Strojniški vestnik
Journal of Mechanical Engineering

Since 1955

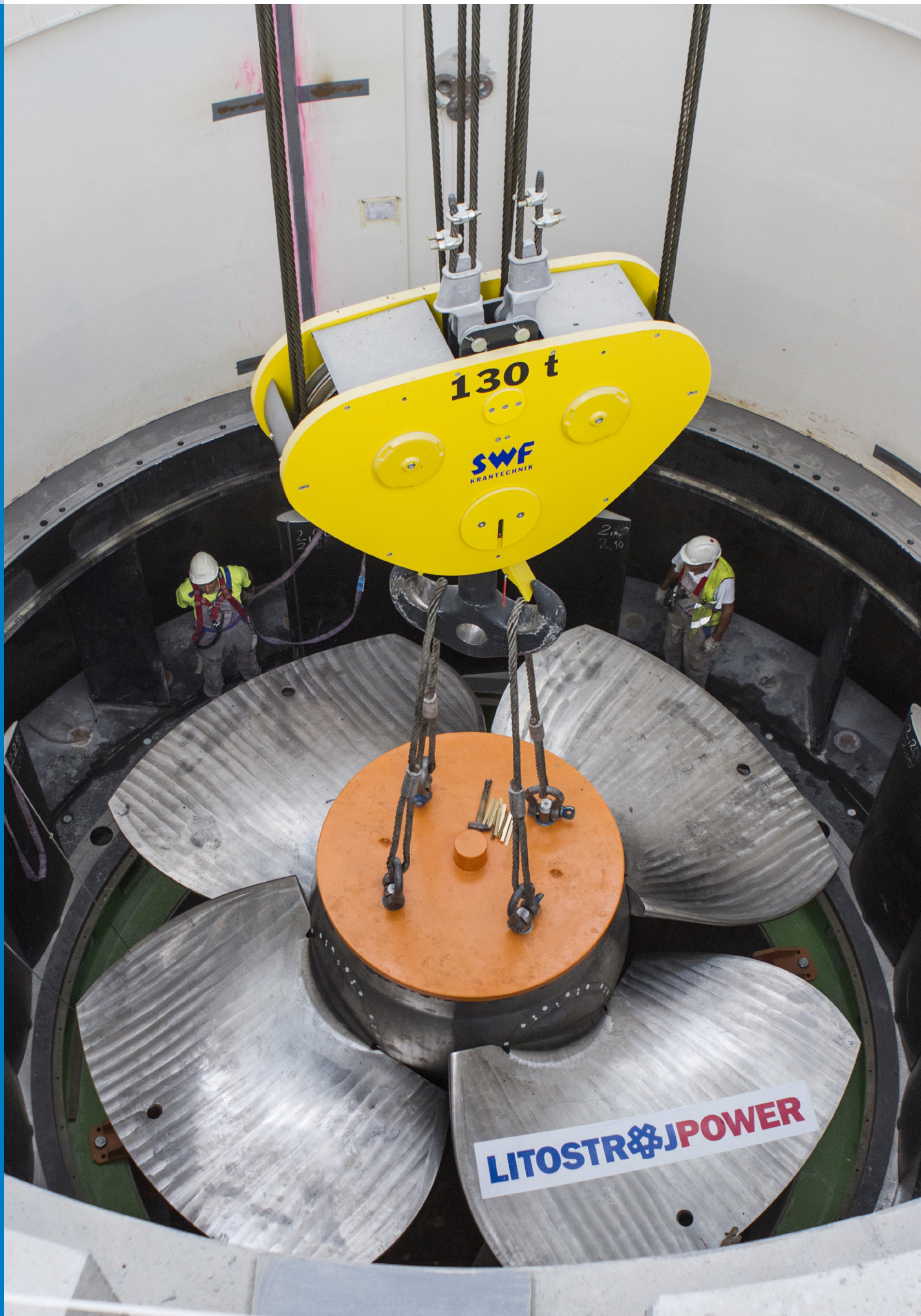

no. 9
year 2018
volume 64

Strojniški vestnik – Journal of Mechanical Engineering (SV-JME)

Aim and Scope
The international journal publishes original and (mini)review articles covering the concepts of materials science, mechanics, kinematics, thermodynamics, energy and environment, mechatronics and robotics, fluid mechanics, tribology, cybernetics, industrial engineering and structural analysis.
The journal follows new trends and progress proven practice in the mechanical engineering and also in the closely related sciences as are electrical, civil and process engineering, medicine, microbiology, ecology, agriculture, transport systems, aviation, and others, thus creating a unique forum for interdisciplinary or multidisciplinary dialogue.
The international conferences selected papers are welcome for publishing as a special issue of SV-JME with invited co-editor(s).

Editorial Office
University of Ljubljana, Faculty of Mechanical Engineering
SV-JME, Aškerčeva 6, SI-1000 Ljubljana, Slovenia
Phone: 386 (0)1 4771 137
Fax: 386 (0)1 2518 567
info@sv-jme.eu, http://www.sv-jme.eu

Print: Abografika, printed in 300 copies

Founders and Publishers
University of Ljubljana, Faculty of Mechanical Engineering, Slovenia
University of Maribor, Faculty of Mechanical Engineering, Slovenia
Association of Mechanical Engineers of Slovenia
Chamber of Commerce and Industry of Slovenia, Metal Processing Industry Association

Cover:
Lowering of a large Kaplan runner assembly into the turbine pit in the Brežice powerhouse on Sava river, Slovenia
(maximum turbine output: 21.4 MW, turbine diameter: 4900 mm).

Image Courtesy:
Litostroj Power d.o.o., Slovenia

ISSN 0039-2480, ISSN 2536-2948 (online)

General information
Strojniški vestnik – Journal of Mechanical Engineering is published in 11 issues per year (July and August is a double issue).

Institutional prices include print & online access: institutional subscription price and foreign subscription €100,00 (the price of a single issue is €10,00); general public subscription and student subscription €50,00 (the price of a single issue is €5,00). Prices are exclusive of tax. Delivery is included in the price. The recipient is responsible for paying any import duties or taxes. Legal title passes to the customer on dispatch by our distributor.

Single issues from current and recent volumes are available at the current single-issue price. To order the journal, please complete the form on our website. For submissions, subscriptions and all other information please visit: *http://www.sv-jme.eu.*

You can advertise on the inner and outer side of the back cover of the journal. The authors of the published papers are invited to send photos or pictures with short explanation for cover content.

We would like to thank the reviewers who have taken part in the peer-review process.

The journal is subsidized by Slovenian Research Agency.

Strojniški vestnik - Journal of Mechanical Engineering is available on *http://www.sv-jme.eu*, where you access also to papers' supplements, such as simulations, etc.

Contents

Strojniški vestnik - Journal of Mechanical Engineering
volume 64, (2018), number 9
Ljubljana, September 2018
ISSN 0039-2480

Published monthly

Guest Editorial

Special Issue: Hydraulic Engineering

Slovenian Association of Hydraulic Research (SDHR) is organizing invited lectures on hydraulic engineering held at the Faculty of Civil and Geodetic Engineering, University of Ljubljana. This issue brings together seven distinct lectures in a form of scientific papers. Two papers deal with transient liquid pipe flow investigating the effects of trapped gas and multiple valve closures. The control of air may be a major operational problem in a number of pipelines. Simultaneous and sequential closure of valves may produce high or very low pressures in the pipeline. Three papers present operation of turbomachines in their respective systems. The first one presents fluid-dynamic characteristics of modified mixed-flow impellers for air dispersion with high flow rates. The second paper evaluates cavitating flow in axial turbomachines whereas the third one presents experimental study of intake structures for the cooling tower pumps. Two-phase flow effects, if not properly taken into account, may deteriorate smooth operation of turbomachine systems and may even lead to damage of components. Finally, two papers deal with open channel flow. The first one deals with numerical prediction of flow in a curved channel by using a curvilinear orthogonal numerical mesh. The second one presents a novel method of water surface topography by using laser scanning. Laser scanning is particularly useful for measurement of rapidly varying surfaces. All the papers were peer reviewed and, for the final versions of English texts, careful proof reading was provided.

The guest editors of this thematic issue wish to express our gratitude to the editor-in-chief of Journal of Mechanical Engineering, Prof. Dr. Vincenc Butala and to the technical editor of the journal Mrs. Pika Škraba, who offered us all necessary professional, logistic and financial support. Finally, we would like to thank the reviewers for their concise and fruitful reviews.

Ljubljana, in August 2018

Guest Editors
Assoc. Prof. Dr. Anton Bergant
Prof. Dr. Matjaž Četina

Strojniški vestnik - Journal of Mechanical Engineering 64(2018)9, 501-512

DOI:10.5545/sv-jme.2018.5238
Original Scientific Paper
Received for review: 2018-01-24
Received revised form: 2018-06-04
Accepted for publication: 2018-06-20

Unsteady Pressures Influenced by Trapped Air Pockets in Water-Filled Pipelines

Anton Bergant[1,*] – Arris Tijsseling[2] – Young-il Kim[3] – Uroš Karadžić[4] – Ling Zhou[5] – Martin F. Lambert[6] – Angus R. Simpson[6]
[1] Litostroj Power d.o.o., Slovenia
[2] Technical University Eindhoven, The Netherlands
[3] Detection Services, Australia
[4] University of Montenegro, Montenegro
[5] Hohai University, China
[6] University of Adelaide, Australia

Trapped air pockets may cause severe operational problems in water-filled pipelines. This paper investigates the dynamic behaviour of a single trapped air pocket. A single air pocket creates distinct changes of amplitude, shape and timing of unsteady flow pressure waves when it is located at some point in a pipeline. The severity of the resulting hydraulic transients depends on the size, pressure and position of the trapped air pocket. In this paper, the air pocket is incorporated as a boundary condition in the discrete gas cavity model (DGCM) that also considers the effects of unsteady skin friction. Two distinct case studies are presented: (1) start-up test case (flow starting from rest) and (2) shut-down test case (flow stoppage). The start-up test case has been performed in the University of Montenegro pipeline apparatus (length 55 m, internal diameter 18 mm). A trapped air pocket is confined at the downstream end of the pipeline. The transient event is initiated by rapid opening of a valve positioned at the initial air/water interface. The shut-down test case has been carried out in the University of Adelaide laboratory apparatus (length 37 m, internal diameter 22 mm). A trapped gas pocket is maintained near the midpoint of the pipeline. The shut-down event is initiated by rapid closure of the downstream-end valve. Results of numerical simulations and laboratory investigations are presented and they show profound effects of unsteady skin friction on pressure histories.
Keywords: fluid transients, water hammer, trapped air pocket, discrete gas cavity model, unsteady skin friction, pipeline apparatus

Highlights

- *Trapped air (gas) pockets cause changes in attenuation, shape and timing of pressure waves.*
- *Gas pocket is incorporated as boundary condition in discrete gas cavity model (DGCM).*
- *Start-up and shut-down experiments affected by one trapped gas pocket are investigated.*
- *Unsteady skin friction may significantly increase damping of pressure waves.*

0 INTRODUCTION

Liquid-conveying piping systems should work safely over a broad range of operating conditions. The control of air pockets may be a major problem in piping systems [1] and [2]. Air may be found in water pipelines mainly as stationary pockets or moving bubbles of various sizes. Air pockets can develop in a pipeline by bubble entrainment at inflow locations (such as at headrace tunnel intake structure, pump sump) and by gas release as the water pressure falls (steady or unsteady flow conditions) or the temperature rises. In addition, residual air may be trapped at an air valve if the air discharge through the valve is not properly controlled [3] and [4]. Transport of large pockets of air can also occur during filling and emptying of pipelines. Air movement along the pipeline can be slow during filling and the air column can become trapped adjacent to a closed valve or at a high point thus separating two water columns. Homogeneously distributed air bubbles or trapped air pockets in a liquid pipeline system can significantly reduce pressure wave propagation velocity (wave speed) and cause changes in the attenuation, shape and timing of pressure waves. This depends on the amount of the air in bubbles and pockets [5] and [6]. Air removal is traditionally performed using air valves. Correctly designed and sized air valves release unwanted air out of the pipeline in a controlled and safe manner. Dynamic effects of poorly selected air valves may cause large pressure peaks (air valve slam) as found by Campbell [7] and recently reviewed by Ramezani et al. [8].

The effects of entrapped air on hydraulic transients can be either beneficial or detrimental, with the outcome being entirely dependent on the layout of the piping system, the size and location of the air pocket(s), and the type of transient event (valve closure or opening, pump start-up or failure, turbine shut-down). The influence of air is more profound in low-pressure systems. Hydraulic transients in a pipeline that contains air pockets may

*Corr. Author's Address: Litostroj Power d.o.o., Litostrojska 50, 1000 Ljubljana, Slovenia, anton.bergant@litostrojpower.eu

create pressure spikes that are either greater than or less than those that would occur without any air as a result of reflections from the interfaces between the liquid and the air pockets [6] and [9]. The most severe pressure rise occurs during the rapid acceleration of a liquid column towards a volume of air that is completely confined [10] and [11]. The maximum pressure can be higher than the Joukowsky pressure if the transient is generated rapidly. However, a large air cavity may alternatively act as an air cushion that attenuates pressure surges in a pipeline. Numerical and experimental studies of dynamic behaviour resulting from entrapped air pockets in pipelines have been previously presented by Martin [10] in his pioneer work, and most recently by Zhou et al. [12]. Numerical models are both based on rigid-column theory for systems with relatively large air pockets and on elastic water-hammer theory for systems with smaller air pockets [12]. The liquid column length may be assumed as constant (for a lumped gas pocket of relatively small volume) or as variable (air/water interface is allowed to move, long air columns).

This paper brings together and further explores unsteady pressures influenced by relatively small trapped air (gas) pockets in two nominally ‘unsteady-friction dominated’ liquid-filled pipelines [13]: (1) University of Montenegro pipeline apparatus (length 55.37 m, internal diameter 18 mm) [14] and (2) University of Adelaide laboratory apparatus (length 37.32 m, internal diameter 22.1 mm) [15]. Trapped gas pockets are incorporated as (internal and end) boundary conditions (discrete gas cavities) in the discrete gas cavity model (DGCM) [5]. Isentropic behaviour is assumed for relatively large trapped gas pockets and an isothermal bath for small gas cavities. In addition, a computationally efficient and accurate convolution-based unsteady skin friction term [16] is incorporated in the DGCM. This is essential because numerical and experimental investigations herein show that the fully-developed pressure traces may be strongly attenuated by unsteady friction. Unsteady friction has not been used by other authors for analysis of the effects of trapped gas pockets in water-filled pipelines. Treatment of very large trapped gas volumes (long gas columns) is beyond the scope of this paper. Details on modelling of very long trapped gas columns can be found in the literature including Chaiko and Brinckman [17], Malekpour and Karney [18], and most recently by Tijsseling et al. [19]. The DGCM developed in this paper is then validated against the results from two distinct experimental runs: (1) start-up test case (flow starting from rest – such as for a pump start-up or a valve opening) [14] and (2) shut-down test case (flow stoppage – such as for a pump failure or a valve closure) [15]. The start-up test case has been performed in the University of Montenegro pipeline apparatus. A trapped gas pocket is captured between two ball valves at the downstream-end of the pipeline. The transient event is triggered by rapid opening of the valve that initially separates the water column and air pocket; the downstream-end valve stays closed during the event. The shut-down test case has been carried out in the University of Adelaide laboratory apparatus. In this apparatus the trapped gas pocket is captured at the midpoint of the pipeline in a specially designed air-pocket device. The shut-down event is initiated by the rapid closure of a side-discharge solenoid valve positioned at the downstream-end of the pipeline.

1 THEORETICAL MODELLING

A DGCM with consideration of unsteady skin friction effects is presented in this Section. Unsteady pipe flow is described by the continuity equation and the equation of motion [3] and [5]. The method of characteristics (MOC) transformation of the unsteady pipe flow equations gives the water hammer solution procedure. The DGCM allows gas cavities to grow at computational sections in the MOC numerical grid [5]. Trapped gas pockets are incorporated as (internal and end) boundary conditions (discrete gas cavities).

1.1 Unsteady Pipe Flow Equations

Water-hammer refers to the transmission and reflection of pressure waves in liquid-filled pipelines. Unsteady pipe flow is described by the continuity equation and the equation of motion [5]

$$\frac{\partial H}{\partial t}+V\frac{\partial H}{\partial x}-V\sin\theta+\frac{a^2}{g}\frac{\partial V}{\partial x}=0, \tag{1}$$

$$g\frac{\partial H}{\partial x}+\frac{\partial V}{\partial t}+V\frac{\partial V}{\partial x}+f\frac{V|V|}{2D}=0. \tag{2}$$

All symbols are defined in Section 6. The flow in the pipe is assumed to be uni-directional (with cross-sectional averaged velocity and pressure distributions), the pressure always remains greater than the liquid vapour pressure, the pipe wall and liquid behave linearly elastically, unsteady friction losses are usually approximated as steady friction losses, the amount of free gas in the liquid is negligible, fluid-structure coupling is negligible, and there are no leakages and blockages along the pipe. For most acoustic problems, the transport terms $V(\partial H/\partial x)$, $V(\partial V/\partial x)$ and $V\sin\theta$, are very small compared to the other terms and may be neglected [5] and [20]. A simplified form of Eqs. (1) and (2) using the discharge $Q = VA$ instead of the flow velocity V leads to

$$\frac{\partial H}{\partial t} + \frac{a^2}{gA}\frac{\partial Q}{\partial x} = 0, \tag{3}$$

$$\frac{\partial H}{\partial x} + \frac{1}{gA}\frac{\partial Q}{\partial t} + f\frac{Q|Q|}{2gDA^2} = 0. \tag{4}$$

The method of characteristics transformation of the simplified Eqs. (3) and (4) produces the water-hammer compatibility equations which are valid along the characteristics lines [5] and [20]. The compatibility equations in finite-difference form are numerically stable unless the friction is dominant and the computational grid is coarse and, when written for computational section i, are [5]:

- along the C^+ characteristic line ($\Delta x/\Delta t = a$)

$$H_{i,t} - H_{i-1,t-\Delta t} + \frac{a}{gA}\Big(\left(Q_u\right)_{i,t} - \left(Q_d\right)_{i-1,t-\Delta t}\Big) + \frac{f\Delta x}{2gDA^2}\left(Q_u\right)_{i,t}\left|\left(Q_d\right)_{i-1,t-\Delta t}\right| = 0, \tag{5}$$

- along the C^- characteristic line ($\Delta x/\Delta t = -a$)

$$H_{i,t} - H_{i+1,t-\Delta t} - \frac{a}{gA}\Big(\left(Q_d\right)_{i,t} - \left(Q_u\right)_{i+1,t-\Delta t}\Big) - \frac{f\Delta x}{2gDA^2}\left(Q_d\right)_{i,t}\left|\left(Q_u\right)_{i+1,t-\Delta t}\right| = 0. \tag{6}$$

The discharge at the upstream side of the computational section ($(Q_u)_i$) and the discharge at the downstream side of the section ($(Q_d)_i$) are identical for the pure water-hammer case where pressures remain above vapour pressure (transient liquid flow). At a boundary (reservoir, valve, pump, turbine), a device-specific equation replaces one of the water-hammer compatibility equations.

1.2 Discrete Gas Cavity Model (DGCM)

The DGCM allows gas cavities to develop at computational sections in the MOC numerical grid. A liquid phase with a constant wave speed a is assumed to occupy each computational reach. The DGCM is described by the two water-hammer compatibility Eqs. (5) and (6), the continuity equation for the gas cavity volume, and the ideal gas equation [5]. Numerical forms of the continuity equation for the gas cavity volume and the ideal gas equation within the staggered grid of the method of characteristics are:

- continuity equation for the gas volume

$$\left(\forall_g\right)_{i,t} = \left(\forall_g\right)_{i,t-2\Delta t} + \psi\Big(\left(Q_d\right)_{i,t} - \left(Q_u\right)_{i,t}\Big)2\Delta t + (1-\psi)\Big(\left(Q_d\right)_{i,t-2\Delta t} - \left(Q_u\right)_{i,t-2\Delta t}\Big)2\Delta t, \tag{7}$$

- ideal gas equation for the gas pocket

$$\left(H_{i,t} - z_i - h_v\right)\left(\forall_g\right)^n_{i,t} = \left(H_0 - z_0 - h_v\right)\left(\forall_{g0}\right)^n. \tag{8}$$

The polytropic exponent n has values between 1 (isothermal, traditionally used for small gas cavities) and 1.4 (isentropic, used in our simulations for the relatively large trapped gas pocket). The nonlinear system of equations is solved numerically.

The DGCM has been successfully used both for the simulation of gaseous and vaporous cavitation (vaporous cavitation: gas void fraction $\alpha_{g0} \leq 10^{-7}$; $\alpha_{g0} = \forall_{g0}/\forall_{reach}$; $\forall_{reach} = A_i \Delta x$). In the latter case, when the discrete cavity volume calculated by Eq. (7) is negative (cavity collapse), then the cavity volume is recalculated by Eq. (8) (by definition: small cavity exists at each computational section at all times).

1.3 Unsteady Skin Friction

Traditionally the steady skin friction term is incorporated in the water-hammer algorithm. This is satisfactory for slow transients where the wall shear stress has a quasi-steady behaviour. Previous investigations using the steady friction approximation for rapid transients [21] to [23] showed significant discrepancies in attenuation, shape and timing of pressure traces when computational results were compared with results of measurements. The skin friction factor, explicitly used in Eqs. (5) and (6), can be expressed as the sum of a steady part f_s and an unsteady part f_u as proposed by Vardy [24] and his coworkers [25], and Meniconi et al. [26]

$$f = f_s + f_u. \tag{9}$$

The steady friction factor f_s depends on Reynolds number and relative pipe roughness. When the steady friction factor is updated at each time step during simulation, it is referred as quasi-steady friction factor (QF). A number of unsteady friction models has been proposed in the literature including one-dimensional (1D) and two-dimensional (2D) models [21] to [23], and recently three-dimensional (3D) model [27]. The 1D models take into account the actual 2D cross-sectional velocity profile and corresponding viscous losses in different ways. The 2D models compute the actual cross-sectional velocity profile continuously during the water-hammer event. The recent 3D model better captures local and convective accelerations and serves as a 'numerical laboratory' for testing 1D and 2D models. This paper deals with the convolution-based unsteady friction model developed by Zielke [28]. Zielke analytically developed the convolution-based model of unsteady friction (UF) for transient laminar flow. The unsteady part of the friction factor in Eq. (9) is defined by the convolution of a weighting function with past temporal flow-rate accelerations

$$f_u = \frac{32\nu A}{DQ|Q|}\int_0^t \frac{\partial Q}{\partial t^*} W_0\left(t-t^*\right)dt^*. \quad (10)$$

Zielke evaluated Eq. (10) using the full convolution scheme, which is computationally intensive (long time simulations). Vítkovský et al. [16] developed an efficient and accurate method that makes an approximation of the weighting function $W(\tau)$ by a finite sum of N_W exponential terms:

$$W_{app}(\tau) = \sum_{k=1}^{N_W} m_k e^{-n_k \tau}. \quad (11)$$

The unsteady part of the friction factor is defined as:

$$f_u = \frac{32\nu A}{DQ|Q|}\sum_{k=1}^{N_W} y_k\left(t\right), \quad (12)$$

in which the component $y_k(t)$ is expressed as

$$y_k(t) = \int_0^t \frac{\partial Q}{\partial t^*} m_k e^{-n_k K\left(t-t^*\right)} dt^*. \quad (13)$$

The constant factor K $(=4\nu/D^2)$ converts the time t into the dimensionless time $\tau=4\nu t/D^2$. At time $t+2\Delta t$ the component y_k is

$$y_k(t+2\Delta t) = \int_0^{t+2\Delta t} \frac{\partial Q}{\partial t^*} m_k e^{-n_k K\left(t+2\Delta t-t^*\right)} dt^*. \quad (14)$$

Integration of Eq. (14) in terms of the dimensionless time step $\Delta\tau$ $(=K\Delta t)$ gives an efficient recursive expression for the component y_k and hence for f_u

$$y_k(t+2\Delta t) = e^{-2n_k K\Delta t} y_k(t) + m_k e^{-n_k K\Delta t}\left[Q(t+2\Delta t) - Q(t)\right]. \quad (15)$$

The convolution is still there, but it is dealt with efficiently through exponential functions. The coefficients of the exponential sum (m_k and n_k) have been developed both for Zielke's weighting function for transient laminar flow [28] and for Vardy-Brown's weighting functions for transient turbulent flow [29] and [30] and can be found in Vítkovský et al. [16]. The Vítkovský et al. [16] model is accurate over a wide range of dimensionless times $\Delta\tau$ $[10^{-6}, 10^{-1}]$ and this condition has been considered in all simulations presented in Sections 3.1 and 3.2. It should be noted that for lower $\Delta\tau$ values Urbanowicz [31] and [32] developed a computationally efficient and accurate approximation of weighting functions that can be used when $\Delta\tau \leq 10^{-6}$. In addition, the UF cannot produce the small low frequency shift observed in experimental results. The measured wave speed is slightly lower than the classical theoretical one as the liquid has extra inertia due to the unsteady velocity profile, which is asymptotically related to the momentum correction factor as found by Schönfeld [33]. The momentum correction factor is relatively constant during the transient event and can be found in Chen [34]. Its value is close to 1.

2 LABORATORY TEST FACILITIES

Experiments with trapped air pockets have been performed in two laboratory test facilities. Tests with flow starting from rest have been carried out in the University of Montenegro pipeline apparatus [14] and tests with flow stoppage in the University of Adelaide apparatus [15].

2.1 Montenegro Pipeline Apparatus

A multi-purpose pipeline apparatus has been designed and constructed at the Faculty of Mechanical Engineering, University of Montenegro, for investigating rapid water-hammer events including column separation and fluid-structure interaction. The apparatus is comprised of a horizontal steel pipeline (total length of 55.37 m (U_x=±0.01 m); internal diameter of 18 mm (U_x=±0.1 mm); pipe wall thickness of 2 mm (U_x=±0.05 mm)) that connects the upstream-end high-pressurized tank (Tank 1) to the outflow tank (Tank 2) – see Fig. 1. The uncertainty in a measurement U_x is expressed as the root-sum-square combination of bias and precision error [35]. Four valve units are positioned along the pipeline including the end points. The valve units at the upstream-end tank (position 0/3) and at the two equidistant positions along the pipeline (positions 1/3 and 2/3) consist of two hand-operated ball valves that are connected to the intermediate pressure transducer block. A T-section with an on/off air inlet valve is installed between the upstream end valve unit (position 0/3) and the high-pressurized tank to facilitate pipeline emptying tests. The horizontal pipe upstream-end service valve is installed between the T-section and the high-pressurized tank in order to isolate upstream-end tank during emptying tests. There are four 90° bends along the pipeline with radius of curvature R_b=3D. The pipeline is anchored against axial movement at 37 points (as close as possible to the valve units and bends). The air in the upstream-end tank can be adjusted up to 800 kPa gauge pressure. Pressure in the tank is kept constant during each experimental run by using a high precision fast-acting air pressure regulator (precision class: 0.2 %) in the compressed air supply line.

Four dynamic high-frequency pressure transducers are positioned within the valve units along the pipeline including the end points (see Fig. 1). Pressures $p_{0/3}$, $p_{1/3}$, $p_{2/3}$ and $p_{3/3}$ are measured by Dytran 2300V4 high-frequency flush-mounted piezoelectric pressure transducers (absolute pressure range: up to 0 MPa to 6.9 MPa; resonance frequency: 500 kHz; acceleration compensated; discharge time constant: 10 seconds (fixed); U_x=±0.1 %). An Endress+Hauser PMP131 strain-gauge pressure transducer has been installed at the control valve V3/3C (pressure $p_{3/3\text{-}sg}$; pressure range: 0 MPa to 1 MPa; U_x=±0.5 %) to measure (1) initial pressure in the confined space between the valves V3/3E and V3/3H (or V3/3P), and (2) transient response of a trapped air pocket after rapid opening of either V3/3H or V3/3P. The water temperature is monitored by a thermometer installed in the outflow tank. The water-hammer wave speed was determined as a=1340 m/s (U_x=±0.1%).

The experimental start-up run with a confined trapped air pocket at the downstream-end valve (V3/3E – see Fig. 1) is carried out as follows. The pressure in the upstream-end Tank 1 is adjusted to a desired value using the high precision air pressure regulator. The control needle valve (V3/3C) is fully open. The upstream-end valve (V0/3U) at the pressurized tank (position 0/3 in Fig. 1) is closed. All other valves of the four valve units are fully open. The air inlet valve (V0/3A) is closed (isolation of the compressed air supply into the pipeline), and the downstream-end emptying valve (V3/3E) is open. The filling of the initially empty pipeline is initiated by opening the valve V0/3U. When steady state flow conditions are reached, the downstream-end valve (either V3/3P or V3/3H) is closed as fast as possible.

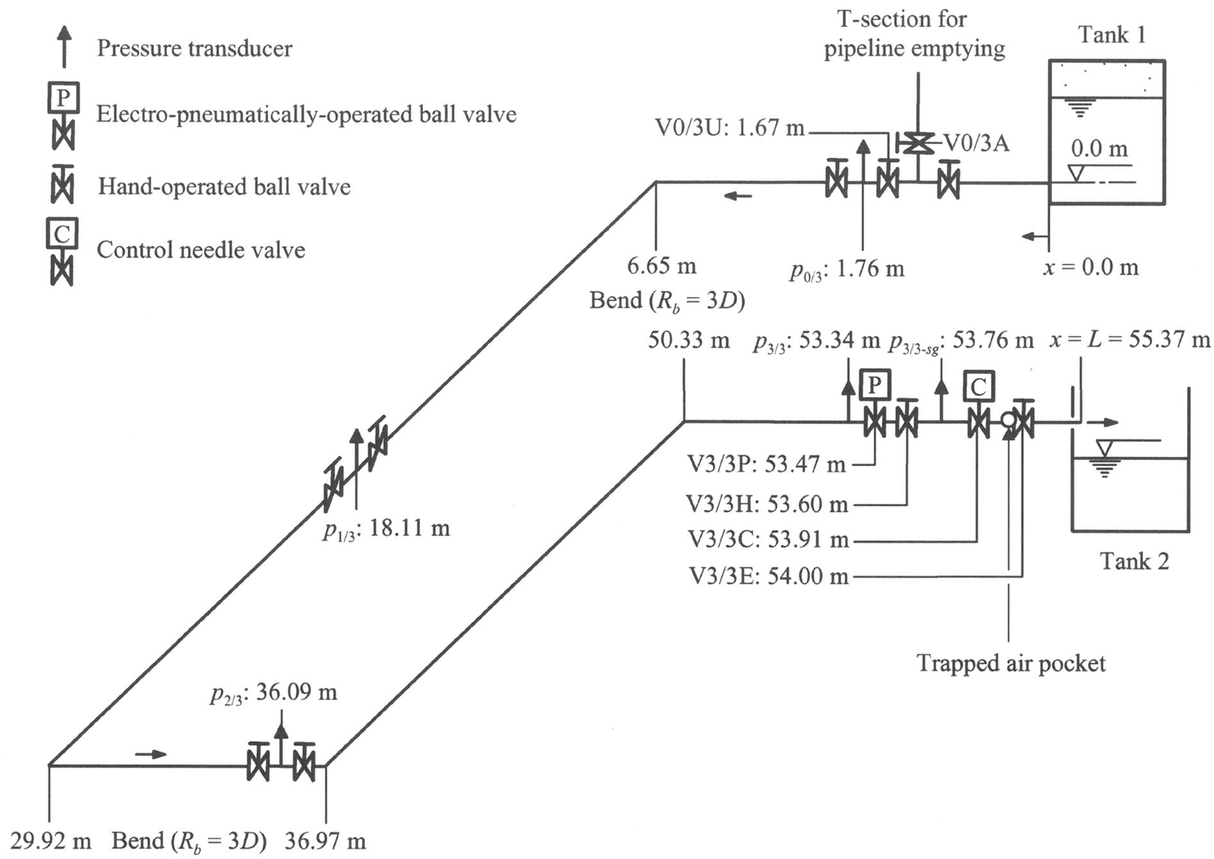

Fig. 1. *Montenegro pipeline apparatus (total length L = 55.37 m; diameter D = 18 mm)*

After complete valve closure, a large amount of water is flushed downstream the valve into the outflow tank. The pressure downstream of the closing valve drops to the atmospheric pressure and upstream the valve the reservoir pressure remains. Then the emptying valve V3/3E is closed. The system is now ready for experiments. The start-up experiment is initiated by the rapid opening of the hand-operated valve V3/3H (or V3/3P). It should be noted that the space between the valves V3/3E and V3/3H (or V3/3P) is occupied by air and residual water due to the inline control valve V3/3C which prevents full flushing. This deficiency will be removed in the near future by adequate redesign of the pipeline outlet. Therefore, the initial value of the trapped gas volume is estimated by a trial and error method based on best fit between the measured and computed first pressure peak at the valve.

2.2 Adelaide Pipeline Apparatus

A versatile pipeline apparatus for investigating water hammer and column separation in pipelines was constructed in the Robin Hydraulics Laboratory at the University of Adelaide, Australia. The apparatus has been modified to investigate the effects of in-line boundaries on transients [36] including the effect of a trapped gas pocket. The modified apparatus comprises a straight 37.32 m (37.53 m including a service valve; $U_x = \pm0.01$ m) long sloping copper pipe of 22.1 mm ($U_x = \pm0.1$ mm) internal diameter and of 1.63 mm ($U_x = \pm0.05$ mm) wall thickness connecting two pressurized tanks (Tanks 1 and 2 in Fig. 2). The upward pipe slope is constant at 5.45 % ($U_x = \pm0.01$ %). A specified pressure in each of the tanks is controlled by a computerized pressure control system. The net water volume in both tanks and the capacity of the air compressor limits the maximum steady state velocity to 1.5 m/s; the maximum operating pressure in each tank is 690 kPa. The pressure waves are recorded by four high-resolution flush-mounted strain-gauge pressure transducers Druck PDCR 810 (absolute pressure range: 0 MPa to 6 MPa; resonance frequency: >360 kHz; $U_x = \pm0.3$ %). The two transducers are located at the end tanks: $p_{0/2}$ and $p_{2/2}$, and the two at the midpoint: $p_{1/2U}$ and $p_{1/2D}$ (one below the pipe axis at the trapped air pocket device and one 1.34 m downstream of the device, respectively) - see Fig. 2.

A special trapped air pocket device is installed practically at the midpoint of the pipeline (Fig. 2). Four screw bolt type devices with trapped air volumes of $\forall_{g0,1/2U} = \{0.43; 1.20; 3.93; 48.0\} \times 10^{-7}$ m³ have been designed and constructed. The device has a hole drilled in the middle and it is inserted in a brass block. The cavity volume of the air pocket devices can be measured by using the diameter and depth of holes or by using 1.25 cm³ micro centrifuge tube with a conical bottom. The experimental procedure requires the careful removal of any residual air from the pipeline before the tests. The only air in the pipeline system should be trapped in the device.

Shut-down events are generated at the downstream location (at the left hand end in Fig. 2) by a side-discharge solenoid valve V2/2S with a very fast closing time (effective valve closure time of 4 ms). The service valve at Tank 2 V2/2H is closed at all times during transient runs. The initial flow velocity

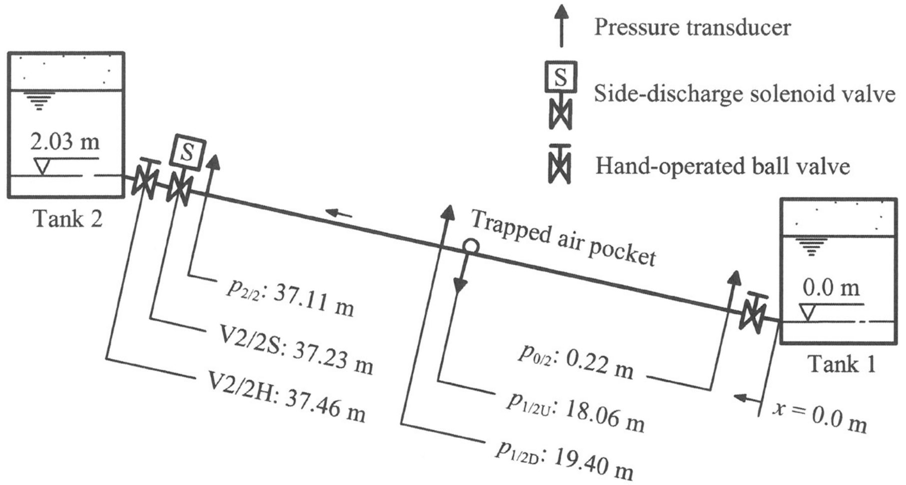

Fig. 2. *Adelaide pipeline apparatus (total length L = 37.53 m; internal diameter D = 22.1 mm)*

(U_x=±1 % for the volumetric method) is established by changing the pressure in the upstream end Tank 1. The water temperature is recorded by a thermometer installed in Tank 2. The wave propagation velocity was determined as a=1330 m/s (U_x=±0.1 %).

3 NUMERICAL AND EXPERIMENTAL RESULTS

Laboratory measurements of hydraulic transient events in pipelines are traditionally used for validation of water-hammer software packages. The case studies herein present two typical examples of validation of a trapped gas pocket boundary condition that is incorporated in the classical discrete gas cavity model [5] with unsteady skin friction term extension. Numerical results from the DGCM with consideration of QF and UF are compared with the results of laboratory measurements taken in Montenegro (Fig. 1) and Adelaide (Fig. 2) pipeline test facilities.

3.1 Start-up Test Case (Montenegro Pipeline Apparatus): Air Pocket at Pipe End

The flow start-up experiment is initiated by the rapid opening of the hand-operated downstream-end valve V3/3H in the Montenegro test apparatus as explained in Section 2.1. Initially the air pocket is confined in the space between the valves V3/3E and V3/3H (Fig. 1) at atmospheric pressure and the liquid (water) in the pipeline is at static conditions (standstill water with Tank 1 pressure). The computed and measured results are presented for the case with initial static head in the upstream-end pressurized tank H_{T1}=52 m (measured at datum level at the top of the pipe inlet at Tank 1 – Fig. 1) and an estimated initial trapped air pocket volume at atmospheric conditions $\forall_{g0,3/3}$=13 cm³ (1.3 × 10^{-5} m³; U_x=±10 %). This air volume is very small in comparison to the total water volume in the pipeline of 13.6 litres (13,600 cm³). The minor losses (entrance, in-line ball valves and large-radius bends) have been neglected in numerical simulations. The magnitude of minor losses is less than 1 % of the total line losses at different steady flow velocities of interest. Internal water and surrounding temperatures were about 25 °C and 30 °C, respectively. Fig. 3 shows measured absolute heads H^*_{air} (pressure $p_{3/3\text{-}sg}$) in the area of the confined air pocket and $H^*_{3/3}$ (pressure $p_{3/3}$) at the upstream end of the electro-pneumatically-operated ball valve V3/3P (H^* = absolute head herein; $H^*=H-z+H_b$). The effective valve opening time of t_{oef}=0.015 s is significantly shorter than the water-hammer wave-return time of $2L/a$=0.080 s. The effective valve opening time is also shorter than the time t=0.15 s of occurrence of the maximum bulk head at the air pocket interface. The assumption of instantaneous valve opening used in the DGCM simulations is justified [12]. The maximum peak head occurs as short duration pressure pulse at time t=0.175 s. This peak pressure is due to the superposition of the trapped air pocket induced bulk head wave with the reservoir-reflected low pressure wave (two end-boundary-induced waves). The frequency of damped bulk pressure oscillations of 5 Hz is naturally lower than the first hydraulic frequency of the reservoir-pipeline-closed valve system of 6.2 Hz ($f_h=a/(4L)$ [37]: a=1340 m/s, L=54 m).

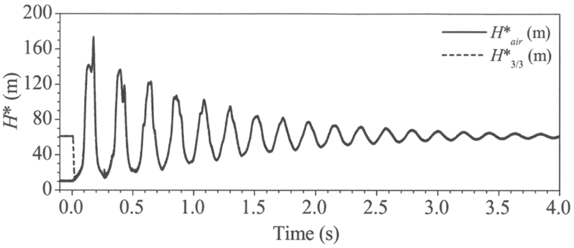

Fig. 3. *Variation of measured absolute air and liquid heads at the downstream dead end (H^*_{air} and $H^*_{3/3}$) in Montenegro apparatus: H_{T1} = 52 m; $\forall_{g0,3/3}$ = 13 cm³*

Numerical results from the DGCM (as described in Section 1.2) are compared with results of the laboratory measurements at the downstream end valve (pressure $p_{3/3}$ in Fig. 1) and along the pipeline (pressures $p_{2/3}$ and $p_{1/3}$ in Fig. 1). The effect of unsteady friction is included in the simulations by using the Zielke weighting function for transient laminar flow [28]. The number of pipe reaches for all computational runs is N=12 and the time step is Δt=0.0033 s. The corresponding dimensionless time $\Delta\tau=4\nu\Delta t/D^2=3.7\times10^{-5}$ in the Vítkovský et al. [16] unsteady friction weighting function approximation is well within the applicable range of the model (see Section 1.3). The DGCM void fraction at the downstream-end closed valve (location of the trapped air pocket) is of the order of $\alpha_{g0,3/3}=10^{-3}$ (at atmospheric conditions) and much larger than the void fractions of $\alpha_{g0}=10^{-7}$ at the other 11 computational sections (except 0.5×10^{-7} at the upstream-end reservoir). Simulations using the isentropic relation for the trapped gas pocket and the isothermal one for the negligibly small gas cavities produce the best fit with the measured results for the considered case study. In addition, simulations with larger numbers of pipe reaches (24, 48; $\alpha_{g0,3/3}$ is updated accordingly) produce practically the same results (showing the robustness of the DGCM). A weighting factor of ψ=1 has been used in the DGCM Eq. (7) [38].

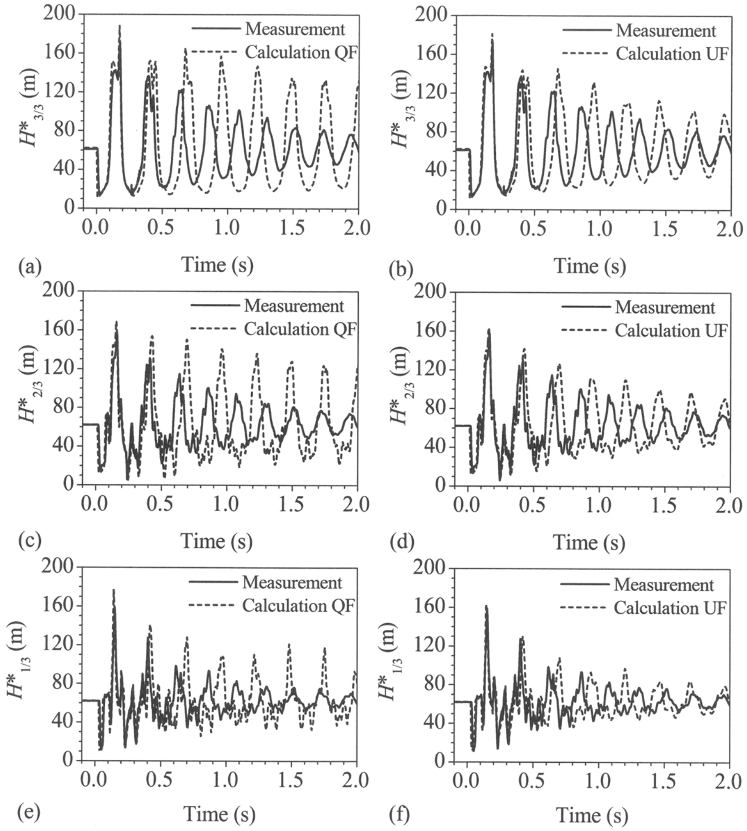

Fig. 4. *Comparison of absolute heads at the downstream end ($H^*_{3/3}$) and along the pipeline ($H^*_{2/3}$ and $H^*_{1/3}$) in Montenegro apparatus: H_{T1} = 52 m; $\forall_{g0,3/3}$ = 13 cm³*

The results from the DGCM using the QF are presented in Figs. 4a ($H^*_{3/3}$), 4c ($H^*_{2/3}$) and 4e ($H^*_{1/3}$). There is a good match between maximum head peaks and pressure wave timing in the early phase of the transient event. However, the results significantly differ from the measurements both in attenuation and timing of pressure traces at later times. It is evident that the DGCM-QF (quasi-steady) model does not produce sufficient damping both for the bulk pressure traces and the short-duration pressure peaks. On the contrary, when using DGCM with UF model the results improve significantly not only in attenuation but also in timing – Figs. 4b ($H^*_{3/3}$), 4d ($H^*_{2/3}$) and 4f ($H^*_{1/3}$) but there are still some discrepancies in timing and attenuation at later times. These discrepancies may be attributed to additional head losses at the control needle valve (not accounted for in the simulations) and possible air pocket separation and consequent entrainment of some air bubbles with reverse flow into the initial pure-liquid zone. Careful investigation of computed head traces in computational sections along the pipeline between the transducer positions 2/3 and 3/3 indicates a distributed vaporous cavitation zone that is condensed back to the liquid phase by the reservoir-reflected wave. Cavitation growth and collapse occurs within the time period t is between 0.242 and 0.248 seconds. The propagation of the low pressure wave towards the trapped air pocket boundary and the reflected wave during this period can be visualized from heads at positions 1/3 and 2/3 (absolute heads $H^*_{1/3}$ and $H^*_{2/3}$ in Fig. 4). This unique case study exhibits both trapped air pocket and distributed vaporous cavitation at the same time.

3.2 Shut-down Test Case (Adelaide Pipeline Apparatus): Air Pocket at Pipe Middle

Shut-down is generated by rapid closure of the downstream-end side-discharge solenoid valve V2/2S in the Adelaide test apparatus as presented in Section 2.2. Fig. 5 (absolute head at the downstream end ($H^*_{2/2}$)) and Fig. 6 (absolute head at the midpoint ($H^*_{1/2D}$)) show computational and measured results for the case with initial flow velocity V_0=0.137 m/s at a constant static head in the upstream-end pressurized tank of H_{T1}=51 m (measured at datum level at the top of the pipe inlet at Tank 1 – Fig. 2) and a trapped air pocket at atmospheric conditions of volume $\forall_{g0,1/2U}=0.39$ cm³ (3.93×10^{-7} m³; $U_x=\pm5$ %) - see position of air pocket device in Fig. 2. The air volume is very small in comparison to the total water volume of 14,400 cm³ and therefore isothermal air behaviour is assumed in all simulations. Water and surrounding temperatures were 21 °C and 22 °C, respectively. The initial Reynolds number is $\mathrm{Re}_0=3{,}050$ ($\mathrm{Re}_0=V_0D/\nu$) and the respective approximated Vardy-Brown weighting function W_{app} is taken from Vítkovský et al. [16]. The measured wave speed is $a=1330$ m/s and the estimated initial steady-state friction coefficient is $f_0=0.044$. Minor losses (entrance, ball valve) are small and neglected in the analysis (much less than 1 % of total losses). The effective valve closure time of $t_{cef}=0.004$ s is significantly shorter than the water-hammer wave-return time of $2L/a=0.056$ s.

The number of pipe reaches in the computational runs using the MOC-based DGCM is $N=54$ (55 computational sections) and the time step is $\Delta t=(L/N)/a=0.000519$ s. The dimensionless time $\Delta\tau=4\nu\Delta t/D^2=4.2\times10^{-6}$ is within the applicable range of the Vítkovský et al. [16] model (see Section 1.3). A larger number of reaches (in comparison to the start-up case) has been selected for accurate monitoring of pressure waves due to interaction with the trapped gas pocket. The trapped air pocket is at computational section 27 with $\alpha_{g0,1/2U}=1.48\times10^{-3}$ (at atmospheric conditions) and the other 54 void fractions are taken $\alpha_{g0}=10^{-7}$ (except 0.5×10^{-7} at the end boundaries (reservoir and valve)). As in the start-up case, the $\psi=1$ has been used in Eq. (7).

Fig. 5 presents absolute head at the rapidly closed valve V2/2S. After closure the pressure wave travels towards the trapped air pocket at the midpoint of the pipeline (position 1/2U in Fig. 2). The interaction of the pressure wave and the compressed air pocket is first recorded as spiky pressure drop (Fig. 6) at the pressure transducer closest to the trapped pocket

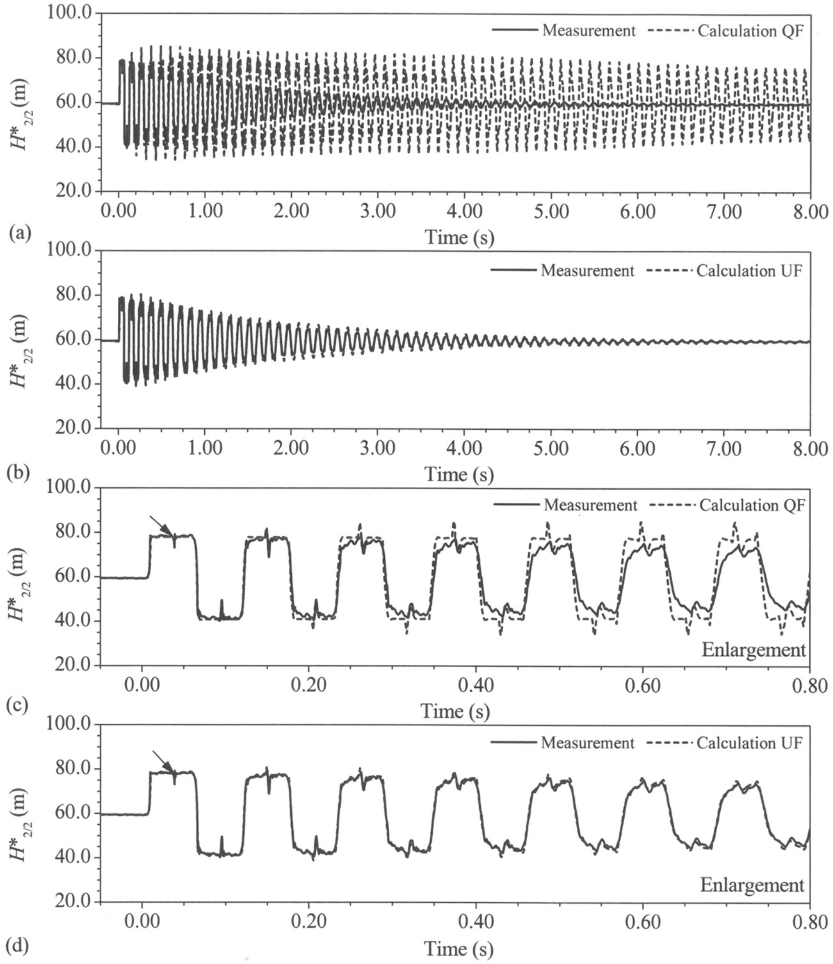

Fig. 5. *Comparison of absolute heads at the downstream end ($H^*_{2/2}$) in Adelaide apparatus: H_{T1} = 51 m; $\forall_{g0,1/2U}$ = 0.39 cm³*

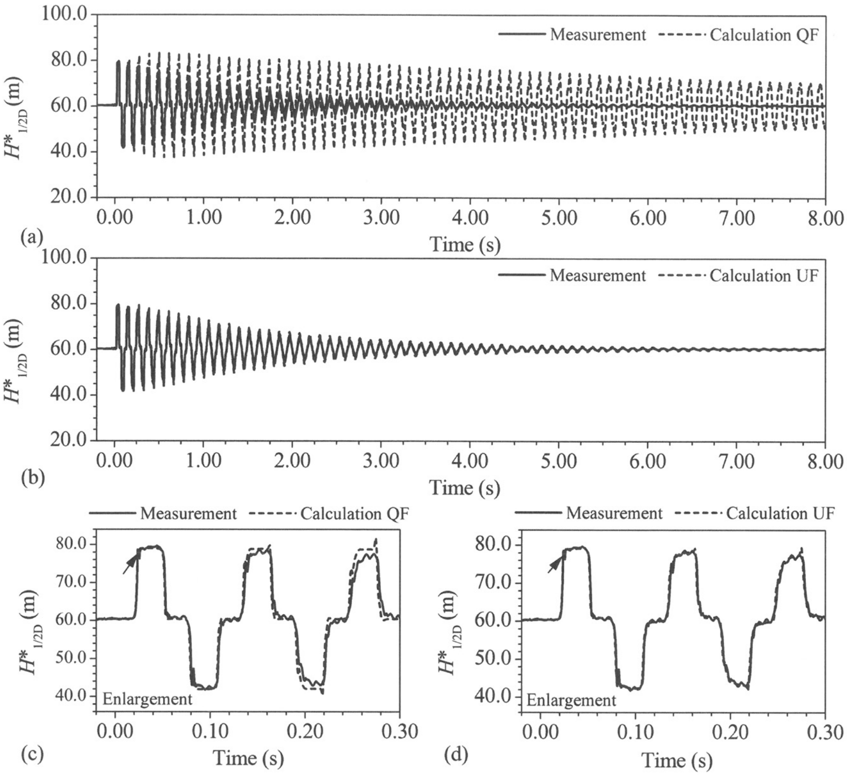

Fig. 6. *Comparison of absolute heads at the midpoint ($H^*_{1/2D}$) in Adelaide apparatus: H_{T1} = 51 m; $\forall_{g0,1/2U}$ = 0.39 cm³*

(position 1/2D in Fig. 2). This occurs about $L/(2a)$ in time after the valve closure as marked in Fig. 6 with the arrow in the $H^*_{1/2D}$-absolute head history. At about L/a after the valve closure the spiky pressure drop arrives at the closed valve (as marked with the arrow in the $H^*_{2/2}$-absolute head history in Fig. 5). The results from DGCM using the QF model differ significantly from the measured results (Figs. 5a and 5c for $H^*_{2/2}$; Figs. 6a and 6c for $H^*_{1/2D}$). The long-time simulations clearly show that the effects cumulate to such an extent that beat develops (Figs. 5a and 6a). The pressure envelope with increasing and decreasing pressure may be visualized. Finally, the pressure starts slowly to decay. When the time window is shortened (Fig. 5c and to a lesser extent Fig. 6c), the beginning of a damped beat on top of damped water-hammer may be observed in the experiment as well. It is evident that the quasi-steady friction model does not produce sufficient damping both for the bulk pressure traces as for the short-duration pressure peaks. Again, an attempt has been made to overcome this deficiency by using the UF model. The results from DGCM using UF are compared with the results of measurements in Figs. 5b and 5d for $H^*_{2/2}$, and Figs. 6b and 6d for $H^*_{1/2D}$. The long-time simulations show that the beat quickly damps out. When the time window is shortened weak experimental and numerical beats may be observed (Figs. 5d and 6d). The unsteady friction model does produce sufficient damping both for the bulk pressure traces and for the short-duration pressure peaks.

4 CONCLUSIONS

Theoretical and experimental investigations show that a single air pocket trapped in a water-filled pipeline creates distinct changes of amplitude, shape and timing of pressure waves. The severity of the resulting hydraulic transients depends on the size, pressure and position of the trapped air pocket. In the DGCM the trapped air pockets are incorporated as internal and end boundary conditions in the MOC scheme. Experiments with one trapped air pocket have been performed in two laboratory test facilities including tests with flow starting from rest (start-up case) and tests with flow stoppage (shut-down case). A trapped air pocket is confined either at the downstream dead-end or captured in a special device near the midpoint of the pipeline, respectively. The dynamic response of the elastic liquid column due to a trapped air pocket in these apparatuses should be similar for both small and large pipelines with similar scalings. The results from DGCM using the QF model significantly differ from the measured results in both test cases. The quasi-steady friction model does not produce sufficient damping both for the bulk pressure traces as for the short-duration pressure peaks. An attempt has been made to overcome this deficiency by using a convolution-based UF model. The unsteady friction model does produce sufficient damping both for the bulk pressure traces and the short-duration pressure peaks and it is recommended for long-duration hydraulic transient analysis. The short duration peaks due to interaction of pressure waves in water-filled pipelines with trapped air pockets have been investigated in depth for the first time.

5 ACKNOWLEDGEMENTS

The authors gratefully acknowledge the support of the Slovenian Research Agency (ARRS) conducted through the project L2-5491 Unsteady skin friction modelling in hydraulic piping systems.

6 NOMENCLATURE

A pipe area, [m^2]
a pressure wave speed, [m/s]
C^+, C^- label of characteristic equation
D pipe internal diameter, [m]
f friction factor, [-]
f_h hydraulic frequency, [Hz]
g gravitational acceleration, [m/s^2]
H piezometric head (head), [m]
H^* absolute pressure head, [m]
H_b barometric head, [m]
h_v gauge vapour pressure head, [m]
K constant in UF model, [-]
L length, [m]
m_k, n_k exponential sum coefficients, [-]
N number of reaches, [-]
N_W number of exp. terms in W_{app}, [-]
n polytropic exponent, [-]
p gauge pressure (pressure), [N/m^2]
Q discharge, [m^3/s]
Q_d downstream-side discharge, [m^3/s]
Q_u upstream-side discharge, [m^3/s]
R_b radius of curvature of bend, [m]
Re Reynolds number, [-]
t, t^* time, [s]
t_{cef} effective valve closure time, [s]
t_{oef} effective valve opening time, [s]
U_x uncertainty in measurement, [%, unit]
V average flow velocity, [m/s]
W weighting function in UF model, [-]
x distance, [m]
y_k component of the W, [m^3/s]
z elevation, [m]
α_g gas void fraction, [-]
Δt time step, [s]
Δx space step or reach length, [m]
θ pipe angle, [rad]
ν kinematic viscosity, [m^2/s]
τ dimensionless time, [-]
ψ weighting factor, [-]
$\forall_g$ gas cavity volume, [m^3]
$\forall_{reach}$ pipe reach volume, [m^3]

Subscripts:
app approximate
g gas
i node number
s steady
T1 upstream-end pressurized tank
u unsteady
0 initial condition

7 REFERENCES

[1] Lauchlan, C.S., Escarameia, M., May, R.W.P., Burrows, R., Gahan, C. (2005). Air in Pipelines. A Literature Review. *Report SR 649*, HR Wallingford Limited, Wallingford.

[2] Ramezani, L., Karney, B., Malekpour, A. (2016). Encouraging effective air management in water pipelines: a critical review. *Journal of Water Resources, Planning and Management*, vol. 142, no. 12, p. 04016053-1-11, **DOI:10.1061/(ASCE)WR.1943-5452.0000695**.

[3] Thorley, A.R.D. (2004). *Fluid Transients in Pipeline Systems. A Guide to the Control and Suppression of Fluid Transients in Liquids in Closed Conduits*. Professional Engineering Publishing Limited, London.

[4] Kruisbrink, A.C.H., Arregui, F., Carlos, M., Bergant, A. (2004). Dynamic performance characterisation of air valves. *Proceedings of the 9th International Conference on Pressure Surges*, p. 33-47.

[5] Wylie, E.B., Streeter, V.L. (1993). *Fluid Transients in Systems*. Prentice Hall, Englewood Cliffs.

[6] Bergant, A., Tijsseling, A.S., Vítkovský, J.P., Covas, D.I.C., Simpson, A.R., Lambert, M.F. (2008). Parameters affecting water-hammer wave attenuation, shape and timing-Part 2: Case studies. *Journal of Hydraulic Research*, vol. 46, no. 3, p. 382-391, **DOI:10.3826/jhr.2008.2847**.

[7] Campbell, A. (1983). The effect of air valves on surge in pipelines. *Proceedings of the 4th International Conference on Pressure Surges*, p. 89-102.

[8] Ramezani, L., Karney, B., Malekpour, A. (2015). The challenge of air valves: A selective critical literature review. Journal of Water Resources, Planning and Management, vol. 141, no. 10, p. 04015017-1-11, **DOI:10.1061/(ASCE)WR.1943-5452.0000530**.

[9] Burrows, R., Qiu, D.Q. (1995). Effect of air pockets on pipeline surge pressure. *Journal of Water Maritime and Energy. Proceedings of Institution of Civil Engineers*, vol. 112, no. 4, p. 349-361, **DOI:10.1680/iwtme.1995.28115**.

[10] Martin, C.S. (1976). Entrapped air in pipelines. *Proceedings of the 2nd International Conference on Pressure Surges*, p. F2-15-F2-28.

[11] Carlos, M., Arregui, F.J., Cabrera, E., Palau, C.V. (2011). Understanding air release through air valves. *Journal of Hydraulic Engineering*, vol. 137, no. 4, p. 461-469, **DOI:10.1061/(ASCE)HY.1943-7900.0000324**.

[12] Zhou, L., Liu, D., Wang, H., Ou, C., Long, A.X. (2015). Numerical comparison of rapid-filling-pipe models with trapped air. *E-proceedings of the 36th IAHR World Congress*, Paper 80823.

[13] Duan, H.F., Ghidaoui, M.S., Lee, P.J., Tung, Y.K. (2012). Relevance of unsteady friction to pipe size and length in pipe fluid transients. *Journal of Hydraulic Engineering*, vol. 138, no. 2, p. 154-166, **DOI:10.1061/(ASCE)HY.1943-7900.0000497**.

[14] Bergant, A., Karadžić, U., Tijsseling, A.S. (2016). Dynamic water behaviour due to one trapped air pocket in a laboratory pipeline apparatus. *IOP Conference Series. Earth and Environmental Science*, vol. 49, p. 967-976, **DOI:10.1088/1755-1315/49/5/052007**.

[15] Bergant, A., Kim, Y., Tijsseling, A.S., Lambert, M.F., Simpson, A.R. (2009). Analysis of beat phenomena during transients with trapped air pocket. *Proceedings of the 3rd IAHR International Meeting of the Workgroup on Cavitation and Dynamic Problems in Hydraulic Machinery and Systems, Part II*, p. 409-418.

[16] Vítkovský, J., Stephens, M., Bergant, A., Lambert, F., Simpson, A. (2004). Efficient and accurate calculation of Zielke and Vardy-Brown unsteady friction in pipe transients. *Proceedings of the 9th International Conference on Pressure Surges*, p. 405-419.

[17] Chaiko, M.A., Brinckman, K.W. (2002). Models for analysis of water hammer in piping with entrapped air. *Journal of Fluids Engineering*, vol. 124, no. 1, p. 194-204, **DOI:10.1115/1.1430668**.

[18] Malekpour, A., Karney, B.W. (2011). Rapid filling analysis of pipelines with undulating profiles by the method of characteristics. *ISRN Applied Mathematics*, vol. 2011, Article ID 930460, **DOI:10.5402/2011/930460**.

[19] Tijsseling, A.S., Hou, Q., Bozkuş, Z. (2015). Analytical expressions for liquid-column velocities in pipelines with entrapped gas. *Proceedings of the ASME 2015 Pressure Vessels & Piping Division Conference*, Paper PVP2015-45184, **DOI:10.1115/PVP2015-45184**.

[20] Chaudhry, M.H. (2014). *Applied Hydraulic Transients*. 3rd ed., Springer, New York, **DOI:10.1007/978-1-4614-8538-4**.

[21] Bergant, A., Simpson, A.R., Vítkovský, J. (2001). Developments in unsteady pipe flow friction modelling. *Journal of Hydraulic Research*, vol. 39, no. 3, p. 249-257, **DOI:10.1080/00221680109499828**.

[22] Pezzinga, G., Brunone, B. (2006). Turbulence, friction, and energy dissipation in transient pipe flow. Brocchini, M., Trivellato, F. (eds.), *Vorticity and Turbulence Effects in Fluid Structure Interaction*. WIT Press, Southampton, p. 213-236, **DOI:10.2495/978-1-84564-052-1/09**.

[23] He, S., Ariyaratne, C., Vardy, A.E. (2008). A computational study of wall friction and turbulence dynamics in accelerating pipe flows. *Computers & Fluids*, vol. 37, no. 6, p. 674-698, **DOI:10.1016/j.compfluid.2007.09.001**.

[24] Vardy, A.E. (1980). Unsteady flows: fact and friction. *Proceedings of the 3rd International Conference on Pressure Surges*, p. 15-26.

[25] Vardy, A.E., Brown, J.M.B., He, S., Ariyarante, C., Gorji, S. (2015). Applicability of frozen-viscosity models of unsteady wall shear stress. *Journal of Hydraulic Engineering*, vol. 141, no. 1, p. 04014064-1-13, **DOI:10.1061/(ASCE)HY.1943-7900.0000930**.

[26] Meniconi, S., Duan, H.F., Brunone, B., Ghidaoui, M.S., Lee, P.J., Ferrante, M. (2014). Further developments in rapidly decelerating turbulent flow modelling. *Journal of Hydraulic Engineering*, vol. 143, no. 12, p. 04014028-1-9, **DOI:10.1061/(ASCE)HY.1943-7900.0000880**.

[27] Martins, N.M.C., Brunone, B., Meniconi, S., Ramos, H.M., Covas, D.I.C. (2017). CFD and 1D approaches for the unsteady friction analysis of low Reynolds number turbulent flow. *Journal of Hydraulic Engineering*, vol. 147, no. 12, p. 04017050-1-13, **DOI:10.1061/(ASCE)HY.1943-7900.0001372**.

[28] Zielke, W. (1968). Frequency-dependent friction in transient pipe flow. *Journal of Basic Engineering*, vol. 90, no. 1, p. 109-115, **DOI:10.1115/1.3605049**.

[29] Vardy, A.E., Brown, J.M.B. (2003). Transient turbulent friction in smooth pipe flows. *Journal of Sound and Vibration*, vol. 259, no. 5, p. 1011-1036, **DOI:10.1006/jsvi.2002.5160**.

[30] Vardy, A.E., Brown, J.M.B. (2004). Transient turbulent friction in fully rough pipe flows. *Journal of Sound and Vibration*, vol. 270, no. 1-2, p. 233-257, **DOI:10.1016/S0022-460X(03)00492-9**.

[31] Urbanowicz, K. (2015). Simple modelling of unsteady friction factor. *Proceedings of the 12th International Conference on Pressure Surges*, p. 113-130.

[32] Urbanowicz, K. (2018). Fast and accurate modelling of frictional transient pipe flow. *Zeitschrift für Angewandte Mathematik und Mechanik*, vol. 98, no. 5, p. 802-823, **DOI:10.1002/zamm.201600246**.

[33] Schönfeld, J.C. (1949). Resistance and inertia of the flow of liquids in a tube or open canal. *Applied Scientific Research*, vol. 1, p. 169-197, **DOI:10.1007/BF02120326**.

[34] Chen, C.L. (1992). Momentum and energy coefficients based on power-law velocity profile. *Journal of Hydraulic Engineering*, vol. 118, no. 11, p. 1571-1584, **DOI:10.1061/(ASCE)0733-9429(1992)118:11(1571)**.

[35] Coleman, H.W., Steele, W.G. (1989). *Experimentation and Uncertainty Analysis for Engineers*. John Wiley and Sons, New York.

[36] Kim, Y. (2008). *Advanced Numerical and Experimental Transient Modelling of Water and Gas Pipeline Flows Incorporating Distributed and Local Effects*. PhD thesis. University of Adelaide, Adelaide.

[37] VDI 3842:2004. *Schwingungen in Rohrleitungssystemen. Vibrations in Piping Systems*. Verein Deutscher Ingenieure, Düsseldorf.

[38] Simpson, A.R., Bergant, A. (1994). Numerical comparison of pipe-column-separation models. *Journal of Hydraulic Engineering*, vol. 120, no. 3, p. 361-377, **DOI:10.1061/(ASCE)0733-9429(1994)120:3(361)**.

Strojniški vestnik - Journal of Mechanical Engineering 64(2018)9, 513-524

DOI:10.5545/sv-jme.2017.5149
Original Scientific Paper
Received for review: 2017-12-13
Received revised form: 2018-03-14
Accepted for publication: 2018-04-11

Asymmetric Blade Disc Turbine for High Aeration Rates

Andrej Bombač
University of Ljubljana, Faculty for Mechanical Engineering, Slovenia

This paper presents some fluid-dynamic characteristics of modified impellers for air dispersion with high flow rates. An asymmetrically folded blade turbine (ABT) was developed as the last in a series of research studies on modified blades of disk impellers, such as twisted blade turbine (TBT) and other blade shape turbines. The analyses of the modified impeller characteristics in a model scale mixing device includes the measurements of: a) the mixing power in liquid stirring and in the air dispersion up to the occurrence of flooding, b) global gas hold up, c) appearance of flooding, and d) the mixing times in liquid stirring. The energy dissipation of the ABT impeller was found to be very small, in the range of hydrodynamic regimes in industrial scale operations with a power number equal to Po_{ABT} ~ 1.75. During aeration in water, the ABT impeller has a very small power draw reduction (less than 16 %) at the same stirrer speed (corresponding to Fr = 0.3) and is capable of dispersing substantially higher amounts of air (up to 53 %) than the Rushton turbine is, as well as achieving shorter mixing times. While local mixing time expresses only changes with the time at the measuring location, a CFD analysis was included for better insight into inhomogeneity in the liquid. To compare the efficacy of the ABT impeller with other impellers, some results of our previous research are summarized.
Keywords: liquid mixing, air dispersing, gas holdup, ABT impeller, flooding, mixing time

Highlights
- *High efficiency of the newly developed asymmetrically folded blade turbine (ABT) during dispersing of air into water by single impeller stirring.*
- *Low power number of the ABT impeller in water mixing (1.75).*
- *High pumping capacity by air dispersing at very small power draw reduction (less than 16 %).*
- *Capable of dispersing much greater amounts of air (up to 53 %) than the Rushton turbine is.*
- *The shortest mixing time by the same impeller energy dissipation.*
- *Some CFD analysis results included for better insight into inhomogeneity in the liquid.*

0 INTRODUCTION

Air dispersion in tall, slim fermenters is mostly carried out with multistage impellers to provide high air flow intake, which must be supplied in some fermentation processes in the pharmaceutical industry. Such an impeller can be assembled of two equal impellers, such as dual Rushton turbines in parallel, merging, and diverging flow conditions [1], power consumption [2], mixing rate [3] or flow patterns [4]. The higher the ratio between tank height and its diameter H/T, the higher the number of impellers equidistantly placed to ensure as much uniform void fraction distribution as possible [5] to [8]. Nowadays, a combination of axial and radial impellers [7] and [9] predominates. The choice of a proper impeller for the given geometric configuration of the mixing vessel is of prime importance for the optimal achievement in the fermentation process: a fermenter must have a flow field that provides the organisms with air throughout the entire volume of the liquid. Any dead zone can cause an improperly fermented product due to lack of air. A multi-stage impeller with a proper configuration provides the circulation of substances in the fermenter and most evenly distributes the air throughout the liquid volume [10]. To determine these conditions, it is necessary to know the main characteristics of the individual impeller, such as the mixing power [11] and [12], gas holdup [11], bubble size and distribution [13] and [14], flooding in gas-liquid systems [8], [15] and [16] and in even more complex three-phase systems [17] and [18], mixing time [19] to [21], etc.

Each impeller dispersing air is limited by the maximum amount of air to be dispersed. Further increasing of the air flow rate causes flooding. From the process operation point of view, flooding is an inefficient operation. Usually, the ring sparger is used for the air intake and is placed in-between the bottom and the lowest impeller. From an extensive study [15] of individual impeller-flooding by gassing in a tall mixing vessel with single, dual (Du) and triple (Tr) Rushton turbines, it was determined that the lowest impeller (Du1 and Tr1, see Fig. 1) is prone to be flooded in both configurations even at lower gas flow rates in comparison to gassing with a single impeller in a standard geometric configuration vessel. Due to lesser pumping capacity, a flooded impeller causes an extremely inhomogeneous gas phase distribution and changes the other basic characteristics, so the lowest impeller is of key importance for effective dispersion.

*Corr. Author's Address: University of Ljubljana, Faculty for Mechanical Engineering, Laboratory for Fluid Dynamics and Thermodynamics, Aškerčeva 6, 1000 Ljubljana, Slovenia, andrej.bombac@fs.uni-lj.si

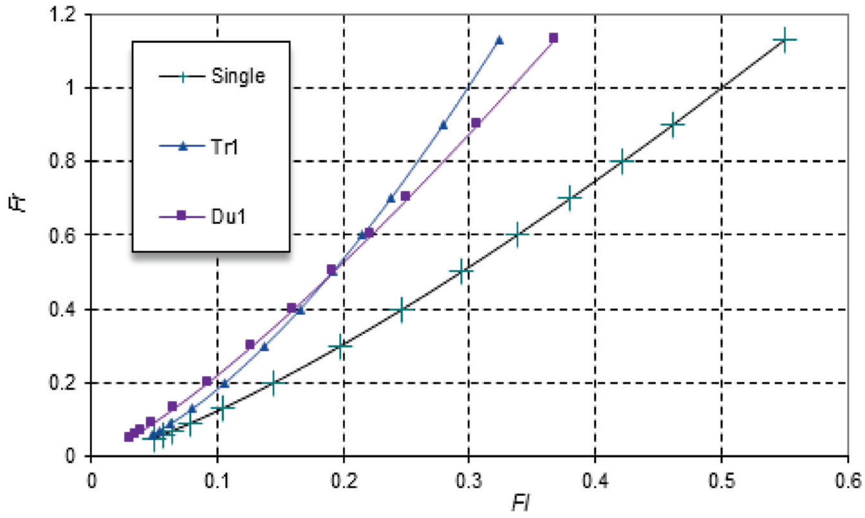

Fig. 1. *Individual impeller flooding conditions; comparison of single, the lowest impeller by dual (Du1) and triple-impeller (Tr1) stirring*

If an additional enlarged amount of air needs to be dispersed in some fermentation processes [8], at a minimum, the lowest impeller must be replaced with a more capable one in terms of preserving the pumping capacity and the small power reduction as much as possible by gassing. There are many studies in which Rushton turbine modifications [21] and [22] and disk impellers of various blade shapes [19] and [23] to [26] were used to enhance the lowest impeller characteristics.

In the following sections, a modified disk impeller ABT [27] is presented, which is derived from the same basic contour of the standard Rushton turbine (RuT) as well as other modifications; such as split blade disk impeller, twisted blade impeller (TBT) [19] and [28] or double disk impeller [29]. The asymmetrically folded blade turbine (ABT) impeller was developed and patented at the Laboratory for Fluid Dynamics and Thermo-dynamics specifically for dispersing large quantities of air, which (in contrast with the other two developed and gradually improved impellers (the TBT and the split blade turbine) demonstrates air dispersion with the least energy dissipation, a high gas holdup, slight power drawn by aeration, and flooding at much higher gas flow rates than any other impellers. Computational fluid dynamics (CFD) is a very useful tool to analyse transitional phenomenon in space-time domain, which mixing time represents. In that manner, CFD was performed by liquid mixing for the same geometric configuration as the experimental setup. It enabled the visualization of the flow field of different impellers as well as the spreading of poured hot water, representing the pulse/response technique of measuring the mixing time.

1 EXPERIMENTAL SETUP AND EXPERIMENT

The measurements of the mixing power were carried out in a mixing vessel comprised of an upright cylindrical vessel, made of acrylic glass with an inner diameter T = 450 mm with rounded edges and a flat bottom. The mixing drive shaft enabled the placement of up to five impellers of various types and clearances between them in case of multi-stage impeller stirring with a maximum height of the water of 1350 mm. Four baffles of width T/10 were axially symmetrically placed perpendicularly to the vessel wall with a gap of 8 mm between the wall and the baffle; the impeller clearance was set to T/3. The experimental set-up by single impeller stirring with liquid height $H = T$ is shown in Fig. 2. Impeller speed was measured by IR-pulse transmitter with an absolute error of ±1 rpm. An HBM transducer enabled torque measurements with an error of ±0.02 Nm, while the gas flow rate was measured with calibrated rotameters with the error ±0.4 m³/h, respectively. A more detailed description of the measurement installations and the accuracy of the measured values, the repeatability of the measurements, etc. are given in [15] and [19]. Tap water was used as the working liquid and air from the in-house compressed air, both at room temperature. Mixing time was measured based on pulse-response technique [19] and [30]. One dm³ of hot water at ~95 °C was poured into the vessel in cca. 0.5 s just above the location of the thermocouple tip {r, z; 65,

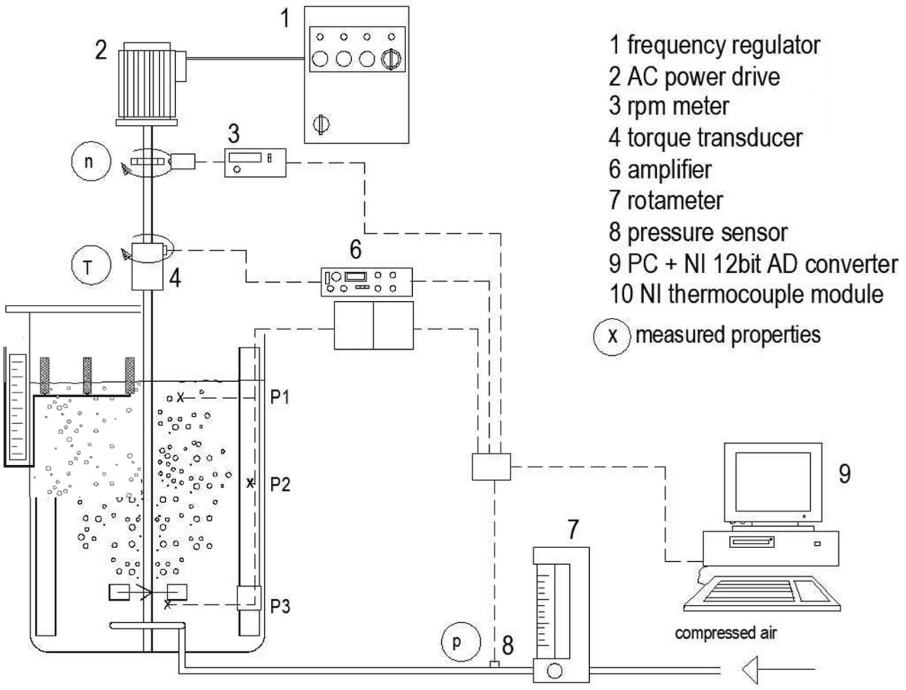

Fig. 2. *Experimental set-up*

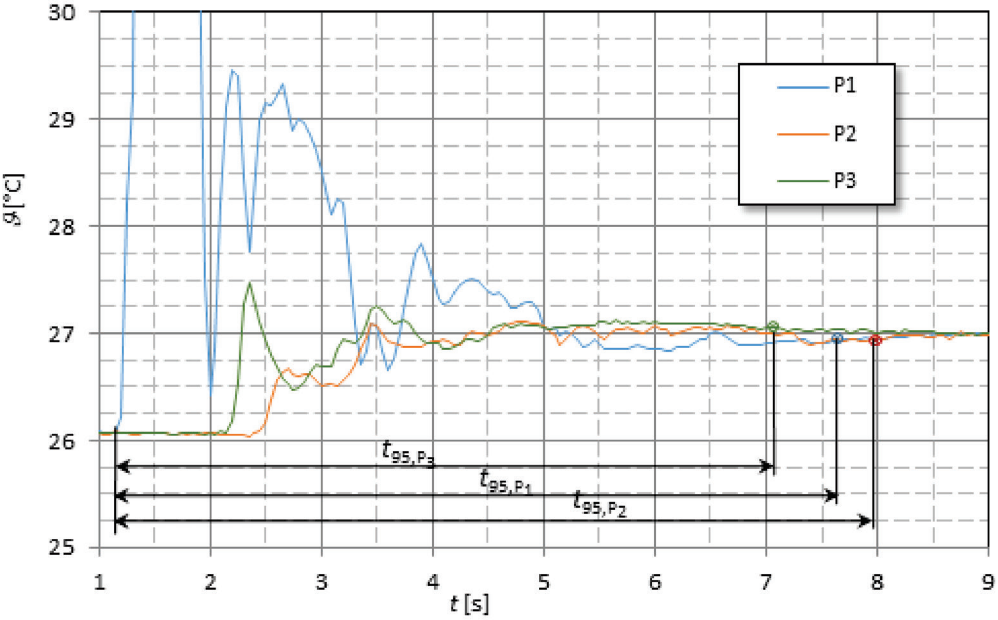

Fig. 3. *Mixing times t_{95} based on pulse response at the measurement locations P1, P2, P3*

420 mm} to begin the measurements. This location was chosen based on literature data **[30]** according to which mixing times were measured at three different locations (below the surface, just under the lower edge of the impeller and near the vessel wall) and varied from –10 % to +6 % in comparison with their mean value. A thin non-insulated thermocouple (Ni-CrNi, type K) of 0.2 mm of diameter tip was used to provide a quick response, which was analysed previously and found to be between 440 °C/s and 550 °C/s. The mixing time t_{95} is defined as the difference between the final time (t_f), when the temperature stabilizes

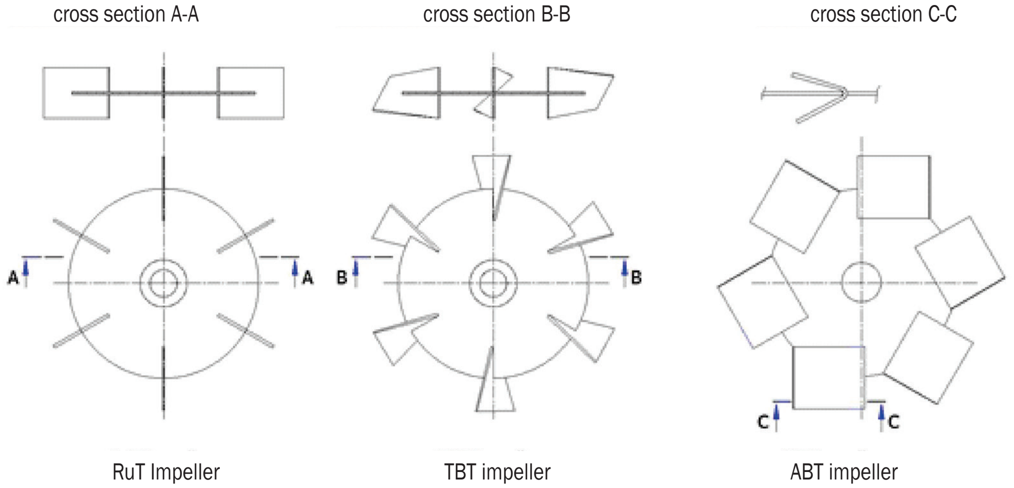

Fig. 4. *A Rushton turbine and both modified impellers*

within ±5 % of the final average temperature, and the start time (t_s) of the pulse entry. The mixing times were calculated from temperatures recorded at three locations defined as: P_1 location (r_1, z_1); (T/4.7 from the impeller centre line, T/4.5 from the level), P_2 location (r_2, z_2); (T/2.2 from the axis of the impeller, T/3 from the level) and P_3 location (r_3, z_3); (T/8 from the axis of the impeller, T/50 from under the edge of the impeller) and averaged ($t_{95,P1}+t_{95,P2}+t_{95,P3}$)/3. Fig. 3 shows separate temperature responses at the all three locations after the pulse input (poured hot water) by stirring with ABT impeller. The sampling frequency of the measuring temperature was set to 10 Hz; each measurement lasted 60 s.

The global gas holdup measurements were performed with improved three-point “level taker”, which based originally on the change of the liquid level height only in one location and was defined for a cylindrical vessel as:

$$\alpha_g = (H_g - H) / H_g, \quad (1)$$

where H_g means the liquid level under gassing and H is the liquid level by liquid mixing. Each α_g was measured at constant impeller speed with a stepwise increase of the air flow rate. The measurements of the height were taken for each individual hydrodynamic regime five times; their average value was used for further analysis. All the impellers used (RuT, TBT, and ABT) are shown in Fig. 4. The blade of the ABT impeller is in the middle by width (w) folded in the form of the letter “V” and placed so that the upper part has a smaller slope than the lower part does, while the upper part is longer than the lower part, as shown in Fig. 4, cross section C-C.

All impellers (RuT, TBT, and ABT) have the same disk diameter, the same width (b) and height (w) of the blades and the impeller diameter (T/3), as shown in Fig. 4.

2 RESULTS AND DISCUSSION

A number of measurements were taken in order to determine the basic impeller characteristics for each type of impeller in liquid mixing and in the dispersing of air into water by a standard geometric configuration of the mixing vessel.

2.1 Mixing Power in Water

The mixing power of each individual impeller was measured for various rotational speeds and is expressed with power number $Po = P/(\rho \cdot n^3 \cdot D^5)$, while the impeller rotational speed is expressed with the Reynolds number $Re = D^2 \cdot n/\nu$.

The rotational impeller speed increased from 50 rpm to 650 rpm. As shown in Fig. 5, in the range Re > 110,000, the Po value for the ABT impeller stabilizes with an averaged value of Po ~ 1.75, while the average value for the standard RuT impeller when stabilized and without surface aeration is ~5.13. At Re > 150,000, the power number of the RuT impeller decreases due to surface aeration, i.e. air being sucked from the surface in the liquid. Such a hydrodynamic regime is treated as an air dispersion with a low gas holdup. In mixing with the TBT and ABT impeller, no surface aeration in the same range of impeller speeds was detected. Therefore, why the ABT power curve stabilizes at a higher Re number can be attributed

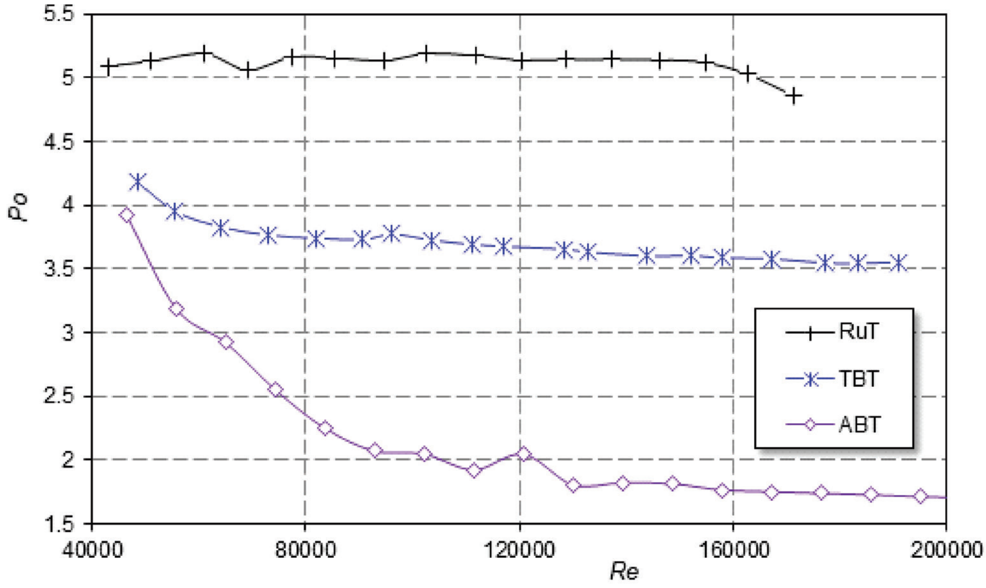

Fig. 5. *Power number of various disk impellers by mixing in water*

to its hollow blade shape; these types of impellers develop fully turbulent regime in the baffled tank at higher impeller speeds [23].

2.2 Dispersion of Air in Water

The mixing power in air dispersion is usually found to be lesser than mixing in a liquid and decreases with an increase of air flow rate. This is due to the weaker pumping capacity of the impeller, since the negative pressure region behind the blades is filled with air, i.e. so-called gas-filled cavities. With an increase in air flow, the gas cavities become greater, while the pumping capacity of the impeller becomes ever weaker. Flooding occurs when the buoyancy forces of the gas phase dominate the weak primary circulation of the impeller discharge flow. During the measurement of the mixing power, this state can be reflected as a local increase in power (with regard to the previous regime), and the corresponding relationship is marked

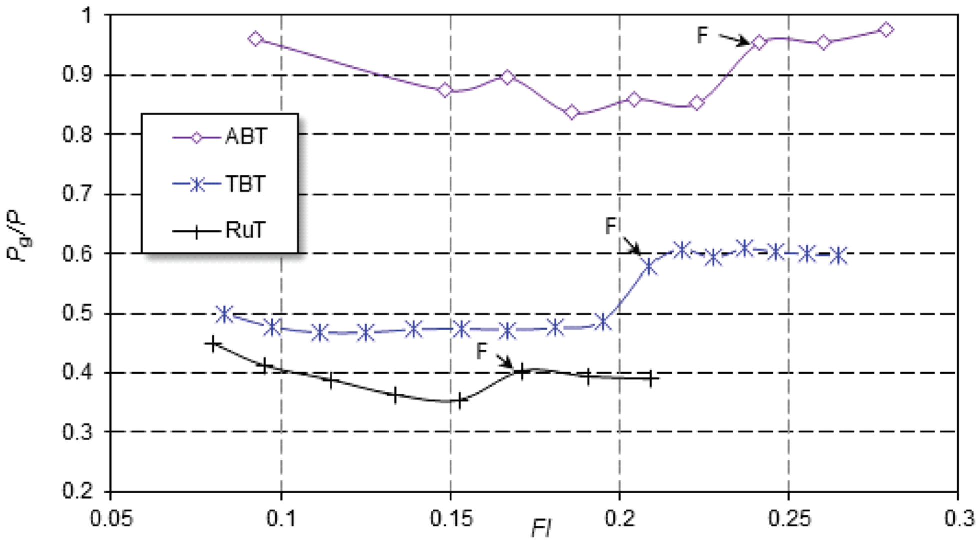

Fig. 6. *Power drawn under gassing at Fr = 0.3*

as flooding $(P_g/P)_F$ while the condition just before flooding as loading $(P_g/P)_L$, respectively, and the transition itself is the loading-to-flooding transition [16]. In Fig. 6, the ratio P_g/P is shown in air dispersion with the studied impellers in dependence on the flow number $Fl = q/(n \cdot D^3)$ at constant impeller speed expressed with Froude number $Fr = n^2 \cdot D/g$. It is obvious that the RuT impeller floods first at $Fl \sim 0.17$ while the primary circulation of the impeller discharge flow weakens with increasing gas flow rate, and the mixing power dissipation decreases by 65 %.

With a modified twisted-blade shape, the TBT impeller floods at a somewhat higher flow number $Fl \sim 0.21$, but during dispersion, there is still a 52 % decrease in power. Real improvement of gas dispersion can be seen only with the ABT impeller, which floods at $Fl = 0.24$ and shows a very small power draw under gassing: only 18 %. That means that the ABT impeller still maintains the circulation of dispersed air in the vessel even with quite higher air flow rates. Another flooding recognition method in single-impeller dispersion [16] used in our study of ABT impeller is based on the global gas holdup drop, as shown in Fig. 7. With an increase of air inflow into the liquid, the gas holdup rises to a stagnation point and soon, with a further minimal increase in the air intake, flooding

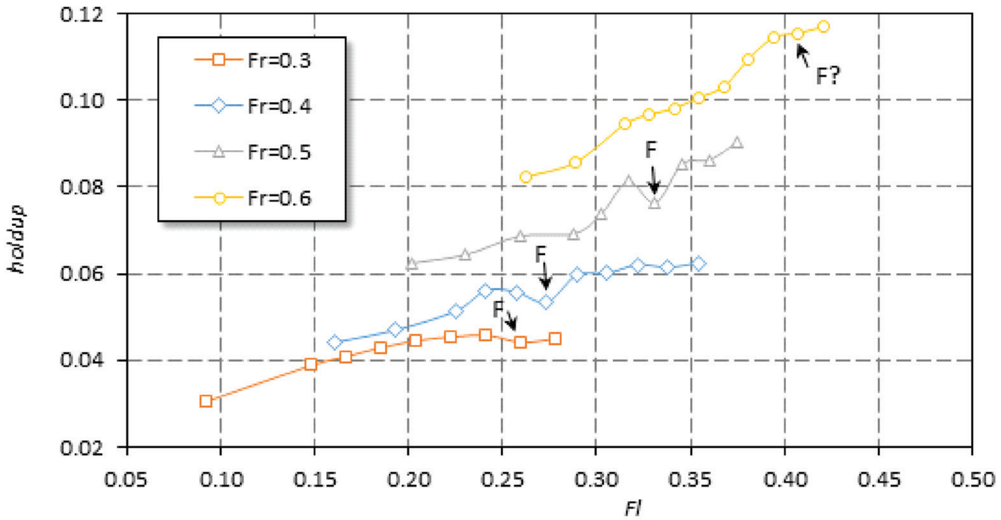

Fig. 7. *Global gas holdup of the ABT impeller depending on the flow number Fl*

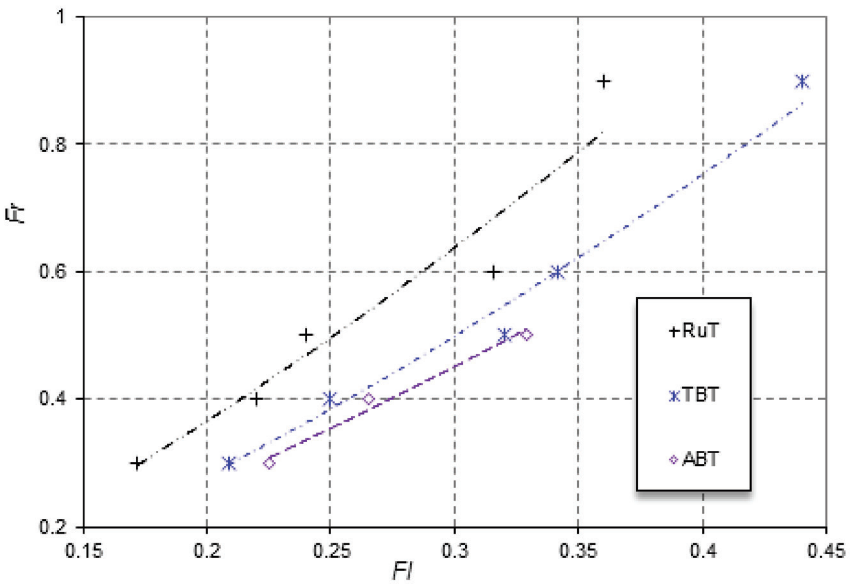

Fig. 8. *Measured LFT for the studied impellers: curves correlated according to Eq. (2)*

occurs (F). In Fig. 7, flooding conditions are shown as a local decrease in the global gas holdup and are evident at Fr = 0.3, Fr = 0.4 and Fr = 0.5, while at Fr = 0.6 no flooding was able to be detected.

Thus, on the basis of the measurement results of the studied impellers, the influence of the different disk impellers on the flooding transition can be seen in the flow map in Fig. 8. Curves represent loading to flooding transition (LFT) correlation criteria

$$Fr = k_1 \cdot Fl^{k2}, \tag{2}$$

with the coefficients k_1 and k_2 and the correlation coefficient R shown in Table 1.

Table 1. *Parameters of the regression curve by Eqs. (1) and (2)*

Impeller/coef.	*ABT*	*TBT*	*RuT*
k_1	1.912	2.786	3.340
k_2	1.216	1.429	1.375
k_3	32.64	19.913	32.978
k_4	-0.464	-0.3162	-0.378
R_{LFT}	0.991	0.991	0.976
R_{t95}	0.970	0.960	0.923

The ABT impeller is clearly capable of dispersing an even somewhat greater amount of air than the TBT impeller prior to flooding by higher impeller rotational speeds (Fr). However, the basic difference between their functioning is in the power drawn which is significantly lesser with the ABT.

2.3 Mixing Time during Liquid Mixing

The mixing times of the studied impellers were approximated according to the criteria [19] depending on the impeller power:

$$t_{95} = k_3 \cdot P^{k4}, \tag{3}$$

where the coefficients k_3 and k_4 and the correlation coefficient R are shown in Table 1.

In general, it is clearly seen that with a greater mixing power the mixing time for all given impellers is shorter, as can be seen in Fig. 9. The greater mixing power essentially represents the greater pumping capacity of the impeller and, consequently, more intensive circulation which is reflected in a shorter mixing time. The difference in the mixing time among studied disk impellers of equal *side view contour* are at the same mixing power related only to the form of the blades of individual impellers, which form and direct the impeller discharge flow. For example, it is clear that the RuT impeller mixing times are very long, even twice the times for the ABT impeller, which, of course, strongly influences the efficiency of the impeller, as will be discussed later.

The measured mixing times were compared with the results of the most cited criterion [7], [20] and [31], which was based on summarized experimental data of mixing times (t_{95}) of different impeller types:

$$t_m = 5.2\left(\frac{1}{n}\right)\left(\frac{1}{Po^{0.33}}\right)\left(\frac{T}{D}\right)^2. \tag{4}$$

According to Eq. (4), the mixing times are regarded to any impeller type in single impeller mixing by the conditions $1/3 < D/T < 1/2$ and $H = T$. A comparison of the measured values calculated using Eq. 4 shows a relatively good match with the interdependent parameters $P - t_m$, which raises the question of the meaningfulness of comparing absolute values. As can be seen from Fig. 9, the studied TBT and ABT impellers have achieved quite different mixing times by the same mixing power. Specifically, the Power number for the RuT impeller in the standard geometric configuration, according to the literature survey, is found to be between $4.8 \leq Po \leq 6.3$, which differs from our measured value with a relative discrepancy from –7 % to 23 %. Similarly, various experimental methods of determining the mixing time also differ not only on a physical basis (temperature response, pH change, change in conductivity, discoloration, etc.), but also according to the various criteria for achieving the mixing rate. Thus, the mixing rate can be reached by determination: i) $A_\infty = \pm 0.05 \cdot \Delta A$ [21] and [26] or ii) $A'_\infty = \pm 1$ % [11], ±5 % [32] and [33] or even ±10 % [34] where A represents any measured property and A' its fluctuation [29]. If we proceed from the local measurements, then we have to additionally take into account the influence of the location itself (r, z, ϕ), since the deviations between mixing times were found to be from –6 % to 11 % of the mean mixing time [11]. In general, the pulse/response method determines the minimal amount of input substance that represents a pulse. In our case, this means 1 dm^3 of hot water (as a pulse) while the pouring of water into the vessel itself takes between 0.5 s and 0.75 s and is directly included in the mixing time, while the injection times of chemicals of much smaller quantities using methods based on conductivity or pH change (injection of 3 ml of acid or salt solution, etc.), or discoloration, are considerably shorter.

The mixing time, expressed with local changes in any arbitrary property, represents only the time that a lack of homogeneity is present at a given location in the vessel, so the mixing time is only a somewhat rough evaluation of mixing quality. Therefore, for a high-quality product from the process, any difference in homogeneity of the liquid volume is of vital importance, see Fig. 13.

To analyse the mixing efficiency of an individual impeller, direct energy consumption (E - dissipated energy) can be used as a suitable estimate:

$$E = t_{95} \cdot P. \tag{5}$$

Now it is clearly seen (Fig. 10) that the mixing times of the impellers are quite different by the same dissipated energy. For the same mixing time as the ABT impeller (e.g. at 5 s), the TBT impeller dissipates approximately ~2.7 times more energy and the RuT ~ 5.2 times more. Due to all the above-mentioned preferences, i.e. a very small reduction of P_g/P under gassing, and simultaneously maintaining the circulation of a dispersed air in the vessel with quite higher air flow rates, as well as low power consumption, the ABT impeller is very suitable to be placed as the lowest impeller in the case of a multi-stage impeller for dispersing a large gas intakes into the liquid.

A commercial CFD code ANSYS Fluent 14.5 was performed by liquid mixing in a standard geometric configuration tank of equal size as the experimental device to analyse some mixing characteristics of different impeller types. The computational mesh consisted of two parts: the first one represented the stationary part (i.e. the mixing vessel with baffles of 959,040 cells), and the second one represented the rotational part formed from 86,100 cells for the RuT impeller and 327,531 cells for the ABT impeller.

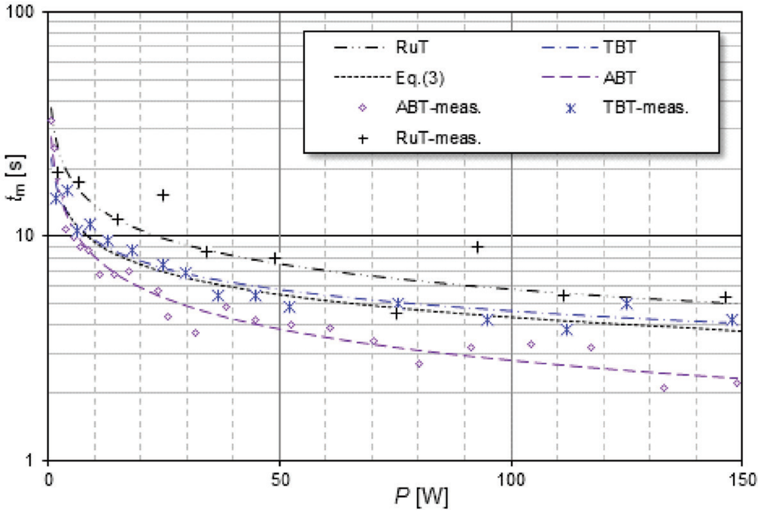

Fig. 9. *Mixing time dependence on the mixing power for various disk impellers*

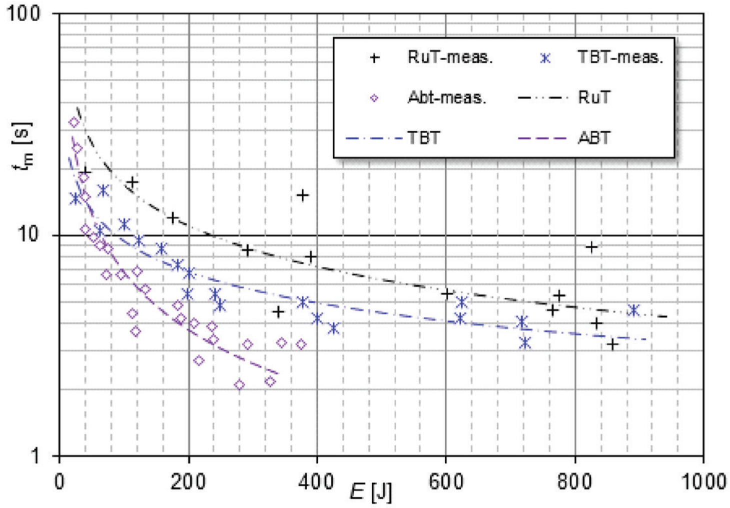

Fig. 10. *Mixing time dependence on dissipated energy of various disk impellers*

Some characteristics of the approach with *Sliding mesh* and *Reynolds stress model* for turbulence given by an impeller rotational speed of 267 rpm calculated flow field are shown in the following figures. It can be seen that, for example, how the liquid flow field and turbulent kinetic energy differ from one another during the mixing with the Rut, TBT, or ABT impeller. Turbulent kinetic energy by mixing with the RuT impeller with its discharge flow causes the greatest turbulence, as seen in the vertical *r-z* cross-section and in a cross-section at the height of the impeller disk (upper right in Fig. 11). The radially directed discharge flow from the impeller splits at the vessel wall into upper and lower circulation loops, as shown in the flow field with speed vectors shown in Fig. 12. Quite different conditions are seen with the TBT impeller; it achieved a somewhat lower turbulent kinetic energy, impeller discharge flow during mixing in water is directed axially down-wards (which completely changes with air dispersion and becomes radial) and there is one large circulation loop. The flow pattern in liquid mixing is very similar, otherwise, to the axial impellers whose main purpose is to provide an intensive circulation with the least turbulence. With the ABT impeller, the turbulent kinetic energy is much smaller and is present in a narrower area. The impeller discharge flow is radial and at the wall splits into an upper and lower circulation loop; both circulations are more intense than with the RuT impeller. The CFD calculated power number was Po_{ABT} = 1.7, which was ~3.5 % higher than the measured one. By stirring with RuT impeller, the CFD-calculated power

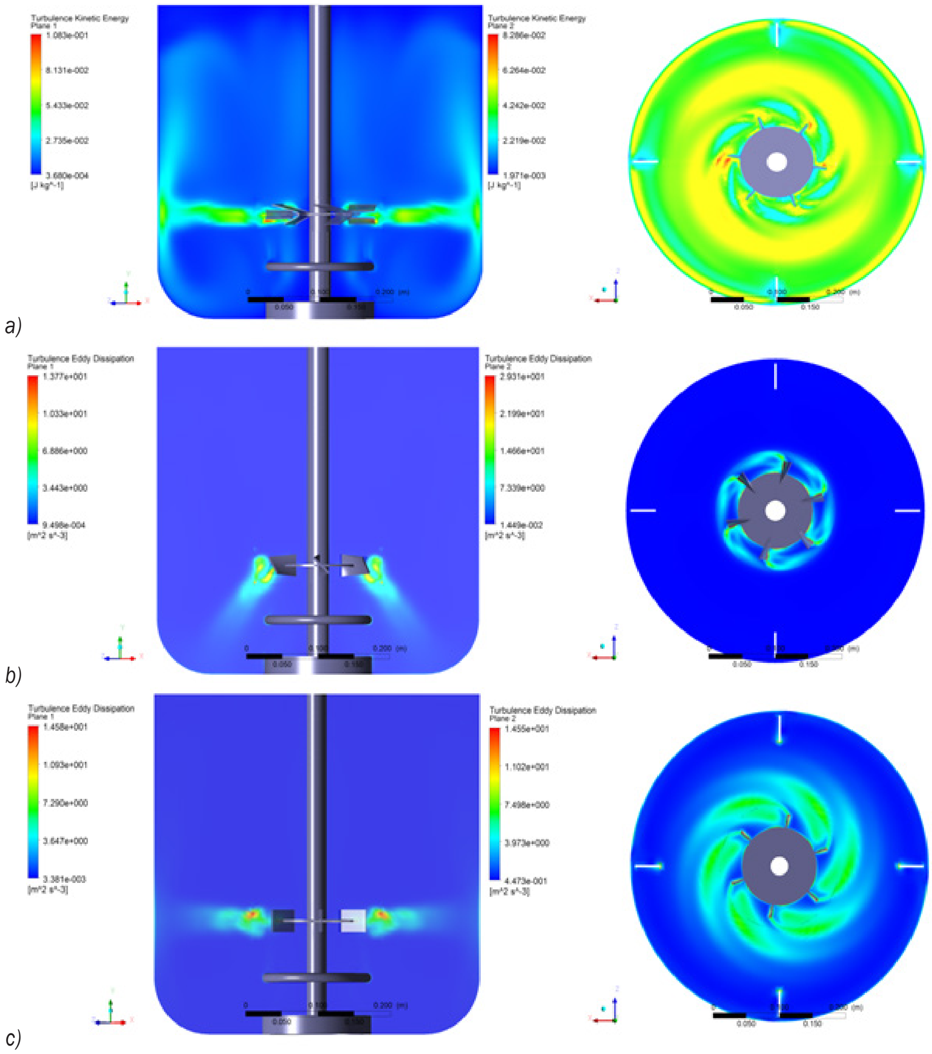

Fig. 11. *Turbulence kinetic energy by mixing with a) RuT, b) TBT, and c) ABT impellers [28]*

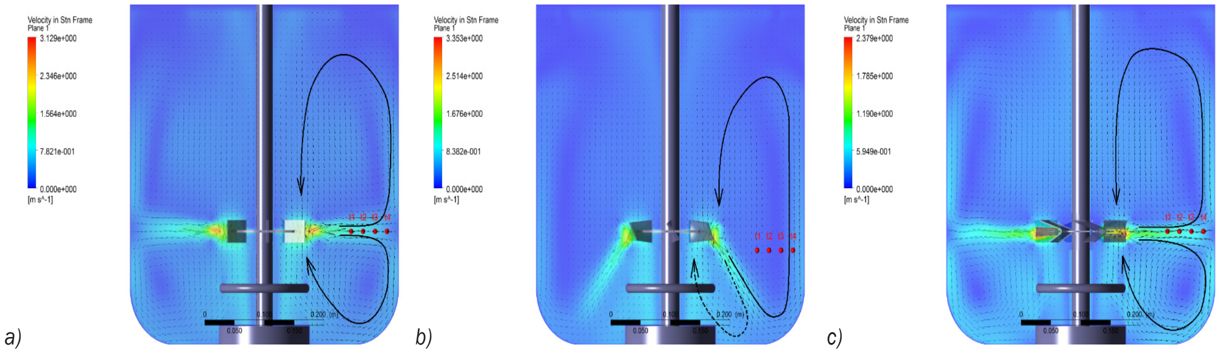

Fig. 12. *Flow field; velocity vectors for a) RuT, b) TBT, and c) ABT impellers [28]*

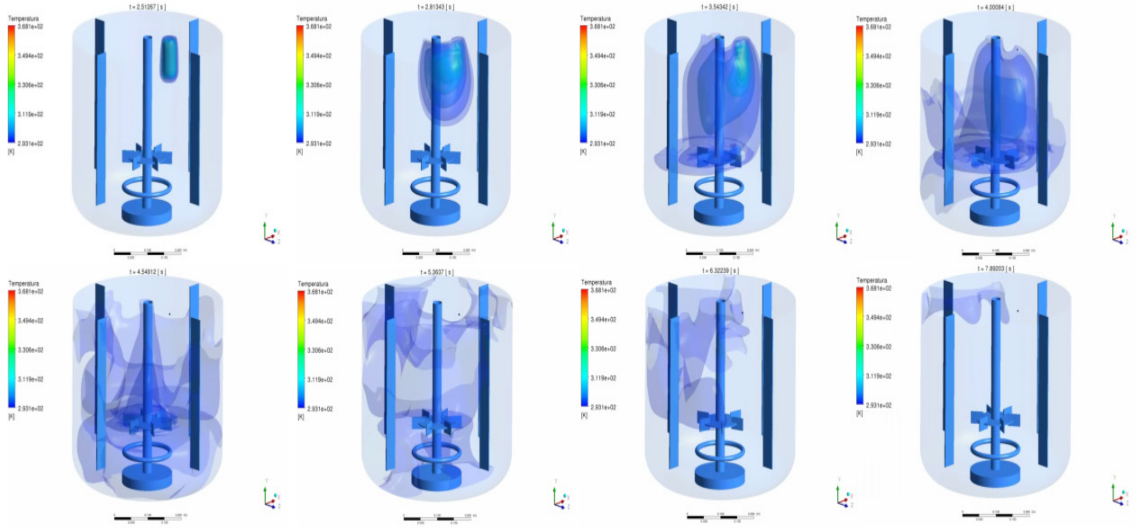

Fig. 13. *Spreading of hot water (pulse) in the flow field using the RuT impeller after 2.5 s, 2.8 s, 3.1 s, 4.0 s, 4.5 s, 5.3 s, 6.2 s, and 7.8 s [33]*

number was Po_{RuT} = 4.0 representing a 22 % lower value than the measured one, and by TBT impeller Po_{TBT} = 2.49 representing a 33 % lower value than the measured one, respectively [28]. CFD is a very useful tool to analyse a transitional phenomenon in space-time domain; which is what mixing time represents. The simulation was performed with 1 dm³ of hot water at the P1 location in the same manner as in the experiment. The spreading of the added hot water (pulse) in the *r-z* cross-section plane is shown in Fig. 13. Spreading started in the already developed flow field of water mixing with the RuT impeller by *Fr* = 0.3. The blue colour represents the state of mixing, greater than ±5 % of the final value. Looking at the mixing-over-time domain, the mixing time (expressed as the local change in any arbitrary property) represents only the time when a lack of homogeneity is present at a given location in the vessel, which confirms our assumption. This is particularly clearly seen at 6.2 s and 7.8 s, when the proposed mixing rate has already reached the marked location P1 despite the presence of inhomogeneity in the liquid in its immediate vicinity. According to measured mixing time, by the same impeller speed, which was equal to 8.5 s, the CFD-calculated mixing time was in good agreement.

3 CONCLUSIONS

This article presents the efficiency of the asymmetrically folded blade turbine (ABT) during the mixing and dispersing of air into water with a single impeller in the standard geometric configuration of the mixing vessel. To compare the efficiency of this impeller, this paper also summarizes some findings of our previous research on other disk impellers (RuT, TBT, and split blade disk turbine). The mixing power measurements were performed in liquid and in the dispersion of air into liquid by a single impeller stirring up to the eventual flooding appearance (LFT).

The power number of the ABT impeller in water mixing is low, and it's almost constant value equals $Po \sim 1.75$.

In the dispersion of air into water, the ABT impeller maintains its pumping capacity, which arises from the small power draw (less than 16 %) with the capability of dispersing much greater amounts of air (up to 53 %) than a Rushton turbine or TBT impeller.

Of all the impellers presented here, the mixing times are shortest for the ABT impellers at the same impeller power. Even more noticeable is the difference in the impeller efficiency, such that at the same mixing time of 5 s with the ABT impeller the TBT impeller dissipates approximately 3 times and the RuT impeller even 5.5 times more energy than the ABT impeller does.

Analyses of some mixing characteristics, such as liquid circulation, impeller power dissipation, mixing time and others, were also carried out using a CFD approach for specific purposes with the above-mentioned impellers. In this manner, the visualization of the flow field and other fluid dynamic characteristics can be seen very clearly; for example, spreading of hot water for a better understanding of mixing time characteristics.

4 ACKNOWLEDGEMENTS

The author would like to thank the Slovenian Ministry of Science for financial support under the current program No. P2-0162.

5 NOMENCLATURES

A arbitrary property,
A' property fluctuation,
b blade width, [m]
D impeller diameter, [m]
E impeller energy dissipation, [J]
Fl flow number, [-]
Fr froude number, [-]
g gravitational acceleration [ms^{-2}]
H liquid height in the vessel, [m]
H_g liquid height by gassing, [m]
k_1, k_2, k_3, k_4 coefficients, [-]
q gas volume flow rate, [m^{3}s^{-1}]
n rotational impeller speed, [s^{-1}]
P impeller power by liquid mixing, [W]
Po power number, [-]
P_g gassing power, [W]
R correlation coefficient, [-]
Re Reynolds number, [-]
t_{95} mixing time, [s]
T vessel diameter, [m]
t_s start time,[s]
t_f final time, [s]
t_m mixing time, [s]
r, z coordinates of r-z plane, [m]
w blade height, [m]
v kinematic viscosity, [m^{2}s^{-1}]
α_g gas holdup, [%]
ρ density, [kgm^{-3}]
ϑ temperature, [°C]

6 REFERENCES

[1] Khopkar, A.R., Tanguy, P.A. (2008). CFD simulation of gas-liquid flows in stirred vessel equipped with dual Rushton turbines: influence of parallel, merging and diverging flow configurations. *Chemical Engineering Science*, vol. 63, no. 14, p. 3810-3820, **DOI:10.1016/j.ces.2008.04.039**.

[2] Taghavi, M., Zadghaffari, R., Moghaddas, J., Moghaddas, Y. (2011). Experimental and CFD investigation of power consumption in a dual Rushton turbine stirred tank. *Chemical Engineering Research and Design*, vol. 89, no. 3, p. 280-290, **DOI:10.1016/j.cherd.2010.07.006**.

[3] Zadghaffari, R., Moghaddas, J.S., Revstedt, J. (2009). A mixing study in a double-Rushton stirred tank. *Computers & Chemical Engineering*, vol. 33, no. 7, p. 1240-1246, **DOI:10.1016/j.compchemeng.2009.01.017**.

[4] Devi, T.T., Kumar, B. (2013). Comparison of flow patterns of dual Rushton and CD-6 impellers. *Theoretical Foundations of Chemical Engineering*, vol. 47, no. 4, p. 344-355, **DOI:10.1134/S0040579513040210**.

[5] Zhang, L., Pan, Q., Rempel, G.L. (2006). Liquid phase mixing and gas hold-up in a multistage-agitated contactor with co-current upflow of air/viscous fluids. *Chemical Engineering Science*, vol. 61, no. 18, p. 6189-6198, **DOI:10.1016/j.ces.2006.06.001**.

[6] Xie, M., Xia, J., Zhou, Z., Zhou, G., Chu, J., Zhuang, Y., Zhang, S., Noorman, H. (2014). Power consumption, local and average volumetric mass transfer coefficient in multiple-impeller stirred bioreactors for xanthan gum solutions. *Chemical Engineering Science*, vol. 106, p. 144-156, **DOI:10.1016/j.ces.2013.10.032**.

[7] Magelli, F., Montante, G. Pinelli, D., Paglianti, A. (2013). Mixing time in high aspect ratio vessels stirred with multiple impellers. *Chemical Engineering Science*, vol. 101, p. 712-720, **DOI:10.1016/j.ces.2013.07.022**.

[8] Bombač, A. (2013). *Loading-Flooding Transition and Local Void Fraction Measurements on Industrial Fermentor 30 m3. Report.* University of Ljubljana, Faculty of Mechanical Engineering, Ljubljana. (in Slovene)

[9] Bombač, A., Senica, D., Žun, I. (2012). Flooding detection measurements on the pilot fermentor. *Conference Proceedings Kuhljevi dnevi*, p. 1-8. (in Slovene)

[10] Tang, W., Pan, A., Lu, H., Xia, J., Zhuang, Y., Zhang, S., Chu, J., Noorman, H. (2015). Improvement of glucoamylase

production using axial impellers with low power consumption and homogeneous mass transfer. *Biochemical Engineering Journal*, vol. 99, p. 167-176, **DOI:10.1016/j.bej.2015.03.025**.

[11] Haucine, I., Plasari, E., David, R. (2000). Effects of the stirred tank's design on power consumtion and mixing time in liquid phase. *Chemical Engineering & Technology*, vol. 23, no. 7, p. 7-15, **DOI:10.1002/1521-4125(200007)23:7<605::AID-CEAT605>3.0.CO;2-0**.

[12] Ochieng, A., Onyango, M.S. (2008) Homogenization energy in a stirred tank. *Chemical Engineering and Processing: Process Intensification*, vol. 47, no. 9-10, p. 1853-1860, **DOI:10.1016/j.cep.2007.10.014**.

[13] Barigou, M., Greaves, M. (1992). Bubble-size distributions in a mechanically agitated gas-liquid contactor. *Chemical Engineering Science*, vol. 47, no. 8, p. 2009-2025, **DOI:10.1016/0009-2509(92)80318-7**.

[14] Bao, Y., Chen, L., Gao, Z., Chen, J., (2010). Local void fraction and bubble size distributions in cold-gassed and hot-sparged stirred reactors. *Chemical Engineering Science*, vol. 65, no. 2, p. 976-984, **DOI:10.1016/j.ces.2009.09.051**.

[15] Bombač, A., Žun, I. (2006). Individual impeller flooding in aerated vessel stirred by multiple-Rushton impellers. *Chemical Engineering Journal*, vol. 116, no. 2, p. 85-95, **DOI:10.1016/j.cej.2005.10.009**.

[16] Bombač, A., Žun, I. (2002). Flooding-recognition methods in a turbine-stirred vessel. *Strojniški vestnik - Journal of Mechanical Engineering*, vol. 48, no. 12, p. 663-676.

[17] Cai Q., Dai, G. (2010). Flooding characteristics of hydrofoil impeller in a two- and three-phase stirred tank. *Chinese Journal of Chemical Engineering*, vol. 18, no. 3, p. 355-361, **DOI:10.1016/S1004-9541(10)60231-5**.

[18] Cheng, D., Wang, S., Yang, C., Mao, Z. (2017). Numerical simulation of turbulent flow and mixing in gas–liquid–liquid stirred tanks. *Industrial & Engineering Chemistry Research*, vol. 56, no. 45, p. 13050-13063, **DOI:10.1021/acs.iecr.7b01327**.

[19] Bombač, A., Žun, I. (2006). Power consumption and mixing time in stirring with modified impellers. *Proceedings of the 12th European Conference on Mixing*, p. 153-160, **DOI:10.13140/2.1.2673.2809**.

[20] Ascanio, G. (2015). Mixing time in stirred vessels: A review of experimental techniques. *Chinese Journal of Chemical Engineering*, vol. 23, no. 7, p. 1065-1076, **DOI:10.1016/j.cjche.2014.10.022**.

[21] Nienow, A.W. (1997). On impeller circulation and mixing effectiveness in the turbulent flow regime. *Chemical Engineering Science*, vol. 52, no. 15, p. 2557-2565, **DOI:10.1016/S0009-2509(97)00072-9**.

[22] Su, T., Yang, F., Li, M., Wu, K. (2018). Characterization on the Hydrodynamics of a Covering-plate Rushton Impeller. *Chinese Journal of Chemical Engineering*, in press, **DOI:10.1016/j.cjche.2017.11.015**.

[23] Ghotli, R.A., Abdul Aziz, A.R., Shaliza I., Baroutian, S., Arami-Niya, A. (2013). Study of various curved-blade impeller geometries on power consumption in stirred vessel using response surface methodology. *Journal of the Taiwan Institute of Chemical Engineers*, vol. 44, no. 2, p. 192-201, **DOI:10.1016/j.jtice.2012.10.010**.

[24] Cooke, M., Heggs, P.J. (2005). Advantages of the hollow (concave) turbine for multi-phase agitation under intense operating conditions. *Chemical Engineering Science*, vol. 60, no. 20, p. 5529-5543, **DOI:10.1016/j.ces.2005.05.018**.

[25] Ameur, H., Bouzit, M. (2012). Mixing in shear thinning fluids. *Brazilian Journal of Chemical Engineering*, vol. 29, no. 2, p. 349–358, **DOI:10.1590/S0104-66322012000200015**.

[26] Vasconcelos, J.M.T., Orvalho, S.C.P., Rodrigues, A.M.A.F., Alves, S.S. (2000). Effect of blade shape on the performance of six bladed disk turbine impellers. *Industrial & Engineering Chemistry Research*, vol. 39, no. 1, p. 203-213, **DOI:10.1021/ie9904145**.

[27] Bombač, A. (2013). *Disc Mixer with Asymmetrical Bended Blades: Patent SI 24012 (A)*. The Slovenian Intellectual Property Office, Ljubljana.

[28] Matijević, I. (2013). *Numerical Simulation of Mixing in the Agitated Vessel with Different Impellers*. Diploma work, University of Ljubljana, Faculty of Mechanical Engineering, Ljubljana.

[29] Bombač, A., Beader, D, Žun, I. (2012). Mixing times in a stirred vessel with a modified turbine. *Acta Chimica Slovenica*, vol. 59, no. 4, p. 707-721.

[30] Paul, L.E., Atiemo-Obeng A.V., Kresta M.S. (eds.) (2004). *Handbook of Industrial Mixing – Science and Practice*. John Wiley & Sons, Hoboken.

[31] Rodgers, T.L., Gangolf, L., Vannier, C., Parriaud, M., Cooke, M. (2011). Mixing times for process vessels with aspect ratios greater than one. *Chemical Engineering Science*, vol. 66, no. 13, p. 2935-2944, **DOI:10.1016/j.ces.2011.03.036**.

[32] Woziwodzki, S., Broniarz-Press, L., Ochowiak, M. (2010). Effect of eccentricity on transitional mixing in vessel equipped with turbine impellers. *Chemical Engineering Research and Design*, vol. 88, no. 12, p. 1607-1614, **DOI:10.1016/j.cherd.2010.04.007**.

[33] Matijević, I., Bombač, A., Mencinger, J., Žun, I. (2013). The comparison of calculated mixing time for two impellers with two computing methods. *Conference Proceedings Kuhljevi dnevi,* p. 113-120. (in Slovene)

[34] Bujalski, J.M., Javorski, Z., Bujalski, W., Nienow, A.W. (2002). The influence of the addition position of a tracer on CFD simulated mixing times in a vessel agitated by a Rushton turbine. *Chemical Engineering Research and Design*, vol. 80, no. 8, p. 824-831, **DOI:10.1205/026387602321143354**.

Strojniški vestnik - Journal of Mechanical Engineering 64(2018)9, 525-535

DOI:10.5545/sv-jme.2017.4993
Original Scientific Paper
Received for review: 2017-10-16
Received revised form: 2018-01-05
Accepted for publication: 2018-01-17

Water Hammer and Column Separation Induced by Simultaneous and Delayed Closure of Two Valves

Uroš Karadžić[1,*] – Marko Janković[2] – Filip Strunjaš[3] – Anton Bergant[4]
[1]University of Montenegro, Faculty of Mechanical Engineering, Montenegro
[2]Electric Power Supply Company, Montenegro
[3]Kone, Montenegro
[4]Litostroj Power d.o.o., Slovenia

Water hammer and column separation induced by simultaneous and sequential (delayed) closure of two valves may occur in industrial pipeline systems. This paper deals with such cases both experimentally and numerically. Water hammer equations are solved by the method of characteristics. Transient cavitating pipe flow is simulated by a discrete gas cavity model (DGCM) that considers unsteady skin friction. Discrete gas cavities and Zielke's convolution-based unsteady skin friction term are explicitly incorporated in the staggered grid algorithm of the method of characteristics. Experiments have been performed in a laboratory pipeline apparatus. The apparatus consists of an upstream end tank, a horizontal steel pipeline (total length 55.37 m, inner diameter 18 mm), four valve units positioned along the pipeline including the end points, and a downstream end tank. A transient event is induced either by simultaneous or sequential closure of two end valves. Numerical results are compared and verified with results of measurements. In addition, a theoretical analysis of pressure wave fronts travelling along the pipeline is also presented to clearly show profound effects of wave interactions.
Keywords: pipeline, two valves, simultaneous and delayed valve closure, water hammer, column separation, experimental setup, unsteady friction

Highlights
- *Water hammer and column separation events induced by simultaneous and sequential (delayed) closure of two valves were investigated.*
- *Experimental test rig is presented and described in detail.*
- *Discrete gas cavity model is validated against experimental results.*
- *Pressure wave fronts travelling along the pipeline for cases with and without friction and transient cavitation were analyzed theoretically.*

0 INTRODUCTION

The term hydraulic transients means a process that takes place in a physical system during the transition from one to another steady state. Knowledge of hydraulic transients and conditions that cause extreme pressures are crucial for safe and economical design of hydraulic systems. Hydraulic transients occur during opening and closing of control valves and changing of the operating mode of hydraulic turbomachinery such as turbo pumps and water turbines [1] and [2]. As a result of these changes high or low pressures are formed and transferred through the hydraulic pipe system with a speed which is close to the speed of sound in liquids. The local speed of sound is defined by the physical condition of the liquid (free air content) and pipe wall (rigid, elastic) and usually is variable in time and space. Pressure waves may have such intensity that they can lead to serious malfunctions of hydraulic system equipment and can cause significant damages and even breakdown of system components. To prevent unwanted effects of hydraulic transient events, pipeline systems must be fitted with adequate protective surge control means. The term water hammer is a synonym for rapid unsteady flow in pipelines and was named after the characteristic sound that occurs during the unsteady event and sounds like strikes with a hammer.

For understanding water hammer phenomena, except pressure changes, fluid compressibility and pipeline mechanics must be considered [1] and [2]. The side effects of water hammer are transient cavitation and column separation, unsteady skin friction, fluid-structure interaction (FSI) and viscoelastic behaviour of the pipe wall [3]. During transient events, it may happen that liquid pressure drops to the liquid vapour pressure. In this case vapour bubbles form [4]. Liquid also contains a certain amount of free and dissolved gas, and if the value of pressure in the system drops below the gas saturated pressure it leads to gas releasing from the liquid and the occurrence of gaseous cavitation [5]. Thus, formed vapour and gas bubbles can coalesce, form large pockets and cause separation of the liquid flow in the pipeline (column separation). The positive pressure waves reflected from the system boundaries (e.g., reservoir, valve,

*Corr. Author's Address: University of Montenegro, Faculty of Mechanical Engineering, Dzordza Vasingtona nn, 81000 Podgorica, Montenegro, uros.karadzic@ac.me

turbine, pump, etc.), compress the bubbles in the cavitation-flow region and progressively reduce the size of the cavity produced by column separation [4]. Cavities collapse and the re-joining of separated columns may produce very high pressures higher than the pressure initially given by the Joukowsky equation and may cause damage of the system components [1]. The value of the friction factor, which describes the resistance due to pipe-wall friction during transients, is different from its value for the steady state flow. For fast transients, the friction coefficient f can be expressed as the sum of two parts: the quasi-steady part (f_q) and the unsteady part (f_u) [6] to [8]. The unsteady part attempts to represent velocity profile changes and flow regime conversions from laminar to turbulent and vice versa [9] to [10].

The objective of this paper is to investigate and discuss water hammer and column separation effects induced by simultaneous and sequential (delayed) closure of two end valves in a simple pipeline apparatus. There are many industrial pipeline systems with multiple-valves, at least with two of them. Multiple actions of valves may induce very large or low pressure waves due to superposition of the waves [11]; therefore, engineers try to avoid it. However, there are reports on the usage of single or even multiple-check valves to attenuate column separation effects [12] and [13]. Recent investigations show that closure of two end valves may produce less severe column separation induced pressure fluctuations than the classical case with the downstream end single valve closure only [14]. In addition, different positions of the valves [15] and their controlled action (water hammer interferometer) [16] may attenuate pressure oscillations significantly.

The paper starts with mathematical tools for water hammer, transient cavitation and unsteady friction including boundary conditions and continues with the description of the experimental setup. In the second part of the paper, water hammer and column separation results from two valve closure experimental runs are compared with computed results. The paper concludes with a theoretical analysis of pressure wave fronts travelling along the pipeline for two end valve closure cases that include the effects of skin friction and transient cavitation.

1 THEORETICAL MODELLING

A simplified version of the continuity and momentum equations, neglecting the convective terms, is used to describe unsteady pipe liquid flow [1]:

$$\frac{\partial Q}{\partial t} + gA\frac{\partial H}{\partial x} + RQ|Q| = 0, \tag{1}$$

$$a^2\frac{\partial Q}{\partial x} + gA\frac{\partial H}{\partial t} = 0, \tag{2}$$

where unknown variables are piezometric head H and discharge Q; friction coefficient is defined as $R=f/(2DA)$.

Solving Eqs. (1) and (2) numerically with the method of characteristics (MOC) gives the following compatibility equations:

$$\frac{dQ}{dt} + \frac{gA}{a}\frac{dH}{dt} + RQ|Q| = 0, \tag{3}$$

$$\frac{dQ}{dt} - \frac{gA}{a}\frac{dH}{dt} + RQ|Q| = 0. \tag{4}$$

Eqs. (3) and (4) are valid along the characteristic lines $dx/dt = \pm a$ (Fig. 1).

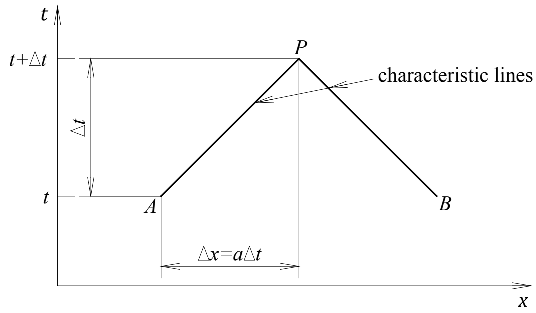

Fig. 1. *Characteristic lines in x-t plane*

It is assumed that the head, H, and discharge, Q at time t are known. These may be either initially known (i.e., at $t_0=0$, initial conditions), or they were calculated during the previous time step. It is necessary to compute the unknown values of H and Q at time $t+\Delta t$. Referring to Fig. 1, for known values of Q and H at points A and B it is necessary to determine their values at point P. Numerically solving Eqs. (3) and (4) along the lines AP and BP leads to [1]:

$$H_P = C_P - B_P (Q_u)_P, \tag{5}$$

$$H_P = C_M - B_M (Q_d)_P, \tag{6}$$

where:

$$C_P = H_A - B(Q_d)_A, \tag{7}$$

$$B_P = B - R|(Q_d)_A|, \tag{8}$$

$$C_M = H_C - B(Q_u)_B, \tag{9}$$

$$B_M = B + R|(Q_u)_B|, \tag{10}$$

where $B = a/gA$ is the pipeline characteristic impedance which depends upon the pipe properties.

Eq. (5) is referred as *the positive characteristic equation* and Eq. (6) as *the negative characteristic equation* [1].

1.1 Boundary Conditions

Boundary conditions describe relationships that define the discharge or head at a boundary, or a relationship between the head and discharge at the boundary. At the downstream end of the small-scale pipeline apparatus (Fig. 2), $x=L$, combining equations for the discharge through the ball valve V3/3H, $\boldsymbol{Q_P = C_{bv}\sqrt{\Delta H_{bv}}}$ and the needle valve V3/3C, $\boldsymbol{Q_P = C_{nv}\sqrt{\Delta H_{nv}}}$, and the positive characteristic equation, Eq. (5) gives:

$$Q_P = \frac{2C_C}{C_b + \sqrt{C_b^{\,2} + 4C_C}} \quad \text{if} \quad C_b > 0, \tag{11}$$

$$Q_P = \frac{1}{2}\left(-C_b + \sqrt{C_b^{\,2} + 4C_C}\right) \quad \text{if} \quad C_b < 0, \tag{12}$$

where:

$$C_b = \frac{C_{nv}^2 C_{bv}^2 B_P}{C_{nv}^2 + C_{bv}^{\,2}}, \quad C_c = \frac{C_{nv}^2 C_{bv}^2 C_P}{C_{nv}^2 + C_{bv}^2}. \tag{13}$$

The boundary condition at the upstream end, $x=0$, is defined by combining expressions for the discharge through the ball valve V0/3U (Fig. 2) and the negative characteristic equation, Eq. (6). Taking into account a constant pressure head in the high-pressurized tank, a quadratic equation is obtained, which roots are Eqs. (11) and (12) with:

$$C_b = C_{bv}^2 B_M, \quad C_c = C_{bv}^2\left(C_M - H_{res}\right). \tag{14}$$

1.2 Discrete Gas Cavity Model

Up to date, several mathematical and numerical models for modeling of vaporous and gaseous cavitation in pipelines have been developed. The discrete gas cavity model (DGCM) [2] is used in this paper. The DGCM can successfully simulate vaporous cavitation if the amount of a free gas in the liquid is small (gas void fraction $\alpha_g \leq 10^{-7}$) [2], [4]. The model allows gas and vapour cavities to form at all computational sections in the MOC grid. A liquid phase with a constant wave speed a is assumed to occupy the reaches connecting the computational sections. A discrete gas cavity is described by two water hammer compatibility equations (Eqs. (5) and (6)), the continuity equation for the cavity volume:

$$\frac{d\forall_g}{dt} = Q_{out} - Q_{in}, \tag{15}$$

and the ideal gas equation with the assumption of isothermal behaviour of the free gas [2]:

$$\forall_g = \alpha_g \forall\left(\frac{p_0^*}{p_g^*}\right). \tag{16}$$

A detailed description of the DGCM and its numerical solution is given in [2]. The MOC based DGCM algorithm in this paper incorporates an improved computationally effective [17] Zielke's convolution-based (with quasi-2-D weighting function) unsteady friction model [18]. Zielke's weighting function for transient laminar flow [18] and Vardy-Brown weighting functions for transient turbulent flow [19] to [21] are used in the numerical simulations.

2 EXPERIMENTAL SETUP

Experimental research was conducted in a small-scale pipeline apparatus for investigation of water hammer events including column separation and fluid-structure interaction [22].

The apparatus is comprised of a horizontal pipeline that connects the upstream end high-pressurized tank to the outflow tank (steel pipe of total length $L=55.37$ m; internal diameter $D=18$ mm; pipe wall thickness $e=2$ mm; maximum allowable pressure in the pipeline $p_{max,\,all}=25$ MPa) – see Fig. 2. Four valve units are positioned along the pipeline including the end points. The valve units at the upstream end tank (position 0/3) and at the two equidistant positions along the pipeline (positions 1/3 and 2/3) consist of two hand-operated ball valves (valves Vi/3U and Vi/3D; $i=0,1,2$) that are connected to the intermediate pressure transducer block. The air pressure in the upstream end tank can be adjusted up to 800 kPa. The pressure in the tank is kept constant during each experimental run by using a high-precision fast-acting air pressure regulator (precision class: 0.2 %) in the compressed air supply line. Four dynamic high-frequency pressure transducers are positioned within the valve units along the pipeline including the end points (see Fig. 2). Pressures $p_{0/3}$, $p_{1/3}$, $p_{2/3}$ and $p_{3/3}$ are measured by Dytran 2300V4 high-frequency piezoelectric absolute pressure transducers (pressure range: from 0 MPa to 6.9 MPa; resonant frequency: 500 kHz; acceleration compensated; discharge time constant: 10 seconds (fixed)). The datum level for all pressures measured in the pipeline and at the tank is at the top of the horizontal steel pipe (elevation 0 m in Fig. 2). The water temperature is continuously monitored by the thermometer installed in the outflow tank. The water hammer wave speed was determined as a = 1340 m/s ±10 m/s [26]. The fast closing electro-pneumatically operated ball valve (V3/3P) is controlled with filtered compressed air which is supplied through a plastic pipeline from the pressure regulator, in which the pressure is independent from the rest of the system. The transient event can be triggered by fast closing or opening of the downstream end valve, using either the V3/3P or the V3/3H. Both valves are equipped with a fast-response displacement sensor (measurement range: 0° to 90°, frequency response: >10 kHz) which measures the change of the valve angle (α) during its closing or opening. In addition, transients can be induced by closing or opening hand-operated valves along the pipeline (valves Vi/3U and Vi/3D; $i=0,1,2$). At the upstream end high-pressurized tank and at the downstream end of the pipeline, two strain-gauge pressure transducers ($p_{0/3\text{-sg}}$ and $p_{3/3\text{-sg}}$; pressure range: from 0 MPa to 1 MPa, uncertainty: ±0.5 %) are installed. These transducers are used for the evaluation of the initial conditions in the system. The needle valve (V3/3C) is used for adjustment of the initial pipe discharge. The initial discharge (velocities larger than 0.3 m/s) is measured by the electromagnetic flow meter (uncertainty: ±0.2 %). All measured data are collected by the data acquisition system (sample rate: up to 100 kHz) that is connected to a PC. In the cases presented in the paper, transients were induced by 'simultaneous' closure of 1) the hand-operated ball valve at the downstream end of the pipeline and 2) the hand-operated ball valve at the upstream end (V3/3H+V0/3U). The pressure in the upstream tank was 400 kPa and initial pipe velocities were 0.3 m/s and 2.12 m/s. This apparatus has been classified as an unsteady friction dominated apparatus [22] because the Ghidaoui's parameter [23] is close to 1. The relative importance of unsteady friction for the two case studies is indicated by the Duan's parameter [24]: $I=0.007$ for $V_0=0.30$ m/s and $I=0.05$ for $V_0=2.12$ m/s. The effects of unsteady friction for rapid transients are important when $I<0.1$.

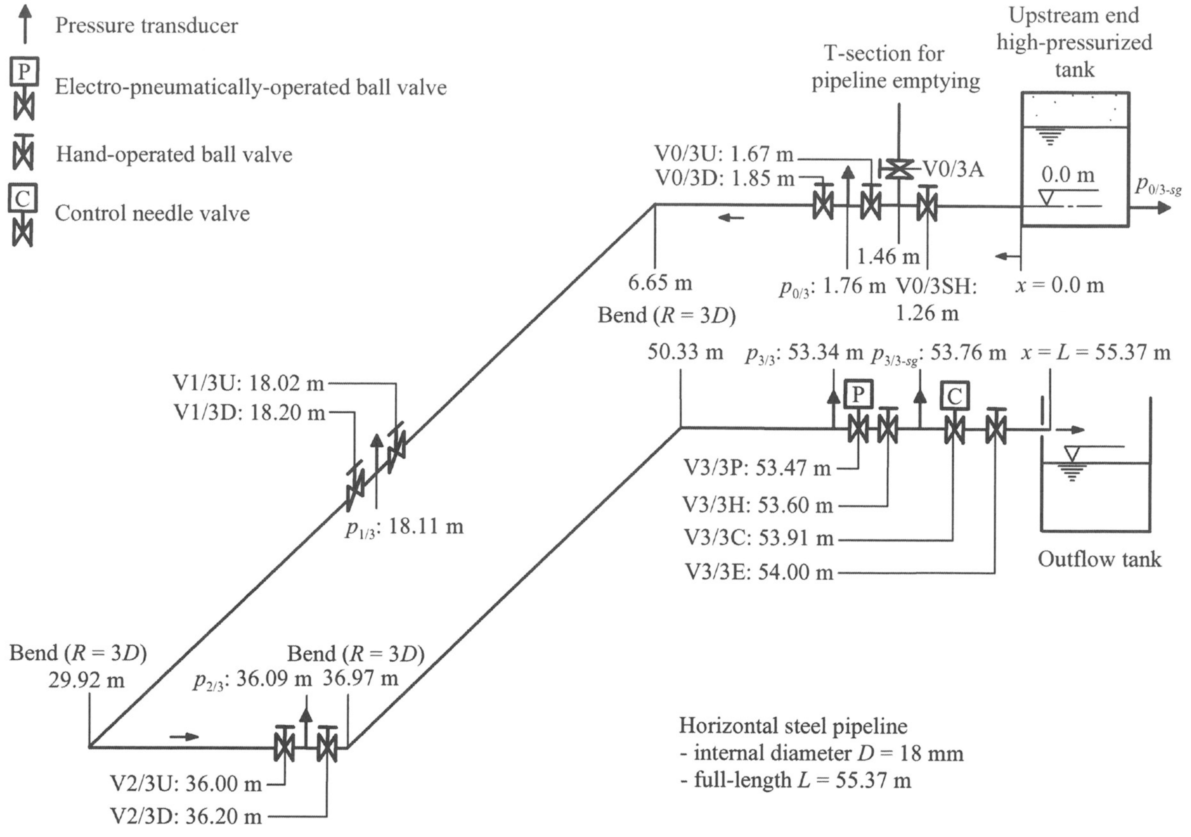

Fig. 2. *Layout of small-scale pipeline apparatus*

3 EXPERIMENTAL AND NUMERICAL RESULTS

A number of experiments have been performed in the laboratory pipe system (Fig. 2) for better understanding of unsteady flow phenomena caused by the closure of two valves. The valve closures were induced 'simultaneously' as much as possible by using valve V3/3H at the downstream end of the pipeline and valve V0/3U at the upstream end. Results from two distinct experimental runs are presented and compared with calculated results in this section: 1) water hammer case and 2) column separation case. Transients were induced first by a fast closure of the downstream end valve V3/3H and second by a delayed fast closure of the upstream end valve V0/3U. The sampling frequency for each continuously measured quantity was f_s = 3,000 Hz.

3.1 Water Hammer Case

Fig. 3 presents measured and computed pressure head traces in the laboratory pipeline apparatus ($H_{3/3}$, $H_{2/3}$, $H_{1/3}$ and $H_{0/3}$) for the rapid closure of the two valves for the initial flow velocity V_0=0.3 m/s; the effective valve closure times were much less than the wave reflection time $2L/a$=0.08 s. This experimental run represents the water hammer case (pressure head is above the vapour pressure head at all times).

The fast closure of the downstream end valve (V3/3H) produces the classical Joukowsky pressure head rise ΔH_{max} = 41.3 m. The second delayed fast closure of the upstream end valve (V0/3U) produces a pressure head rise at this valve of practically the same magnitude. The time delay between the two valve closures is 0.036 s and the time difference between the two measured maximum heads is 0.03 s (due to different valve closure times of 40 ms and 34 ms, respectively). The maximum head due to the closure of V0/3U occurs within the second water hammer time period ($L/a < t < 2L/a$). The maximum measured head H_{max} = 83.0 m occurs at the downstream end valve as a short duration pressure pulse superimposed on the third bulk pressure pulse and it is slightly larger than first bulk head of 80.0 m. Overall, there is good agreement between measured and computed results.

3.2 Column Separation Case

Fig. 4 shows measured and computed head traces in the pipeline apparatus ($H_{3/3}$, $H_{2/3}$, $H_{1/3}$ and $H_{0/3}$) for the fast closure of the two valves for the initial flow velocity V_0 = 2.12 m/s. In this case column separation

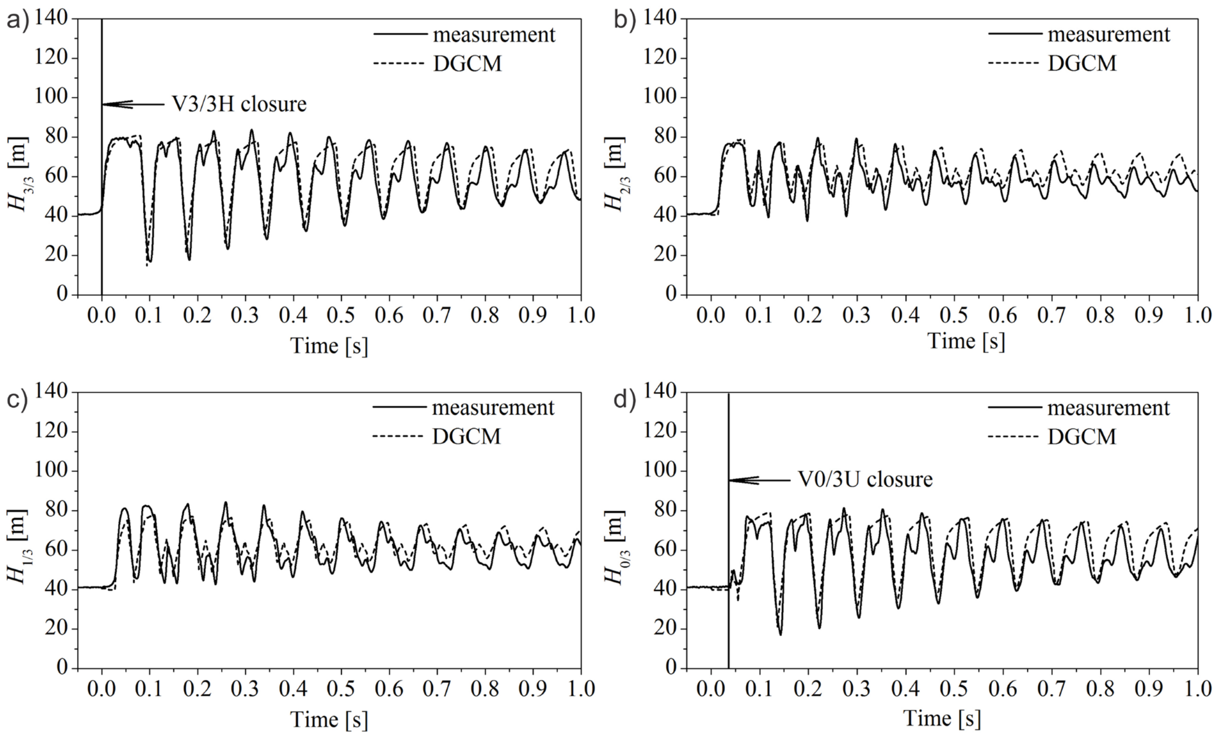

Fig. 3. *Comparison of measured and calculated heads at two end valves; a) $H_{3/3}$ and d) $H_{0/3}$ and along the pipeline; b) $H_{2/3}$ and c) $H_{1/3}$; V_0 = 0.3 m/s; p_{res} = 400 kPa; 'Simultaneous' closure of the valves V3/3H and V0/3U (slight delay)*

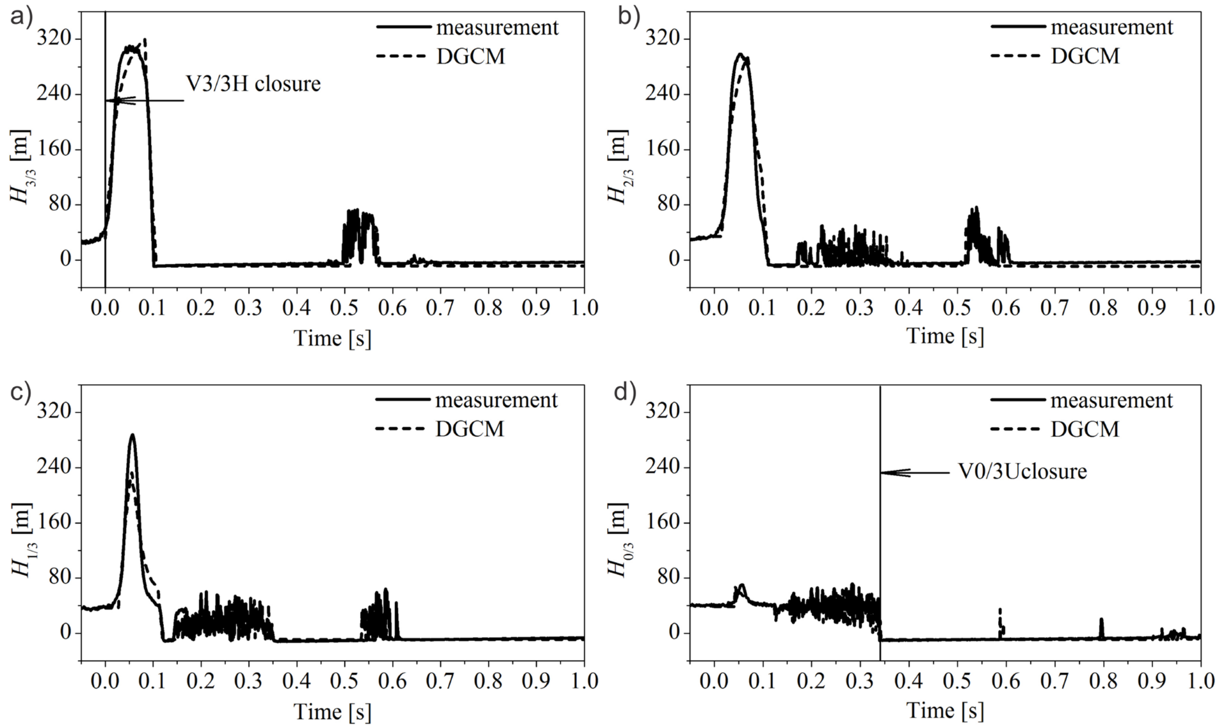

Fig. 4. *Comparison of measured and calculated heads at two end valves; a) $H_{3/3}$ and d) $H_{0/3}$ and along the pipeline; b) $H_{2/3}$ and c) $H_{1/3}$; V_0 = 2.12 m/s; p_{res} = 400 kPa; 'Simultaneous' closure of the valves V3/3H and V0/3U (delay)*

occurs in the system. Again the valve closure times were less than the wave reflection time $2L/a$ = 0.08 seconds (V3/3H: 70 ms and V0/3U: 65 ms).

The column separation case produces water hammer with column separation including large cavities and extended regions of distributed vaporous cavitation along the pipeline. The initial fast closure of the downstream end valve (V3/3H) produces the classical Joukowsky pressure head rise ΔH_{max} = 277.9 m. The second delayed fast closure of the upstream end valve (V0/3U) produces a pressure head drop from the reservoir head to the vapour pressure head of –9.8 m. The time delay between the two end valve closures is 0.34 s. At the time of the pressure drop at V0/3U the water flows from the reservoir towards the downstream end. The pressure heads along the pipeline remain practically constant at the vapour pressure head for a longer period. The first fast closure of the downstream end valve (V3/3H) produces the maximum pressure head $H_{max} = H_0 + \Delta H_{max}$ = 310.3 m in the system. The results obtained using the DGCM give pressure histories that are in good agreement with the experimental results. Reopening of one or both valves at selected time(s) after the closing periods is subject of the authors' future work.

4 THEORETICAL ANALYSIS OF PRESSURE WAVES IN FRICTIONLESS PIPE AND FRICTION DOMINATED PIPE (WATER HAMMER CASE)

Fig. 5 shows the responses of the reservoir-pipeline-valve and reservoir-valve-pipeline-valve system of Fig. 2 considering two theoretical cases: 1) the first one is an ideal frictionless system without cavitation and 2) the second one is system without cavitation but with consideration of unsteady skin friction (water hammer case). The steady flow is stopped 1) by instantaneous downstream end valve closure and 2) by instantaneous simultaneous or sequential (delayed) two end valve closures. The initial flow conditions are the same as for the water hammer case in Section 3.1 with the initial flow velocity V_0 = 0.30 m/s. Figs. 5a and b show the case of V3/3H valve closure (V0/3U stays open). The unsteady friction obviously produces attenuation of pressure waves and also rounds pressure pulses. Comparison of quasi-steady and unsteady friction effects has been previously shown in **[11]**. Timing of the pressure waves is practically unaffected by friction effects. The pressure at the position x/L = 0 has a constant value equal to the reservoir pressure. Effects of unsteady friction show similar behavior for the case of the simultaneous closure of the two valves

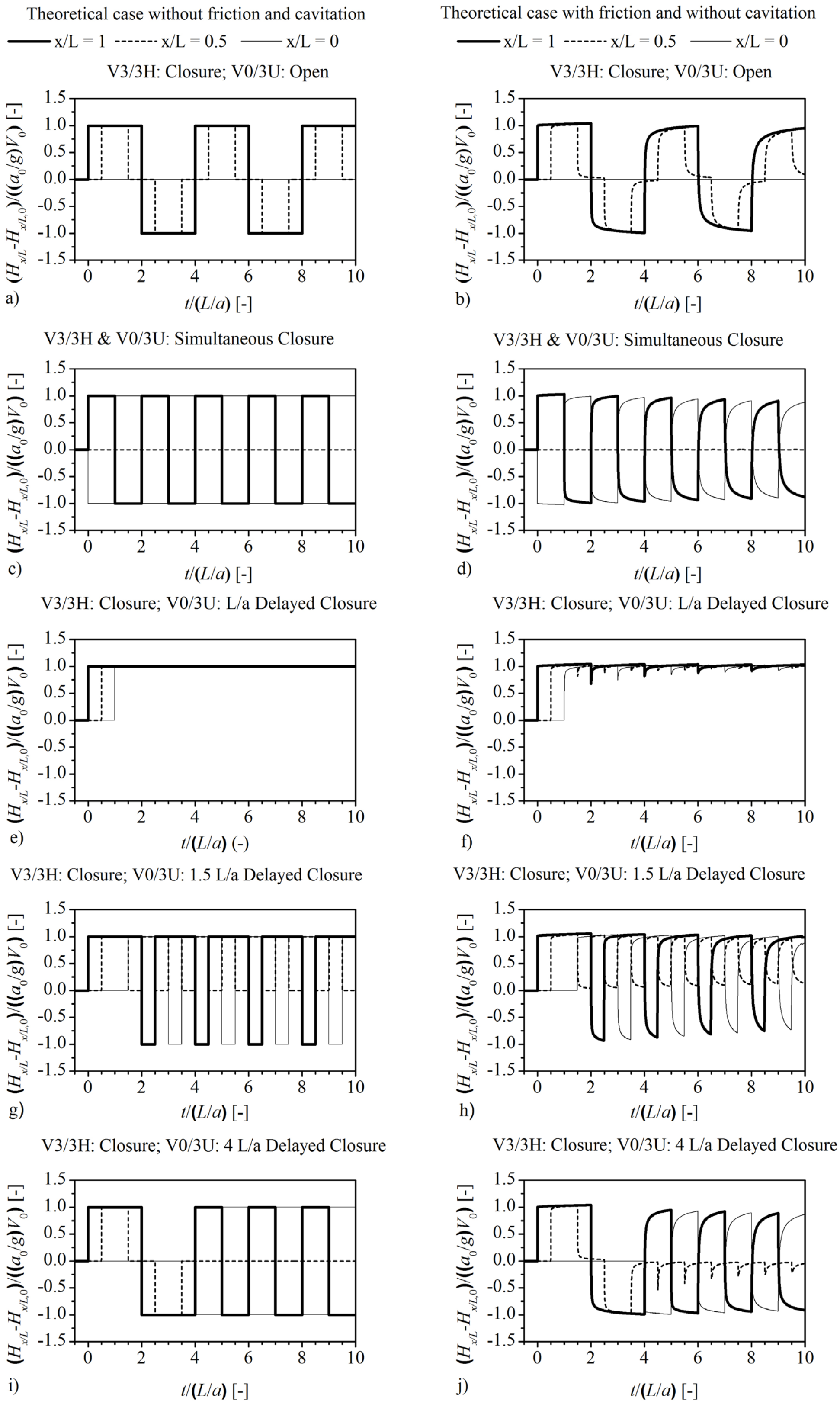

Fig. 5. *Comparison of theoretical dimensionless heads (without and with friction) at the end valves (x/L = 1 and 0) and at the midpoint (x/L = 0.5); V_0 = 0.3 m/s; p_{res} = 400 kPa*

(Figs. 5c and 5d). In this case the pressure at x/L = 0.5 is constant at all times and equal to the reservoir pressure. Pressure variations at the two valves occur with a period of $2L/a$. The case when V0/3U is closed instantaneously at time L/a after V3/3H closure is shown in Figs. 5e and 5f. After V3/3H instantaneous closure a high-pressure wave is formed that travels towards V0/3U. At the time L/a this high pressure wave arrives at the reservoir and at this instant V0/3U is closed resulting in "trapped" constant high pressure in the pipeline (Fig. 5e). Due to frictional effects some small pressure drops are detected in the pipeline after V0/3U closure (Fig. 5f) which attenuate rapidly. The liquid in the pipeline now is at standstill condition. Delayed closure of valve V0/3U at the time 1.5 L/a after closure of V3/3H is shown in Figs. 5g and h. In this case the pressure wave, formed by V3/3H closure, travels towards the upstream end reservoir, reflects back and passes the midpoint of the pipeline when V0/3U instantaneous closure occurs at the time $1.5L/a$. At this moment the liquid is flowing towards the reservoir and closure of the V0/3U causes the occurrence of the second positive pressure wave that travels in the same direction as the first pressure wave but with a delay of $0.5L/a$. At the midpoint the pressure changes from initial to high pressure with the period $0.5L/a$. The unsteady friction effects are similar to the previous cases.

The second valve closure with time delay $4L/a$ is the case that is a combination of the classical water hammer case ($0 \leq t \leq 4L/a$) and the simultaneous two valve closure case ($t > 4L/a$) (Fig. 5i). An interesting situation is at x/L = 0.5 where some negative pressure spikes can be noticed in the case with friction (Fig. 5j). This can be explained as follows. There are two pressure waves, first is the pressure wave initiated by the first valve closure (V3/3H) and the second pressure wave initiated by closure of V0/3U at $t = 4L/a$. When the second wave is generated, the first pressure wave has already been attenuated due to friction. When they meet at x/L = 0.5 the second pressure wave has a larger value than the first pressure wave and after their interference a short-duration pressure drop occurs. After a certain amount of time, due to friction, this pressure spike disappears. In the case without friction (Fig. 5i) both pressure waves have the same value when they meet; therefore, their superposition just cancels each other. This comprehensive theoretical analysis of unsteady friction effects in the two valve closure case is new in the literature.

5 THEORETICAL ANALYSIS OF PRESSURE WAVES IN FRICTIONLESS PIPE AND FRICTION DOMINATED PIPE INCLUDING EFFECTS OF CAVITATION (COLUMN SEPARATION CASE)

Far more complex is the case with transient cavitating pipe flow (column separation). Comparison of theoretical dimensionless heads without and with consideration of unsteady friction is shown in Fig. 6. As for the water hammer case, (Section 4), the steady flow is stopped 1) by instantaneous downstream end valve closure and 2) by instantaneous simultaneous or sequential (delayed) closure of two end valves. The initial flow conditions are the same as for the column separation case in Section 3.2 with the initial flow velocity V_0 = 2.12 m/s.

The effects of cavitation and unsteady friction for the case of V3/3H closure (V0/3U stays open) are depicted in Figs. 6a and b. It is obvious that cavitation limits the minimum pressure head to the liquid vapour pressure head at the position x/L = 1 where cavitation starts at $2L/a$. The pressure head at x/L = 0 stays at the reservoir pressure head at all times. The pressure head at x/L = 0.5, after cavitation starts at the time $2.5L/a$, fluctuates between the initial and the vapour pressure head with a period of L/a. No doubts that cavitation has a predominant effect on the pressure response. For the case of the simultaneous closure of the two valves (Figs. 6c and d) the effects of cavitation play a major role again. Unsteady friction contributes to slight attenuation and timing of bulk pressure pulses. Naturally the minimum pressure heads along the pipeline are limited to the liquid vapour pressure head. As described previously in Section 4, instantaneous V0/3U closure at time L/a after V3/3H closure results in a constant high pressure along the pipeline. Therefore, cavitation does not appear in this case and this is clearly depicted in Figs. 6e and f. System response for the case of 1.5 L/a delayed V0/3U closure after V3/3H is closed is even more profound (Figs. 6g and h). The pressure response at x/L = 1 and x/L = 0 is similar with a delay of L/a to each other. At x/L = 0.5 (midpoint of the pipeline) cavitation occurs at time $3L/a$ and lasts for $0.5L/a$. After that no cavitation exists at the midpoint. The second valve closure with a time delay of $4L/a$ produces longer periods of cavitation existence along the pipeline (Figs. 6i and j). At x/L = 1 cavitation starts at time $2L/a$ and lasts until $7.5L/a$. At x/L = 0 cavitation also occurs at $2L/a$ after V0/3U is closed and exists for a longer period. Similar behaviour can be observed at the midpoint of the pipeline too. Finally, the two valve closure case with cavitation exhibits its profound effect on pressure

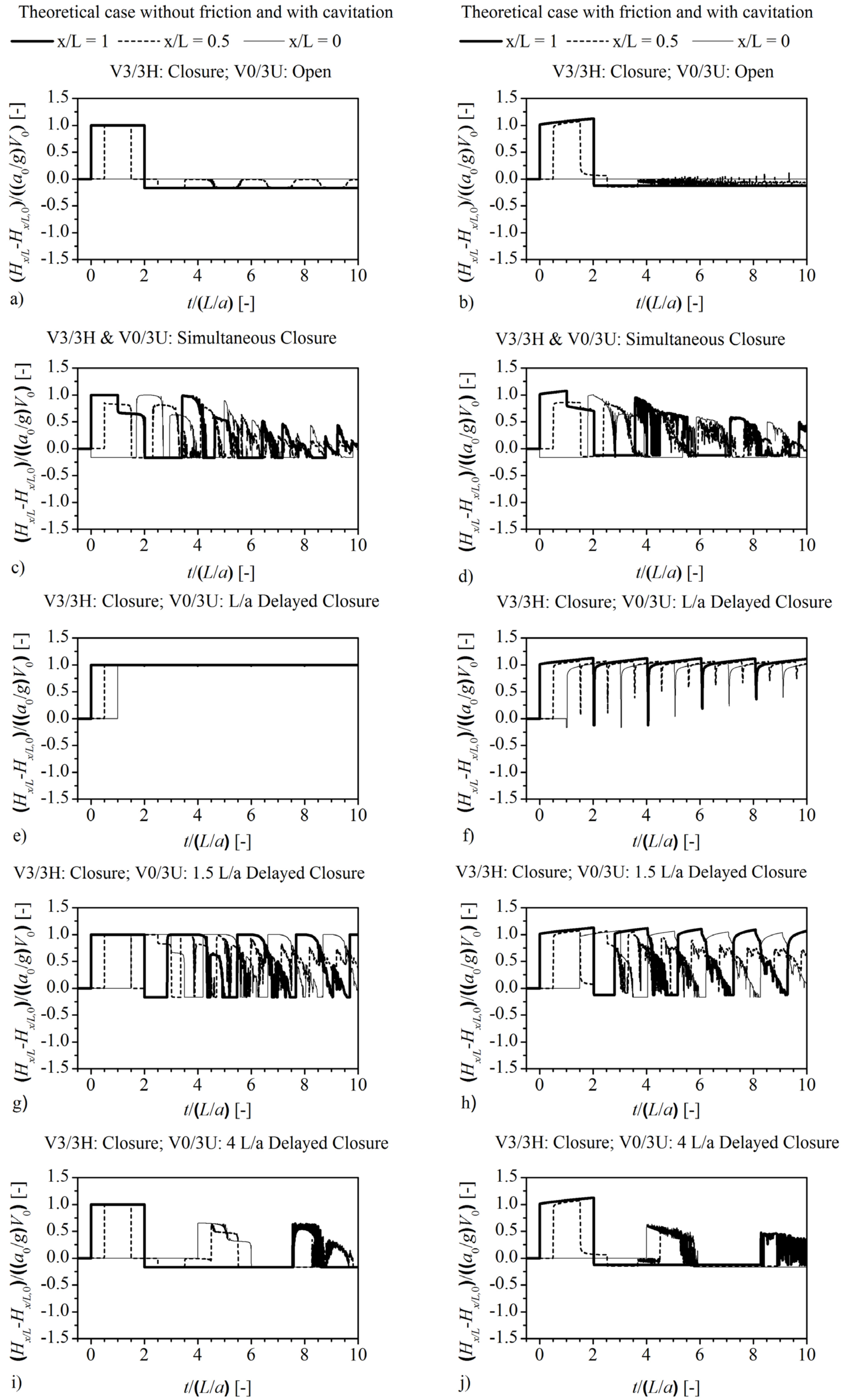

Fig. 6. *Comparison of theoretical dimensionless heads (without and with friction) at the end valves (x/L = 1 and 0) and at the midpoint (x/L = 0.5); V_0 = 2.12 m/s; p_{res} = 400 kPa*

response while unsteady friction only slightly affects the amplitude, shape and timing of the pressure pulses.

7 CONCLUSIONS

Water hammer and column separation effects triggered by simultaneous and sequential (delayed) closure of two end valves have been investigated in a laboratory pipeline apparatus. A numerical discrete gas cavity model (DGCM) with inclusion of the convolution-based unsteady friction term has been successfully validated against the investigated experimental runs including water hammer and column separation cases. Finally, a novel theoretical analysis of pressure wave fronts travelling along the pipeline triggered by simultaneous and delayed closure of the two end valves for cases without and with friction and transient cavitation has been presented. It has been shown that unsteady friction affects rounding and attenuation of pressure head pulses but has no major impact on their timing. Effects of cavitation on pressure histories are far more profound because they include liquid rupture, waves and shocks. Depending on the second valve closure delay cavitation may be a long or short lasting event. In some cases (V0/3U, L/a delayed closure) cavitation does not occur at all.

In the near future, the authors are planning to improve the experimental setup by installing one additional fast closing electro-pneumatically operated ball valve instead of V0/3U and a new PLC (programmable logic controller). In this way simultaneous and controlled sequential closure of the two electro-pneumatically operated ball valves will be possible thus enabling further experimental, numerical and theoretical investigations in the relatively new field of controlled multiple valve actions in pipelines.

8 NOMENCLATURES

A cross-sectional area, [m^2]
a wave speed, [m/s]
B pipeline characteristic impedance, [m^{2}s]
B_M constant of positive characteristic equation, [m/(m^3/s)]
B_P constant of negative characteristic equation, [m/(m^3/s)]
C discharge coefficient, [-]
C_M constant of positive characteristic equation, [m]
C_P constant of negative characteristic equation, [m]
D pipe internal diameter, [m]
E Young's modulus of elasticity, [N/m^2]
e pipe wall thickness, [m]
f friction coefficient, [-]
f_s sampling frequency, [Hz]
g gravitational acceleration, [m/s^2]
H piezometric head (head)
I Duan's parameter, [-]
L length, [m]
N number of computational reaches, [-]
p pressure, [N/m^2]
Q discharge, [m^3/s]
R friction coefficient, pipe bend radius, [1/m^3], [m]
V flow velocity, [m/s]
x axial distance, [m]
α valve opening angle , [°]
α_g volume fraction of gas in mixture with a fluid, [-]
ΔH losses at the valve, pressure head increase, [m]
$\forall$ volume, [m^3]

Subscripts:
0 initial conditions
d downstream
bv ball valve
g gas
in inlet
max maximum value
nv needle valve
out outlet
q quasi-steady
res reservoir
u unsteady, upstream

9 ACKNOWLEDGEMENTS

The authors gratefully acknowledge the support of the Ministry of Science of Montenegro (MSM) and of the Slovenian Research Agency (ARRS) through the projects BI-ME/14-15-016 (MSM, ARRS) and L2-5491 (ARRS).

10 REFERENCES

[1] Chaudhry, M.H. (2014). *Applied Hydraulic Transients. 3rd ed.*, Springer, New York, **DOI:10.1007/978-1-4614-8538-4**.
[2] Wylie, E.B., Streeter, V.L. (1993). *Fluid Transients in Systems. Prentice-Hall*, Englewood Cliffs.
[3] Bergant, A., Tijsseling, A.S., Vítkovský, J.P., Covas, D.I.C., Simpson, A.R., Lambert, M.F. (2008). Parameters affecting water wave attenuation, shape and timing. Part 1: *Mathematical tools. Journal of Hydraulic Research*, vol. 46, no. 3, p. 373-381, **DOI:10.3826/jhr.2008.2848**.
[4] Bergant, A., Simpson, A.R., Tijsseling, A.S. (2006). Water hammer with column separation: A historical review. *Journal of Fluids and Structures*, vol. 22, no. 2, p. 135-171, **DOI:10.1016/j.jfluidstructs.2005.08.008**.
[5] Kessal, M., Bennacer, R. (2005). A new gas release model for a homogeneous liquid gas mixture flow in pipelines.

International Journal of Pressure Vessels and Piping, vol. 82, no. 9, p. 713-721, **DOI:10.1016/j.ijpvp.2005.03.005**.

[6] Vardy, A.E. (1980). Unsteady flow: fact and friction. *Proceedings of the 3rd International Conference on Pressure Surges*, p. 15-26.

[7] Vardy, A.E., Brown, J.M.B. (2010). Evaluation of unsteady wall shear stress by Zielke's method. *Journal of Hydraulic Engineering*, vol. 136, no. 7, p. 453-456, **DOI:10.1061/(ASCE)HY.1943-7900.0000192**.

[8] Meniconi, S., Duan, H.F., Brunone, B., Ghidaoui, M.S., Lee, P.J., Ferrante, M. (2014). Further developments in rapidly decelerating turbulent flow modelling. *Journal of Hydraulic Engineering*, vol. 140, no. 7, p. 04014028−1-9, **DOI:10.1061/(ASCE)HY.1943-7900.0000880**.

[9] Pezzinga, G., Brunone, B. (2006). Turbulence, friction and energy dissipation in transient pipe flow. Brocchini, M., Trivellato, F. (eds.), *Vorticity and Turbulence Effects in Fluid Structure Interaction*, WIT Press, Southampton, p. 213-236, **DOI:10.2495/978-1-84564-052-1/09**.

[10] He, S., Ariyaratne, C., Vardy, A.E. (2008). A computational study of wall friction and turbulence dynamics in accelerating pipe flows. *Computers & Fluids*, vol. 37, no. 6, p. 674-689, **DOI:10.1016/j.compfluid.2007.09.001**.

[11] Bergant, A., Karadžić, U. (2015). Developments in valve-induced water-hammer experimentation in a small-scale pipeline apparatus. *Proceedings of the 12th International Conference on Pressure Surges*, p. 639-652.

[12] Karney, B.W., Simpson, R.A. (2007). In-line check valves for water hammer control. *Journal of Hydraulic Research*, vol. 45, no. 4, p. 547-554, **DOI:10.1080/00221686.2007.9521790**.

[13] Dudlik, A., Schönfeld, S.B.H., Schlüter, S., Prasser, M.H. (2004). ABS-Armaturen für Rohrleitungen. *Hydraulisches Bremssystem vermeidet Druckstöße und Kavitationschläge.* P&A Kompendium 2004, p. 203-205.

[14] Bergant, A., Karadžić, U., Tijsseling, A. (2017). Developments in multiple-valve pipeline column separation control. *IOP Conf. Series: Journal of Physics: Conference Series*, vol. 813, no. 1, **DOI:10.1088/1742-6596/813/1/012015**.

[15] Ikeo, S., Kobori, T. (1975). Water hammer caused by valve stroking in a pipe line with two valves. *Bulletin of JSME*, vol. 18, no. 124, p. 1151-1157, **DOI:10.1299/jsme1958.18.1151**.

[16] Bergant, A. (2016). Principles of water hammer interferometer. *Journal of Energy Technology*, vol. 9, no. 4, p. 11-20.

[17] Vítkovský, J.P., Stephens, M., Bergant, A., Lambert, M.F., Simpson, A.R. (2004). Efficient and accurate calculation of Zielke and Vardy-Brown unsteady friction in pipe transients. *Proceedings of the 9th International Conference on Pressure Surges*, p. 405-419.

[18] Zielke, W. (1968). Frequency-dependent friction in transient pipe flow. *Journal of Basic Engineering*, vol. 90, no. 1, p. 109-115, **DOI:10.1115/1.3605049**.

[19] Vardy, A.E., Brown, E.B. (2003). Transient turbulent friction in smooth pipe flows. *Journal of Sound and Vibration*, vol. 259, no. 5, p. 1011-1036, **DOI:10.1006/jsvi.2002.5160**.

[20] Vardy, A.E., Brown, J.M.B. (2004). Transient turbulent friction in fully rough pipe flows. *Journal of Sound and Vibration*, vol. 270, no. 1-2, p. 233-257, **DOI:10.1016/S0022-460X(03)00492-9**.

[21] Vardy, A.E., Brown, J.M.B., He, S., Ariyaratne, C., Gorji, S. (2015). Applicability of frozen-viscosity models of unsteady wall shear stress. *Journal of Hydraulic Engineering*, vol. 141, no. 1, p. 1-13, **DOI:10.1061/(ASCE)HY.1943-7900.0000930**.

[22] Karadžić, U., Bulatović, V., Bergant, A. (2014). Valve-induced water hammer and column separation in pipeline apparatus. *Strojniški vestnik - Journal of Mechanical Engineering*, vol. 60, no. 11, p. 742-754, **DOI:10.5545/sv-jme.2014.1882**.

[23] Ghidaoui, M.S, Mansour, S.G.S., Zhao, M. (2002). Applicability of quasisteady and axisymmetric turbulence models in water hammer. *Journal of Hydraulic Engineering*, vol. 128, no. 10, p. 917-924, **DOI:10.1061/(ASCE)0733-9429(2002)128:10(917)**.

[24] Duan, H.-F., Ghidaoui, M.S, Lee, P.J., Tung, Y.K. (2012). Relevance of unsteady friction to pipe size and length in pipe fluid transients. *Journal of Hydraulic Engineering*, vol. 138, no. 2, p. 154-166, **DOI:10.1061/(ASCE)HY.1943-7900.0000497**.

Strojniški vestnik - Journal of Mechanical Engineering 64(2018)9, 536-542

DOI:10.5545/sv-jme.2017.5183
Original Scientific Paper
Received for review: 2017-12-28
Received revised form: 2018-05-16
Accepted for publication: 2018-06-06

Analysis of Flow in a Curved Channel Using the Curvilinear Orthogonal Numerical Mesh

Mario Krzyk* – Matjaž Četina
University of Ljubljana, Faculty of Civil and geodetic Engineering, Slovenia

Along the flow in a curved channel, energy losses occur due to external influences on the considered water body and due to the internal friction caused by the turbulent flow of water. In practice, free surface flow is often calculated by using two-dimensional depth-averaged mathematical models. The mathematical model PCFLOW2D-ORTHOCURVE was built to analyse the flow in steep curved streams. It is based on the orthogonal curvilinear numerical mesh. Before the application of the model on examples of complex geometry natural flows, its accuracy was verified in the case of flow in a semi-circular curved channel. A 20 m wide channel with a curvature radius of 30 m in the axis and the horizontal bottom of the channel was applied. There were straight channel sections of 100 m before and behind the curve, respectively. The roughness coefficient of the channel was negligibly small, thus eliminating the impact of bottom and banks on the flow and energy losses. The flow depth distribution was calculated for different average flow velocities in the curve of approximately 1 m/s to about 9 m/s. The critical depth, the depth of water at the upstream and downstream boundaries of the straight section of the channel, and the mean velocity of the flow in the curved section were determined, by means of which the theoretical value of the transverse slope of free surface was calculated. This was compared with the numerically calculated value.

Keywords: flow in a curved channel, two-dimensional mathematical model, orthogonal curvilinear co-ordinates, depth averaged flow, PCFLOW2D-ORTHOCURVE

Highlights

- *Two-dimensional depth averaged mathematical model was used.*
- *Mathematical model based on Cartesian coordinate system was transformed to the mathematical model based on curvilinear orthogonal numerical mesh.*
- *Flow in semi-circular channel with rectangular cross-section was analyzed.*
- *Transversal slope of the free surface in the curved section of the channel calculated by mathematical model was compared with theoretical solution.*
- *Very good agreement was reached.*

0 INTRODUCTION

Flows in steep natural channels are usually very dynamic, which is a consequence of the channels' distinctly irregular shape and nonuniform course. The mathematical modelling of such flows, using the computational mesh based on the Cartesian coordinate system, is rather irrational and can cause inaccurate results and instability of the calculation procedure [1]. The use of curvilinear coordinates allows for better adjustments to the channel shape and profile. The PCFLOW2D mathematical model [2], based on the Cartesian numerical mesh, was upgraded by using the hydrodynamic equations derived for the orthogonal curvilinear coordinate system. This expanded the model's applicability to solving practical problems that require very fine discretisation due to the morphology of the channel bed and banks. There are two more advantages to using such an approach:

- it allows the impact of the centrifugal force in curved sections to be taken into account,
- because of the improved alignment of the numerical mesh with the flow direction it is possible to avoid computational errors due to excess numerical diffusion.

This paper shows flow equations and the applicable turbulence model used in the PCFLOW2D-ORTHOCURVE model. Prior to applying the model on examples of complex geometry natural flows, its accuracy was verified on the case of a flow in a semi-circular curved channel with a rectangular cross-section. The results were compared against the theoretical equation for calculating the transverse water surface slope in a curve.

In recent literature, examples of flow analysis in the bend using an analytic depth averaged two-dimensional (2D) model [3] or using various numerical approaches, including a gene expression programming model [4], can be found. These are examples of flow in the bend of 90°. Several analysis were also performed on flow in a confluent meander bend channel using large eddy simulations [5]. Due to the length of flow in such curved channel, under

*Corr. Author's Address: University of Ljubljana, Faculty of Civil and Geodetic Engineering, Jamova 2, Ljubljana, Slovenia, mkrzyk@fgg.uni-lj.si

certain hydrodynamic conditions it is not possible to establish a parallel depth along the inner and outer edge of the channel. Therefore, a channel with a curve of 180° was used. Also, in such channel geometry it is easier to avoid the influence of the inlet and outlet hydrodynamic characteristics on the flow in the bend.

1 MATHEMATICAL MODEL EQUATIONS

As analysis was focused on 2D depth-averaged flow, the definition of two coordinate axes in the horizontal plane (ξ, η) will be sufficient. The meaning of Lame's coefficients m_ξ and m_η [6] used in the equations is evident from Fig. 1. The basic hydrodynamic equations used in the model based on the orthogonal curvilinear coordinate system are given below.

The continuity, Eq. (1) and momentum equations, (Eqs. (2) and (3)) describing a two-dimensional unsteady depth averaged flow are written in the conservative form.

$$\frac{\partial h}{\partial t}+\frac{\partial\left(hu_\xi\right)}{m_\xi\partial\xi}+\frac{\partial\left(hv_\eta\right)}{m_\eta\partial n}+\frac{hu_\xi}{m_\xi m_\eta}\frac{\partial m_\eta}{\partial\xi}$$
$$+\frac{hv_\eta}{m_\xi m_\eta}\frac{\partial m_\xi}{\partial\eta}=0, \tag{1}$$

$$\frac{\partial hu_\xi}{\partial t}+\frac{\partial\left(hu_\xi^2\right)}{m_\xi\partial\xi}+\frac{\partial\left(hu_\xi v_\eta\right)}{m_\eta\partial n}+2\frac{hu_\xi v_\eta}{m_\xi m_\eta}\frac{\partial m_\xi}{\partial\eta}$$
$$+\left(u_\xi^2-v_\eta^2\right)\frac{h}{m_\eta}\frac{\partial m_\eta}{m_\xi\partial\xi}=$$
$$-gh\frac{\partial h}{m_\xi\partial\xi}-gh\frac{\partial z_b}{m_\xi\partial\xi}-ghn^2\frac{u_\xi\sqrt{u_\xi^2+v_\eta^2}}{h^{4/3}}$$
$$+\frac{1}{m_\xi m_\eta}\left[\frac{\partial}{\partial\xi}\left(h\upsilon_{ef}\frac{m_\eta}{m_\xi}\frac{\partial u_\xi}{\partial\xi}\right)+\frac{\partial}{\partial\eta}\left(h\upsilon_{ef}\frac{m_\xi}{m_\eta}\frac{\partial u_\xi}{\partial\eta}\right)\right], \tag{2}$$

$$\frac{\partial hv_\eta}{\partial t}+\frac{\partial\left(hu_\xi v_\eta\right)}{m_\xi\partial\xi}+\frac{\partial\left(hv_\eta^2\right)}{m_\eta\partial n}+2\frac{hu_\xi v_\eta}{m_\xi m_\eta}\frac{\partial m_\eta}{\partial\xi}$$
$$+\left(v_\eta^2-u_\xi^2\right)\frac{h}{m_\xi}\frac{\partial m_\xi}{m_\eta\partial\eta}=$$
$$-gh\frac{\partial h}{m_\eta\partial\eta}-gh\frac{\partial z_b}{m_\eta\partial\eta}-ghn^2\frac{v_\eta\sqrt{u_\xi^2+v_\eta^2}}{h^{4/3}}$$
$$+\frac{1}{m_\xi m_\eta}\left[\frac{\partial}{\partial\xi}\left(h\upsilon_{ef}\frac{m_\eta}{m_\xi}\frac{\partial v_\eta}{\partial\xi}\right)+\frac{\partial}{\partial\eta}\left(h\upsilon_{ef}\frac{m_\xi}{m_\eta}\frac{\partial v_\eta}{\partial\eta}\right)\right], \tag{3}$$

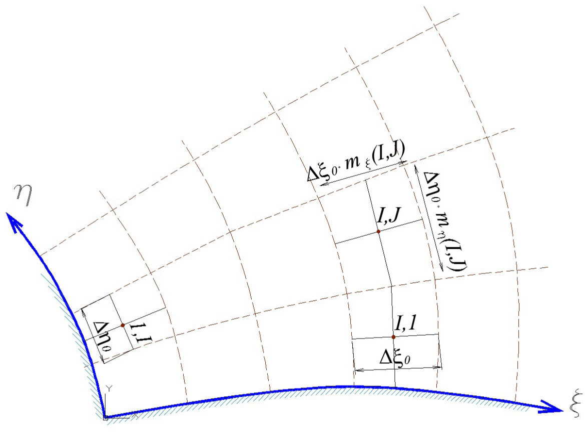

Fig. 1. *The meaning of Lamé's coefficients in the orthogonal curvilinear (natural) coordinate system*

The 2D mathematical model PCFLOW2D for simulating velocity and water depth fields, based on the Cartesian coordinate system, contains the basic differential equations governing the time-averaged flow, where the impact of Reynolds (turbulent) stresses is captured using the $k-\varepsilon$ turbulence model. Such an approach was used in developing the PCFLOW2D-ORTHOCURVE mathematical model, where the use of the $k-\varepsilon$ model was kept in the curvilinear coordinates. Therefore, the transport equations for turbulent kinetic energy per unit mass and the degree of its dissipation had to be converted to the natural coordinate system. The equation for turbulent kinetic energy per unit mass k is:

$$\frac{\partial hk}{\partial t}+\frac{\partial\left(hu_\xi k\right)}{m_\xi\partial\xi}+\frac{\partial\left(hv_\eta k\right)}{m_\eta\partial n}+\frac{hu_\xi k}{m_\xi m_\eta}\frac{\partial m_\eta}{\partial\xi}+\frac{hv_\eta k}{m_\xi m_\eta}\frac{\partial m_\xi}{\partial\eta}$$
$$=\frac{1}{m_\xi m_\eta}\left[\frac{\partial}{\partial\xi}\left(h\frac{\upsilon_{ef}}{\sigma_k}\frac{m_\eta}{m_\xi}\frac{\partial k}{\partial\xi}\right)+\frac{\partial}{\partial\eta}\left(h\frac{\upsilon_{ef}}{\sigma_k}\frac{m_\xi}{m_\eta}\frac{\partial k}{\partial\eta}\right)\right]$$
$$+hG-c_1h\varepsilon+hP_{kv}, \tag{4}$$

and the equation for its dissipation ε:

$$\frac{\partial h\varepsilon}{\partial t}+\frac{\partial\left(hu_\xi\varepsilon\right)}{m_\xi\partial\xi}+\frac{\partial\left(hv_\eta\varepsilon\right)}{m_\eta\partial n}+\frac{hu_\xi\varepsilon}{m_\xi m_\eta}\frac{\partial m_\eta}{\partial\xi}+\frac{hv_\eta\varepsilon}{m_\xi m_\eta}\frac{\partial m_\xi}{\partial\eta}$$
$$=\frac{1}{m_\xi m_\eta}\left[\frac{\partial}{\partial\xi}\left(h\frac{\upsilon_{ef}}{\sigma_\varepsilon}\frac{m_\eta}{m_\xi}\frac{\partial\varepsilon}{\partial\xi}\right)+\frac{\partial}{\partial\eta}\left(h\frac{\upsilon_{ef}}{\sigma_\varepsilon}\frac{m_\xi}{m_\eta}\frac{\partial\varepsilon}{\partial\eta}\right)\right]$$
$$+c_1\frac{\varepsilon}{k}hG-c_2\frac{\varepsilon^2}{k}h+hP_{\varepsilon v}. \tag{5}$$

The expression of G (the production of k due to horizontal velocity gradients of the basic flow) in orthogonal curvilinear coordinates is calculated using the following equation:

$$G = \upsilon_{ef} \left\{ \begin{array}{l} 2\left[\left(\dfrac{\partial u_\xi}{m_\xi \partial \xi} \right)^2 + \left(\dfrac{\partial v_\eta}{m_\eta \partial \eta} \right)^2 \right] \\ + \left(\dfrac{\partial u_\xi}{m_\eta \partial \eta} + \dfrac{\partial v_\eta}{m_\xi \partial \xi} \right)^2 \end{array} \right\}. \tag{6}$$

Effective viscosity value v_{ef} is derived using Eq. (7), **[7]** as the sum of coefficient of laminar and coefficient of turbulent viscosity:

$$v_t = c_\mu \frac{k^2}{\varepsilon}, \qquad v_{ef} = v + v_t. \tag{7}$$

The values for P_{kv} and $P_{\varepsilon v}$ are calculated using the following Eqs. (8) **[7]**, (9) and (11) **[7]**:

$$P_{kv} = c_k \frac{u_*^3}{h}, \qquad P_{\varepsilon v} = c_\varepsilon \frac{u_*^4}{h^2}, \tag{8}$$

$$u_* = \sqrt{c_f \left(u_\xi^2 + v_\eta^2 \right)}, \tag{9}$$

$$c_k = \frac{1}{\sqrt{c_f}}, \qquad c_\varepsilon = c_{\varepsilon r} c_2 \sqrt{c_\mu} \frac{1}{c_f^{3/4}}. \tag{10}$$

The value for the constant $c_{\varepsilon r}$ is 3.6 for the laboratory channels. In the Table 1 used values for the other empirical constants proposed by Launder and Spalding **[8]** are presented.

Table 1. Values of the constants in the $k-\varepsilon$ model

c_1	c_2	c_μ	σ_k	σ_ε
1.44	1.92	0.09	1.00	1.21

2 NUMERICAL METHOD

Finite volume numerical scheme proposed by **[9]** is used for solving partial differential equations presented in the previous section. Characteristics of the method are staggered control volumes and "hybrid" scheme. The "hybrid" scheme is a combination of the upwind and central difference scheme. The first order upwind scheme assures simplicity and robustness **[9]** and it remains stable even with very complex geometry, relatively coarse numerical grid and complicated boundary conditions. The use of a curvilinear numerical mesh also contributes to the stability of the method. For the depth corrections an iterative procedure is used. A fully implicit scheme is used for time integration providing stable and accurate solutions. Numerical method could be used to simulate subcritical and supercritical flows **[9]**.

3 FLOW IN THE CURVED SECTION

Free-surface flow in a curved section is much more complex than that in a straight section. One of its basic characteristics is the secondary flow phenomenon, which is generated as a result of the imbalance between the surface gradient in the transversal flow direction and the centrifugal force. The pressure gradient at the bottom in the direction towards the inner side of the bend dominates over the centrifugal force, generating the flow at the bottom towards the centre of the bend and the flow at the surface towards the outer bank. The transverse velocity component is a size class smaller than the longitudinal or primary velocity component. This results in additional energy losses. The energy loss depends on the relationship between the water depth and the radius of the curve. With smaller wall roughness, due to the impact of transverse circulation, energy losses can even exceed half the value of the total loss **[10]** and **[11]**.

For the cases of curved channels, where acting centrifugal forces cause the surface gradient to occur in the direction transversal to the flow, we can theoretically calculate the surface height difference between the outer and inner banks, Δh, using the following theoretically derived formula:

$$\Delta h = \frac{v^2}{g} \cdot \ln \frac{R_{out}}{R_{ins}}. \tag{11}$$

The equation refers to flows in curves where there are no energy losses due to friction along channel walls or changes in channel cross-section geometry in the transversal and longitudinal direction (e.g. narrowing, sills, or bed dredging).

For testing the 2D mathematical model based on the orthogonal curvilinear numerical mesh, a semi-circular smooth channel with a rectangular cross-section was used, which on both ends extended into long straight sections. This channel shape was chosen to remove the impact of boundary conditions on the flow in the curve; we obtained results that are conditioned only by the channel geometry and the appropriate discharge or flow velocity. A rectangular channel of a width of 20 m with a semi-circular curvature and a channel curvature radius of 30 m in the axis was used. The straight inflow section and the final section of the model are L = 100 m long and the channel bottom is horizontal. The channel geometry is shown in Fig. 2. Manning's roughness coefficient $n = 1\times10^{-6}$ s/m$^{1/3}$ was assumed for the channel bottom and banks.

The channel geometry in the mathematical model is described by 7104 points; 24 points in the direction transversal to the flow (ξ) and 296 points in the direction of the flow (η). In the straight section of the channel the mesh was uniform, with a distance of computation points 1 m × 1 m and in the curved section adjusted to the requirements of the orthogonal curvilinear mesh.

4 RESULTS AND DISCUSION

The hydraulic conditions were calculated for six discharges. The discharge rate varied from

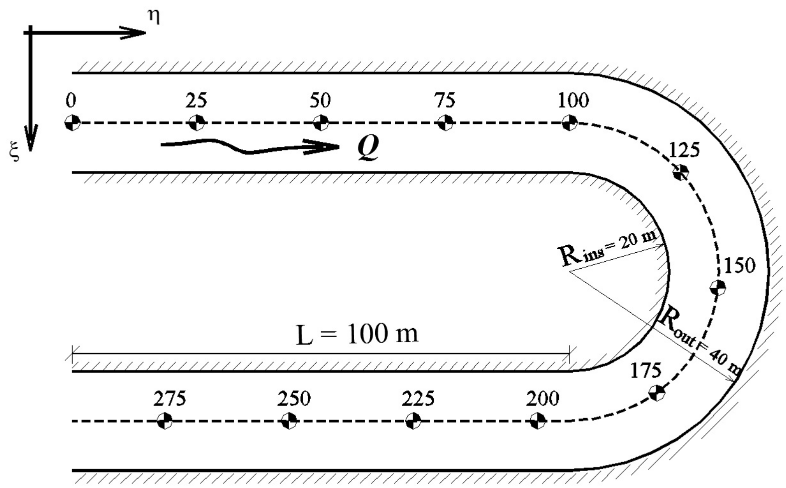

Fig. 2. *Sketch of the channel and the curve considered*

Table 2. *Comparison of mathematical model result and theoretical solution of transversal slope of water surface*

Q [m³/s]	h_{crit} [m]	h_{ups} [m]	h_{downs} [m]	v_{aver} [m/s]	Δh_{curv} (model) [m]	Δh_{curv} (theory) [m]
100	1.366	5.002	4.999	1.000	0.07	0.07
300	2.841	5.017	4.984	3.025	0.67	0.66
500	3.994	5.321	5.160	4.980	1.81	1.75
700	4.998	6.228	4.519	6.870	3.42	3.34
900	5.910	4.600	5.125	8.020	4.64	4.55
1100	6.756	5.200	5.805	8.675	5.52	5.32

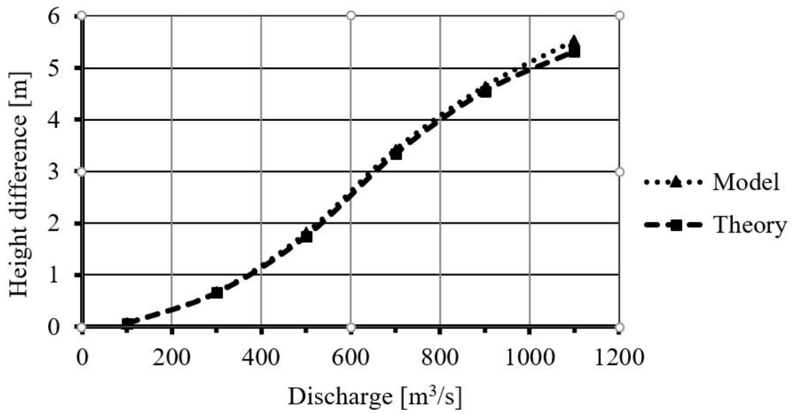

Fig. 3. *Height differences between the inner and outer edges of the curve from the mathematical model and theory*

Q = 100 m³/s to 1100 m³/s, with a step of 200 m³/s. For these discharges, with the average flow velocity in the curve ranging from approx. 1 m/s to approx. 9 m/s, the water level formation in the channel was calculated. In the cases investigated, flow with a horizontal surface and uniform velocity distribution was created at the upstream and downstream model boundaries. In the curved section, the water surface appropriately leaned towards the inner bank of the channel. Table 2 summarises the results of the calculated values: the flow rate (Q) for each case, calculated critical depth h_{crit}, water depth at the upstream section of the straight channel h_{ups}, water depth at the downstream section of the channel h_{downs}, average flow velocity in the curve v_{aver}, between channel stationing 100 and 194 m used to calculate the theoretical value of the transverse slope of the surface. The next two columns give the height differences between the inner and outer edges of the curve Δh_{curv}, derived from the mathematical modelling results and calculated theoretically using Eq. (9). Those values are presented graphically in Fig. 3.

Figs. 4 to 6 show the water surface formation at outer and inner edges of the channel for discharges 100 m³/s, 700 m³/s, and 1100 m³/s.

At Q = 100 m³/s and the average water depth in the channel of around 5 m (Fig. 4), flow velocity of approx. 1 m/s is created. The flow along the entire channel is in the subcritical regime and, because of the low flow velocity, the transverse slope of the free surface at the curve is low as well (Δh_{curv} = 7 cm). At both edges the surface has a falling trend in the flow direction. Under such conditions the average velocity along the channel does not change considerably; therefore, to calculate the water surface slope in the bend the velocity at any cross-section can be taken without causing any considerable differences between the theoretically calculated and the modelled free-surface slope in the bend.

The shape of the surface line at both edges is similar for the discharges up to 700 m³/s and follows

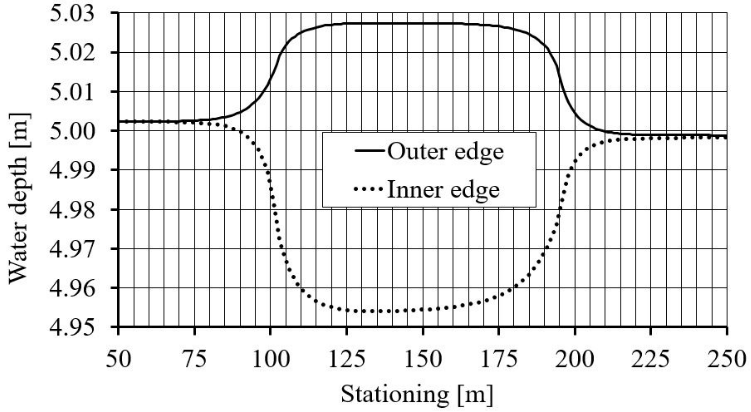

Fig. 4. *Water surface profile along channel walls at Q = 100 m³/s*

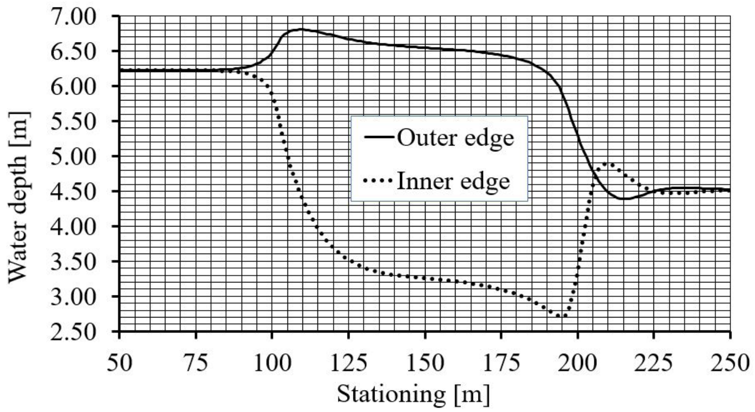

Fig. 5. *Water surface profile along channel walls at Q = 700 m³/s*

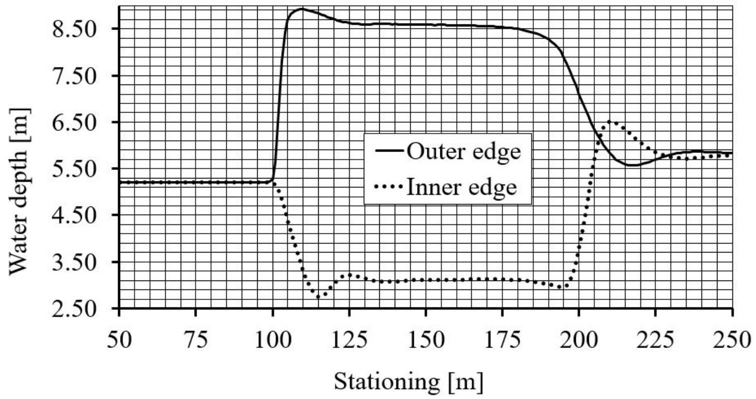

Fig. 6. *Water surface profile along channel walls at Q = 1100 m³/s*

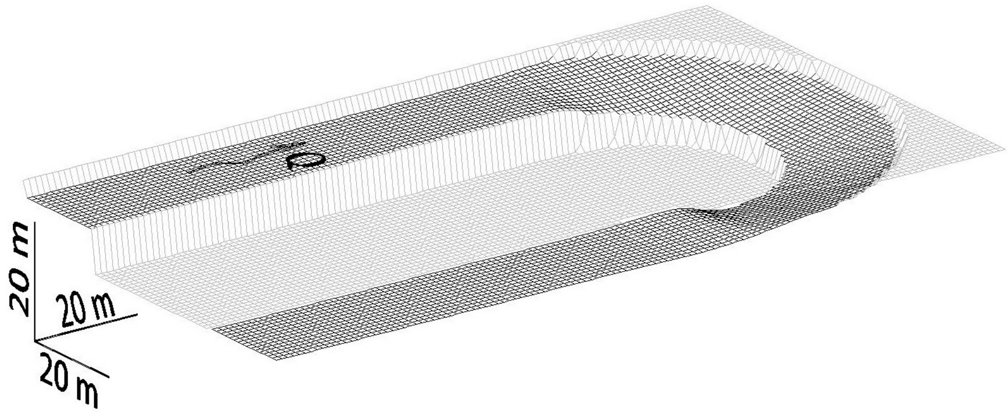

Fig. 7. *The axonometric view of surface in the curved channel at Q = 1100 m³/s*

the shape shown in Fig. 4 at discharge Q = 100 m^3/s. By comparing the offset of the water level at the channel edges and the mean depth it could be find that the lowering of the water level at the inner edge of the curve is much more pronounced than the water level rise at the outer edge.

The flow rate Q = 700 m^3/s is characteristic because in the downstream flow section, the flow regime changes into supercritical flow. The surface shape along the edges is of a somewhat different character than that with an unchanged regime (Figure 5). Because of inertia at increased velocity under the supercritical regime the surface at the end of the curve slightly fluctuates in the transversal direction. In the initial part of the curve the water surface resembles that in the subcritical regime, i.e. the water level rise at the outer edge is smaller than the water surface lowering at the inner edge. By the end of the curve this difference almost approaches zero, while the water surface rise is almost equal to the lowering at the mean water surface level in the straight part of the downstream section.

By increasing the discharge and velocity, the flow regime at the upstream boundary changes as well. At Q = 1100 m^3/s, supercritical flow conditions occur throughout the channel length. The calculation results are shown in Fig. 6. At the start of the curve the impact of flow inertia is evident, thus the surface slightly fluctuates. In the remaining part of the curve the surfaces at the edges are almost horizontal, with a considerable water surface superelevation compared to the mean depth at the outer edge and a water surface lowering by almost a half at the inner edge of the curve.

Under these conditions, surface fluctuations at the outflow from the curve occur, which is even more pronounced at high velocities. Because of energy losses, which are higher on examples with the higher velocities, and because of the supercritical flow conditions in the channel, the surface in the part of the channel following the curve is higher than that in the straight upstream section. Fig. 7 shows an axonometric illustration of the calculated water surface on the model of the curve at Q = 1100 m^3/s.

5 CONCLUSIONS

The analysis of the flow in a semi-circular curve using the 2D PCFLOW2D-ORTHOCURVE model, where the influence of channel walls was considered negligible, revealed the following:

- the form of the free-surface flow in the curved section depends on the flow regime (subcritical, transitional or supercritical);
- in subcritical flow conditions, the surface level rise at the outer edge is smaller by one half than the water level lowering at the inside edge;
- in supercritical flow conditions, the rise in the surface level at the outer edge is almost two times larger than the lowering of the surface level at the inner edge;
- at flow through a bend, where the regime transitions from subcritical to supercritical, the water surfaces at both curve boundaries are almost parallel and follow the linear change in the average depth;
- by taking into account the average water flow velocity across the curve, which is the result of the mathematical model, we obtained a very good fit between the theoretically calculated transverse slope of the free surface and the surface slope in the mathematical model.

6 NOMENCLATURE

ξ, η curvilinear system coordinates,
I, J succession numbers of numeric cel in the ξ and η directions,
m_ξ, m_η Lame's coefficients in the ξ and η directions
t time, [s]
h water depth, [m]
u_ξ velocity component in the ξ direction, [m/s]
v_η velocity component in the η direction, [m/s]
z_b bottom level, [m]
n Manning's friction coefficient, [s/m$^{1/3}$]
g acceleration due to gravity, [m/s^2]
ν laminar coefficient of viscosity, [m^2/s]
ν_t turbulent coefficient of viscosity, [m^2/s]
ν_{ef} effective coefficient of viscosity, [m^2/s]
k turbulent kinetic energy per unit mass, [m^2/s^2]
ε degree of k dissipation, [m^2/s^2]
P_{kv}, $P_{\varepsilon v}$ source terms due to the bottom friction for the k and ε respectively, [m^2/s^3]
c_f Chezy friction coefficient, [m$^{1/2}$/s]
v average flow velocity in the channel, [m/s]
R_{out} radii of the outer edge of the curved channel, [m]
R_{ins} radii of the inner edge of the curved channel, [m]

7 REFERENCES

[1] Roache, P.J. (1972). *Computational Fluid Dynamics*, Hermosa Publishers, Socorro.
[2] Četina, M. (1988). *Mathematical Modelling of Two-Dimensional Turbulent Flows*, MSc Thesis, University of Ljubljana, Faculty of Civil and Geodetic Engineering, Ljubljana. (in Slovene)
[3] Tang, X., Knight, D.W. (2015). The lateral distribution of depth-averaged velocity in a channel flow bend. *Journal of Hydro-environment Research*, vol. 9, no. 4, p. 532-541, **DOI:10.1016/j.jher.2014.11.004**.
[4] Gholam, A., Bonakdari, H., Zaji, A.F., Akhtari, A.A., Khodashenas, S.R. (2015). Predicting the velocity field in a 90° Open channel bend using a gene expression programming model. *Flow Measurement and Instrumentation*, vol. 46, part A, p. 189-192, **DOI:10.1016/j.flowmeasinst.2015.10.006**.
[5] Sui, B., Huang, S. (2017). Numerical analysis of flow separation zone in a confluent meander bend channel, *Journal of Hydrodynamics*, vol. 29, p. 716-723, **DOI: 10.1016/S1001-6058(16)60783-7**.
[6] Ivanović, D.M. (1963). *Vector analysis*, Scientific Book, Beograd. (in Serbian)
[7] Rodi, W. (1993). *Turbulence Models and Their Application in Hydraulics*, 3rd edition, A.A. Bakema, Rotterdam, Brookfield.
[8] Launder, B.E., Spalding, D.B. (1972). *Lectures in Mathematical Models of Turbulence*, Academic Press, London/New York.
[9] Patankar, S.V. (1980). *Numerical Heat Transfer and Fluid Flow*, McGraw-Hill Book Company, New York, **DOI:10.1201/9781482234213**.
[10] Bridge, J.S., Jarvis, J. (1976). Flow and sedimentary processes in the meandring river South Esk, Glen Clova, Scotland. *Earth Surface Processes*, vol. 1, no. 4, p. 303-336, **DOI:10.1002/esp.3290010402**.
[11] Bhowmik, N.G. (1979). *Hydraulics of Flow in the Kaskaskia River, Illionis, Report of Investigation 91*, Illionis State Water Survey, Urbana, Illionis.

Strojniški vestnik - Journal of Mechanical Engineering 64(2018)9, 543-554

DOI:10.5545/sv-jme.2017.4647
Original Scientific Paper
Received for review: 2017-06-02
Received revised form: 2017-09-21
Accepted for publication: 2017-10-13

Numerical Predictions of Cavitating Flow Around a Marine Propeller and Kaplan Turbine Runner with Calibrated Cavitation Models

Mitja Morgut[1,*] – Dragica Jošt[2] – Aljaž Škerlavaj[2] – Enrico Nobile[1] – Giorgio Contento[1]

[1] University of Trieste, Department of Engineering and Architecture, Italy
[2] Kolektor Turboinštitut, Slovenia

Cavitating phenomena, which may occur in many industrial systems, can be modelled using several approaches. In this study a homogeneous multiphase model, used in combination with three previously calibrated mass transfer models, is evaluated for the numerical prediction of cavitating flow around a marine propeller and a Kaplan turbine runner. The simulations are performed using a commercial computational fluid dynamics (CFD) solver and the turbulence effects are modelled using, alternatively, the Reynolds averaged Navier Stokes (RANS) and scale adaptive simulation (SAS) approaches. The numerical results are compared with available experimental data. In the case of the propeller the thrust coefficient and the sketches of cavitation patterns are considered. In the case of the turbine the efficiency and draft tube losses, along with the cavitation pattern sketches, are compared. From the overall results it seems that, for the considered systems, the three different mass transfer models can guarantee similar levels of accuracy for the performance prediction. For a very detailed investigation of the fluid field, slight differences in the predicted shapes of the cavitation patterns can be observed. In addition, in the case of the propeller, the SAS simulation seems to guarantee a more accurate resolution of the cavitating tip vortex flow, while for the turbine, SAS simulations can significantly improve the predictions of the draft tube turbulent flow.

Keywords: cavitation, marine propeller, Kaplan turbine, mass transfer models, RANS, SAS

Highlights
- *CFD simulations of cavitating flow around a marine propeller and Kaplan turbine runner.*
- *Homogeneous model used in combination with three previously calibrated mass transfer models.*
- *Turbulence modelled using RANS and SAS approaches.*
- *Calibrated mass transfer models guarantee similar levels of accuracy.*
- *SAS approach improves the local flow field resolution.*

0 INTRODUCTION

In modern market scenarios, the competitiveness of an enterprise is determined, not only by the quality of the product but also by its time to market. As a matter of fact, nowadays, computational fluid dynamics (CFD) technologies are routinely used for design purposes allowing, in general, more expensive and time consuming experimental tests to be performed only at the final stages of the project. Such an approach becomes particularly relevant for parametric and/or optimization studies, where several simulations can be performed in parallel.

In the specific case of marine propellers and hydraulic turbines, CFD analysis can be effectively used to predict the overall machine performances as well as to investigate the effect of specific flow phenomena such as cavitation for instance [1] to [6].

Cavitation is the phenomenon that consists of the formation and activity of cavities (or bubbles) inside a liquid medium [7]. In flowing liquids it appears in low pressure regions where pressure, also owing to the system geometry, decreases below a certain threshold value. In the case of marine propellers and hydraulic turbines it is, usually, an undesirable phenomenon because in most cases it implies negative effects such as losses, efficiency reduction, noise, erosion and vibration [8] to [12].

In the last decades several CFD approaches have been developed to numerically investigate cavitating flow phenomena. A valuable review of different approaches is for instance provided by [13] and [14] and references therein. Among all the approaches, the most widely applied today is probably the so-called homogeneous transport-equation based model. In this approach the multiphase flow is treated as a homogeneous mixture of liquid and vapour, with variable density, and the relative motion between phases is neglected. The evaluation of the variable density field is based on an equation for void ratio with the source terms modelling the mass transfer rate due to cavitation, generally known as mass transfer model. In the literature there are available several mass transfer models relying on tunable parameters [14] even though interesting solutions for overcoming

*Corr. Author's Address: University of Trieste, Department of Engineering and Architecture, via A. Valerio 10, 34127 Trieste, Italy, mmorgut@units.it

empiricism have for instance been proposed by [15] and [16].

In this study the homogenous transport- equation based model is considered and three different mass transfer models are employed. More precisely, the mass transfer models originally proposed by Zwart et al. [17], Singhal et al. [18] and Kunz et al. [19] with empirical coefficients calibrated according to [20] are employed.

The scope is to verify the applicability of the considered calibrated models to the numerical predictions of the cavitating flow around two different systems: marine propeller and Kaplan turbine.

The investigation is performed considering the Potsdam propeller test case (PPTC) model propeller working in uniform inflow [21], and a model Kaplan turbine experimentally investigated by researchers at Kolektor-Turboinstitut, Slovenia.

Even though the present study is carried out mainly to evaluate a possible more general character of the calibrated mass transfer models, related to the systems under consideration the influence of the turbulence modelling is also briefly evaluated. Thus, the simulations are performed using the standard Reynolds averaged Navier Stokes (RANS) approach and the more accurate and more time consuming Scale Adaptive Simulations (SAS). In the case of the steady state RANS simulations the workhorse Shear Stress Transport (SST) turbulence model [22] is used in combination with all the three different calibrated mass transfer models.

For the evaluation of the possible improvement related to a more accurate turbulence modelling approach, time dependent SAS simulations are carried out using the SST-SAS turbulence model [23] in combination with only a certain mass transfer model for convenience. The simulations are carried out using ANSYS-CFX (CFX for brevity) commercial CFD solver which is based on the node-centered finite volume method (more precisely on the Control Volume-Based Finite Element Method (CVFEM)) [24] and [25].

The numerical results are compared with the available experimental data. For a quantitative comparison the thrust is evaluated for the marine propeller, while the draft tube losses and the efficiency are considered for Kaplan turbine. For a qualitative comparison the sketches of cavitation patterns predicted around the blades are considered for both cases.

From this study it seems that for the prediction of the cavitating flow around a marine propeller and Kaplan turbine all the three different calibrated mass transfer models can be successfully employed. The machine performances can be predicted with a similar level of accuracy, even though small differences in the predicted cavitation patterns can be observed. As far as the turbulence modelling is concerned, the numerical results show that the SAS simulations could be used to improve the resolution of certain flow features such as the propeller cavitating tip vortex for example. Moreover, it seems that in the case of the Kaplan turbines, where the efficiency predictions are highly affected by the proper resolution of the unsteady draft tube turbulent structures, the SAS simulations could represent a good compromise between standard RANS simulations and the computationally more demanding and more accurate large eddy simulations (LES).

The paper is structured as follows. First the mathematical model is presented. Then, the numerical predictions performed for marine propeller and Kaplan turbine are described. The descriptions follow the same scheme where the considered system is presented, the numerical and meshing strategies are described, and the results are discussed. Finally, the concluding remarks are given.

1 MATHEMATICAL MODEL

Here, the homogeneous model is presented in the fixed frame of reference for convenience.

1.1 Governing Equations

In the homogeneous multiphase transport equation-based model, the cavitating flow can be described by the following set of governing equations:

$$\begin{cases} \nabla \cdot \mathbf{U} = \dot{m}\left(\dfrac{1}{\rho_l} - \dfrac{1}{\rho_v}\right) \\ \dfrac{\partial(\rho \mathbf{U})}{\partial t} + \nabla \cdot (\rho \mathbf{U}\mathbf{U}) = -\nabla P - \nabla \cdot \tau + S_M \\ \dfrac{\partial \gamma}{\partial t} + \nabla \cdot (\gamma \mathbf{U}) = \dfrac{\dot{m}}{\rho_l} \end{cases} . \quad (1)$$

Cavitating flow is modelled as a mixture of two species i.e. vapour and liquid behaving as one. The phases are considered incompressible. They share the same velocity **U** and pressure fields P.

The mixture density, ρ, and dynamic viscosity, μ, are scaled, respectively, as:

$$\rho = \gamma \rho_l + (1-\gamma)\rho_v, \qquad \mu = \gamma \mu_l + (1-\gamma)\mu_v. \quad (2)$$

The interface mass transfer rate due to cavitation, $\dot{m}$, can be modelled using three different calibrated mass transfer models.

1.2 Turbulence Modelling

In order to model turbulence effects different approaches can mainly be applied, depending on the required accuracy and the available computational resources. In this study we adopted the standard RANS approach in combination with the workhorse SST turbulence model, and the more advanced SST-SAS model available in CFX. For a detailed description of the considered models we refer to [22], [23] and [26]. Here, we clarify that the SST-SAS model is an improved unsteady-RANS formulation, with the ability to adapt the length scale to resolved turbulent structures by including the von Karman length-scale into the turbulence scale equation. The information given by the von Karman length scale allows SST-SAS model to dynamically adjust to resolved structures mimicking a LES-like behaviour in unsteady regions of the flow field. At the same time, the model provides standard RANS capabilities in stable flow regions.

1.3 Mass Transfer Models

The mass transfer models employed in this study were previously calibrated using an optimization strategy, where selected empirical coefficients of the considered models, were properly tuned for the prediction of the sheet cavity flow around a hydrofoil [20]. In the following the formulations of the considered mass transfer models are provided, and in Table 1 the calibrated empirical values namely F_e, F_c, C_e, C_c, C_{prod}, C_{dest}, are collected.

Zwart et al. model:

$$\dot{m} = \begin{cases} -F_e \dfrac{3r_{nuc}\left(1-\alpha\right)\rho_v}{R_B}\sqrt{\dfrac{2}{3}\dfrac{P_v-P}{\rho_l}} & \text{if } P < P_v \\ F_c \dfrac{3\alpha\rho_v}{R_B}\sqrt{\dfrac{2}{3}\dfrac{P-P_v}{\rho_l}} & \text{if } P > P_v \end{cases}. \quad (3)$$

Full cavitation model (FCM):

$$\dot{m} = \begin{cases} -C_e \dfrac{\sqrt{k}}{\kappa}\rho_l\rho_v\sqrt{\dfrac{2}{3}\dfrac{P_v-P}{\rho_l}}\left(1-f_v\right) & \text{if } P < P_v \\ C_c \dfrac{\sqrt{k}}{\kappa}\rho_l\rho_l\sqrt{\dfrac{2}{3}\dfrac{P-P_v}{\rho_l}}f_v & \text{if } P > P_v \end{cases}. \quad (4)$$

Kunz et al. model:

$$\dot{m} = \dot{m}^+ + \dot{m}^- : \begin{cases} \dot{m}^+ = \dfrac{C_{prod}\rho_v\gamma^2\left(1-\gamma\right)}{t_\infty} \\ \dot{m}^- = \dfrac{C_{dest}\rho_v\gamma\min\left[0, P-P_v\right]}{\left(0.5\rho_l U_\infty^2\right)t_\infty} \end{cases}. \quad (5)$$

Table 1. *Calibrated model coefficients*

Model	Evaporation	Condensation
Zwart	F_e = 300	F_c = 0.03
FCM	C_e = 0.40	C_c = 2.3×10^–4
Kunz	C_{dest} = 4100	C_{prod} = 455

It is worth clarifying that the Zwart et. al model is the native CFX mass transfer model while the FCM and Kunz et al. models were additionally implemented using the cell expression language (CEL) available in CFX. In the case of the FCM, following [27], f_v was replaced by α. In all simulations the mass transfer rate was considered positive if directed from vapour to liquid phase and the maximum density ratio ρ_l/ρ_v was clipped to 1000 for solver stability reasons.

2 MARINE MODEL SCALE PROPELLER

The numerical predictions for cavitating PPTC propeller working in uniform inflow are presented.

The considered propeller is a five-bladed, controllable pitch propeller having a diameter D=0.250 m. It was used as a blind test case at the 2011 Workshop on Cavitation and Propeller Performance. A significant amount of experimental data is currently available at [21].

2.1 Numerical Strategy

Due to the periodicity of the problem (uniform inflow and in this case neglected gravity) only one blade passage was modelled for computational convenience in all propeller simulations. Fig. 1 shows the shape of the computational domain. In Table 2 the values of the corresponding main dimensions are collected.

Since the propeller rotation was simulated using multiple reference frame (MRF) approach the computational domain was subdivided into two regions namely *rotating* and *fixed*. In Fixed the governing equations were solved by considering a *fixed* frame of reference, while in *rotating*, the governing equations were solved using a rotating frame of reference.

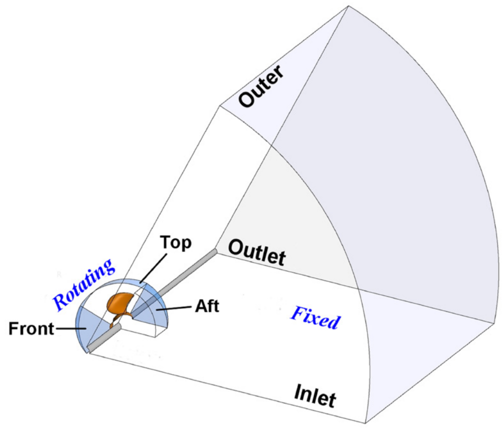

Fig. 1. *Shape of the computational domain; rotating region surrounded by front, aft and top interfaces*

The following boundary conditions were applied: on *inlet* boundary, the free-stream velocity components and a turbulence level of 1 % were set. The free-stream values (as well as the propeller rotational velocity) were set following the experimental setup [21]. The Reynolds number, Re_P, was in range (1.7 to 1.8)×10^6. On *outlet* boundary, a fixed value of the static pressure equal to 202,650 Pa was imposed. On the periodic boundaries (sides of the domain), the rotational periodicity was ensured. On solid surfaces the no-slip boundary condition was applied, and on *outer* boundary, the slip condition was set. Steady state RANS and unsteady SAS simulations were performed. In the case of the RANS simulations the workhorse SST turbulence model was used, while for SAS simulations the SST-SAS model was employed. Both models were used in combination with the automatic wall treatment available in CFX.

Table 2. *Distances of the boundaries/surfaces from the propeller mid plane in axial direction for inlet, outlet, aft, and from the propeller rotation axis in radial direction for outer and top*

Inlet	Outlet	Outer	Front	Aft	Top
2.30D	5.30D	5.00D	0.41D	0.31D	0.60D

As far as the discretization of the advective terms is concerned, for the RANS simulations, the *high resolution scheme* was employed while a bounded second order central difference scheme was used in the SAS simulations. For time discretization a first order implicit time scheme was used. It is worth clarifying that in this study with SAS an almost stable cavitating-tip vortex flow was investigated (see Fig. 4).

Thus, we assumed that, for this specific case, the more stable first order time scheme can be conveniently used and ensure a similar level of accuracy as the generally more unstable second order scheme.

Table 3. *PPTC propeller; thrust coefficient for RANS simulations with different mass transfer models*

J	σ_n	$K_{T,EXP}$	$K_{T,CFD}$		
			Zwart	FCM	Kunz
1.016	2.024	0.373	0.373	0.374	0.375
1.269	1.424	0.206	0.196	0.203	0.210
1.408	2.000	0.136	0.133	0.130	0.133

2.2 Meshing

The computational grids for *fixed* and *rotating* were generated independently and then joined in CFX through the General Grid Interfaces (GGI) solver capabilities. Both meshes were hexa-structured and were created using ANSYS ICEM CFD (ICEM for brevity).

The overall mesh had about 2.1×10^6 nodes with a proper refinement in the tip vortex region following [29].

The considered mesh arrangement proved to guarantee mesh independent results in former studies [30]. The average y^+ value on the blade surface was about 32. Fig. 2 shows the blade surface mesh.

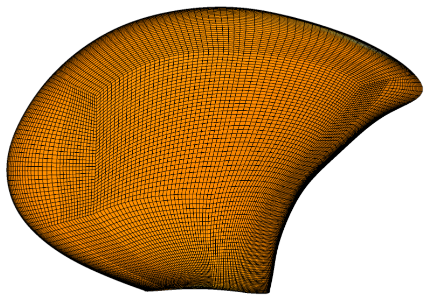

Fig. 2. *PPTC propeller, blade surface mesh*

2.3 Results

The simulations were carried out following the experimental setup suggested in [21]. The overall numerical predictions performed using the steady-state RANS approach compared well with the available experimental data.

Regarding the thrust (thrust coefficient) only minor differences were observed among the results obtained varying the mass transfer model. From Table

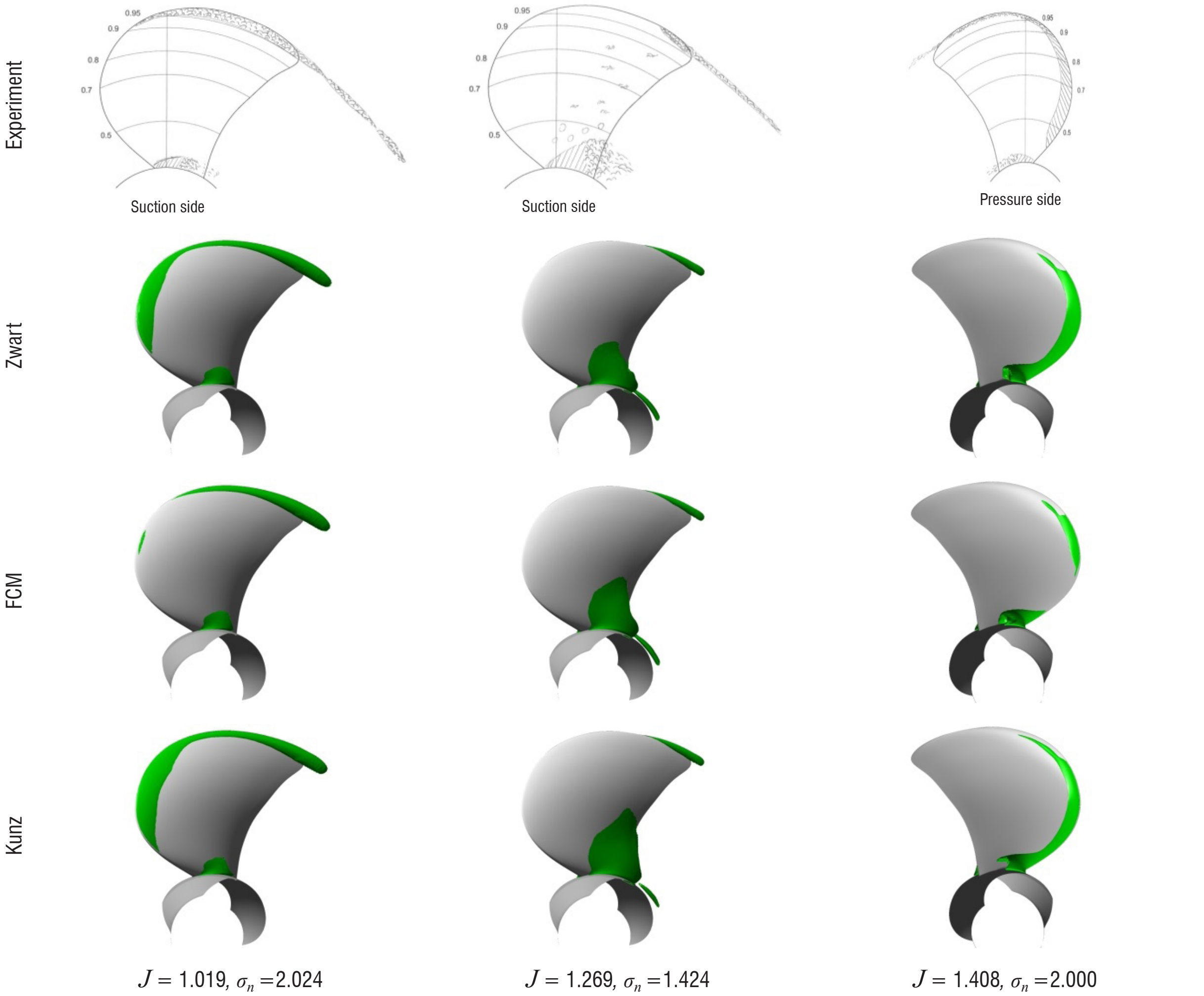

Fig. 3. *PPTC propeller; RANS simulation performed with three different mass transfer models; cavitation patterns depicted using isosurfaces of vapour volume fraction equal to 0.2*

3 it is possible to note that for a given operational condition the thrust predicted using the three different calibrated mass transfer models was in excellent agreement with the experimental data.

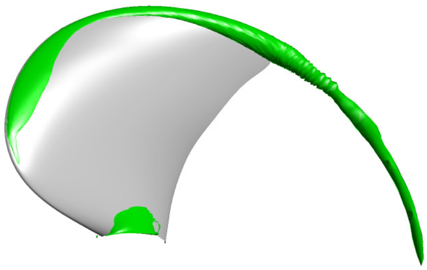

Fig. 4. Cavitation pattern predicted using the SST-SAS turbulence model in combination with the calibrated FCM mass transfer model for J = 1.019, σ_n =2.024

Following [21] the cavitation patterns are here presented as isosurfaces of vapour volume fraction equal to 0.2. From the qualitative comparison of the snapshots of the cavitation patterns, presented in Fig. 3 it is interesting to observe that for J = 1.019, σ_n = 2.024, only in the case of the FCM the shape of the cavitation pattern was correctly reproduced. With the other models a layer of sheet cavitation on the blade leading edge, not observed experimentally, was obtained. Conversely, for J = 1.408, σ_n = 2.000, the extent of the sheet cavity developing on the propeller face was better reproduced with the Zwart and Kunz models. The extent of the cavitation pattern predicted with the FCM was minor. The reasons behind these differences are still not fully clear. For J = 1.269, σ_n = 1.424 there were no differences in the cavitation patterns predicted using the three different mass transfer models.

Since in the case of the RANS simulations the tip-vortex was slightly under-estimated, in this study, focusing on J = 1.019, σ_n = 2.024, a brief evaluation of the SAS simulation was performed. An additional SAS simulation was performed in combination with the FCM model, even though the other two models could also be adopted for this purpose. The FCM was used, mainly, because in the former RANS simulation the most accurate prediction of the cavitation pattern, for the specific operational condition, was obtained using this mass transfer model. Fig. 4 shows that with the SAS simulation the extension of the cavitating tip-vortex was better reproduced. This improvement is related to the less diffusive character of the SAS simulations where, in general, lower levels of the turbulent viscosity are predicted than those obtained with the corresponding RANS simulations.

3 MODEL SCALE KAPLAN TURBINE

The numerical predictions of the cavitating flow in a model scale medium head Kaplan turbine are presented.

The turbine in question was developed by Kolektor-Turboinstitut and consists of a semi-spiral casing with two vertical piers, 11 stay vanes and a nose, 28 guide vanes, a 6-blade runner, and an elbow draft tube with two vertical piers. In CFD simulations a draft tube prolongation was added to improve solver stability as depicted in Fig. 5.

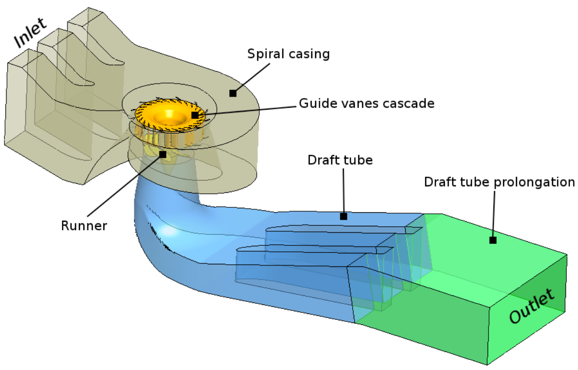

Fig. 5. *Sketch of the Kaplan turbine used in simulations*

The experimental tests were performed on the test rig at Kolektor-Turboinstitut following the IEC 60193 [31] international standard.

In this study the effect of the severity of the cavitating phenomena was analysed considering an operating point, close to the local best efficiency point, determined by a certain combination of guide vane blade opening angle and rotor blade angle. For such a point the flow and energy coefficients were φ/φ_{BEP} =1.33 and ψ/ψ_{BEP} = 0.86, respectively. The Reynolds number, Re_T, was 6×10^6.

3.1 Numerical Strategy

All the simulations were carried out considering the computational domain shown in Fig. 5.

Similarly to the propeller case, the numerical investigations were first performed using the steady state RANS approach, mainly to evaluate the effect of the calibrated mass transfer models on the accuracy of the numerical predictions. Then, further SAS simulations were carried out in order to improve efficiency predictions.

For RANS simulations the SST turbulence model was used while for SAS simulations the SST-SAS model was employed. Both were used in combination with the automatic wall treatment. Moreover, the curvature correction [32] and the Kato launder production limiter [33] were, here, included in all the simulations. For the discretization of the advective terms *high resolution* method was used for both RANS and SAS simulations. The use of the second order bounded central difference scheme (BCDS) in the current SAS simulations was precluded by poor solver stability. For time discretization a second order implicit time scheme was used.

For cavitation modelling all the three different mass transfer models were employed in RANS simulations while for SAS simulations the calibrated Zwart model was used exclusively.

It is important clarifying that during the design process of the current turbine, carried out by Kolektor-Turboinstitut, the standard Zwart model available in CFX was used. Therefore the SAS simulations were carried out in combination with the calibrated Zwart model in order to verify the benefits, in terms of accuracy, of using an advanced URANS model like SAS with the same (calibrated) mass transfer model [35].

The computational domain was properly subdivided in *rotating* region containing the runner and in *fixed* region including the rest of the turbine parts. In the case of the steady state RANS simulations the MRF approach was employed and at the interfaces between *rotating* and *fixed* regions the *frozen rotor* frame change/mixing model was used. In the case of SAS simulations the sliding grid approach (transient rotor stator) available in CFX was used.

All the simulations were carried out by imposing a given flow rate corresponding to a given flow rate coefficient. Thus, on *inlet* boundary a proper velocity distribution with a 5 % turbulence level was set. On solid surfaces the no-slip wall boundary condition was imposed.

Although, the effect of gravity for the model size is small, in this study, gravity was included in computations for the sake of completeness. Therefore, a value of static pressure prescribed at *outlet* boundary also included the hydrostatic pressure.

In current simulations the tip clearance was modelled while the hub clearance was neglected.

3.2 Meshing

The computational grid was composed of several turbine parts. It had about 8.3×10^6 nodes distributed as shown in Table 4.

Table 4. *Turbine mesh characteristics*

Turbine part	Nodes
Semi spiral casing with stay vanes	1,480,999
Guide vane cascade	2,755,496
Runner	1,858,374
Draft tube	1,786,432
Draft tube prolongation	398,056
Total	8,279,357

The meshes, for the different turbine parts, were generated independently of each other and subsequently joined in CFX using GGI. The meshes were created using ICEM and Turbogrid.

The grid in the spiral casing with stay vanes was unstructured, while the grids in the other turbine parts were structured. The average y^+ value on the different turbine parts was in the range of 3 to 9. The suitability of the considered mesh was verified in former studies [34]. Fig. 6 shows snapshots of surface meshes for the runner, draft tube and draft tube prolongation.

3.3 Results

In Fig. 7 the curves of efficiency and draft tube losses (head) are presented.

Considering the efficiency, it is interesting to note that similarly to the propeller case the simulations performed using different calibrated mass transfer models guaranteed similar results. As a matter of fact, from a qualitative comparison presented in Fig. 8 it is possible to note that the cavitation patterns obtained with different calibrated models were very similar to

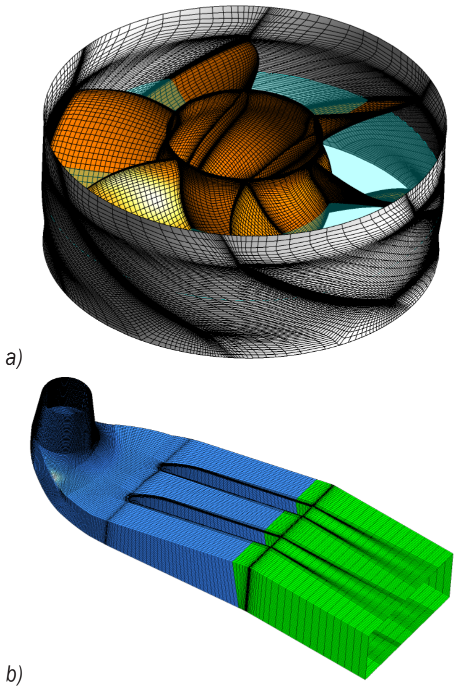

Fig. 6. *Surface meshes; a) runner, and b) draft tube and draft tube prolongation*

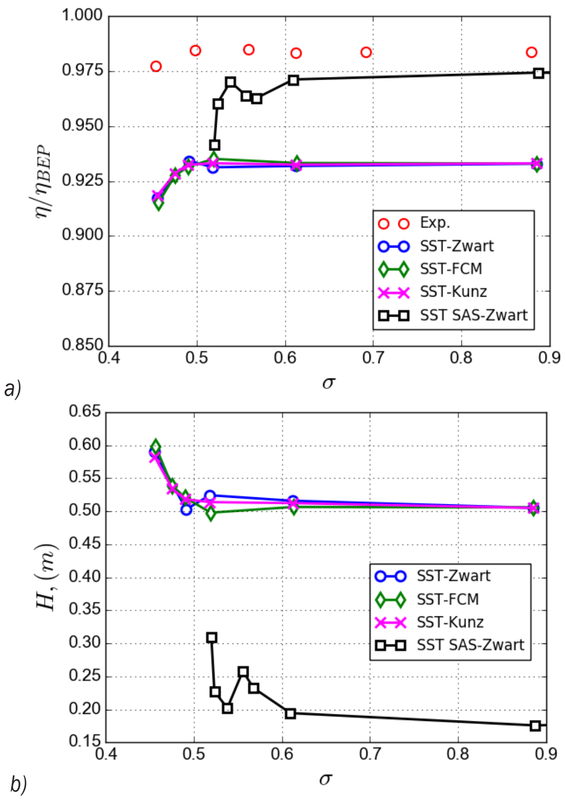

Fig. 7. *a) Efficiency and b) draft tube losses, predicted using steady state simulations (SST turbulence model) and time dependent simulations (SST-SAS turbulence model) in combination with different calibrated mass transfer models*

each other. The cavitation patterns are represented using the isosurfaces of the vapour volume fraction equal to 0.1 in order to clearly visualize the small (initial) cavitation bubbles predicted at .

Nevertheless, in the case of standard RANS simulations the efficiency was under-predicted, even though the shape of the predicted sigma brake curve compared well with the experimental trend. It is worth noting that the differences in predicted efficiency values were, mainly, due to the over estimation of the draft tube losses related to the steady state approach and turbulence modelling rather than on cavitation modelling [35].

Thus, in order to better resolve the vortex structures in the draft tube and consequently improve the accuracy of the efficiency predictions, additional SAS simulations were performed in combination with the calibrated Zwart mass transfer model.

Following [35] a comparison between the turbulent flow structures predicted by RANS and SAS simulations are presented in Fig. 10.

It is possible to note that for the steady state RANS simulations, only large turbulent structures were obtained.

In the case of SAS simulations, as expected, smaller turbulent structures were resolved leading to more accurate predictions of the draft tube losses.

In Fig. 10 it is also interesting to note the lower level of the viscosity ratio (ratio between the turbulent

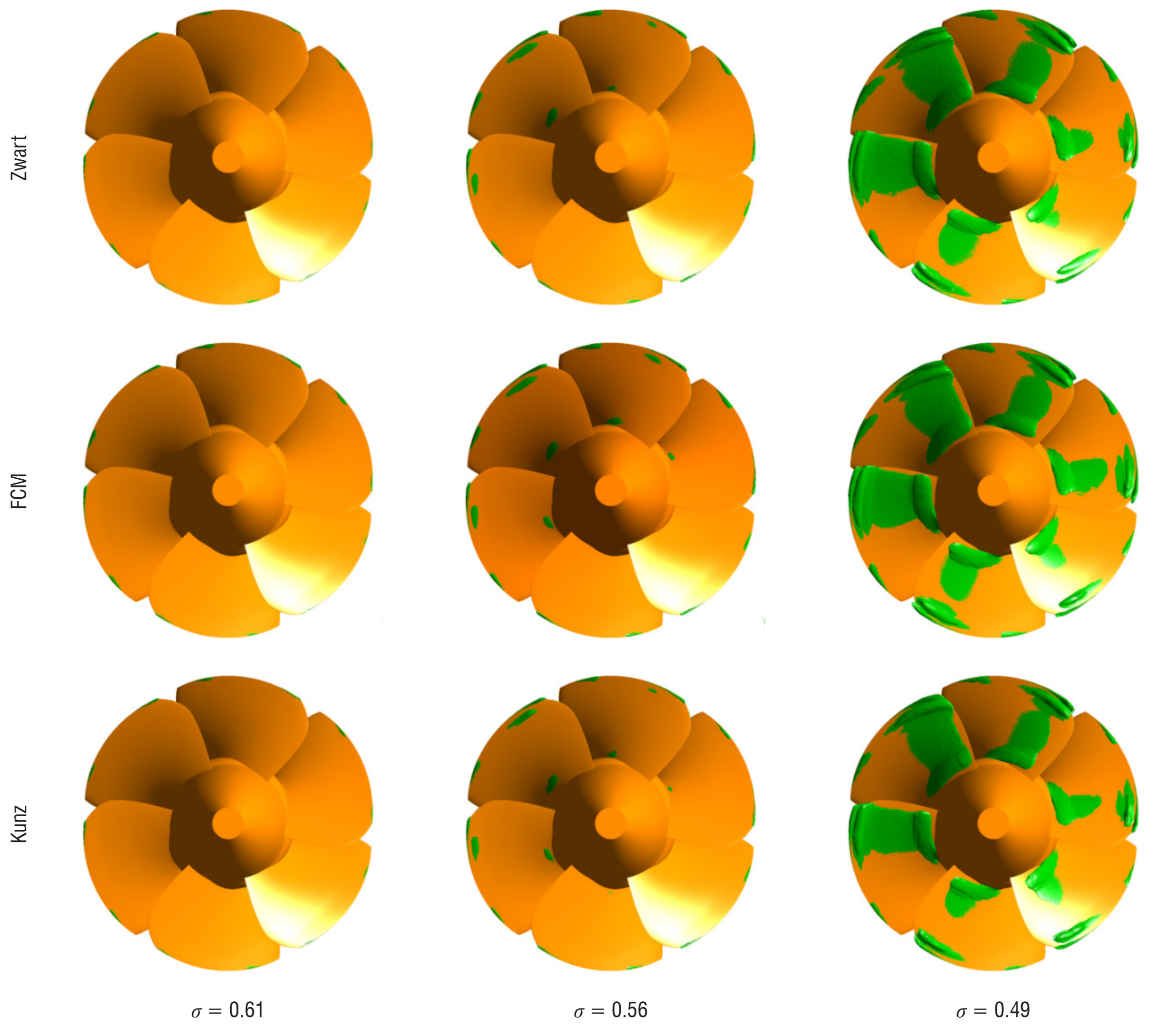

Fig. 8. *Kaplan turbine; steady state simulations performed using the SST turbulence model in combination with three different calibrated mass transfer models; cavitation patterns depicted as isosurfaces of the vapour volume fraction equal to 0.1.*

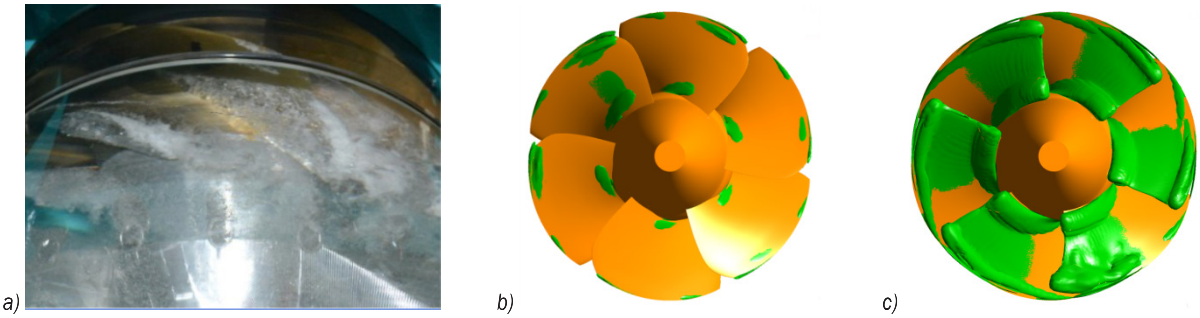

Fig. 9. *Cavitation patterns for σ = 0.52; a) experimental recording, b) predicted using Zwart mass transfer model in combination with the SST turbulence model, c) predicted using Zwart mass transfer model in combination with the SST-SAS turbulence model. Numerical cavitation patterns depicted as isosurfaces of vapour volume fraction equal to 0.1.*

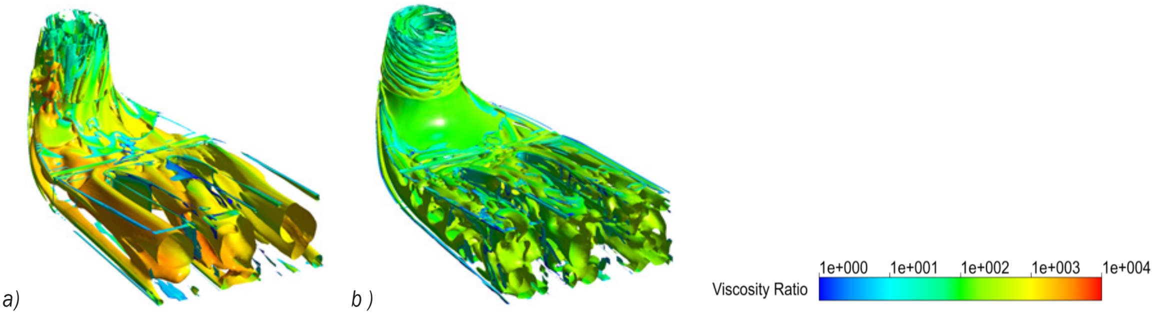

Fig. 10. *Turbulent structures represented using the isosurfaces of velocity invariant equal to 0.1, coloured by viscosity ratio; a) simulation performed with the SST turbulence model, and b) with the SST-SAS model*

and dynamic viscosity) associated with the SAS simulation.

Regarding the efficiency, from Fig. 7, it is possible to note that with the SAS simulations the predicted values compared well with the experimental data even though a premature break down of the turbine performances was predicted.

In Fig. 9 the cavitation patterns obtained with RANS and SAS simulations are qualitatively compared with the available experimental recording for σ = 0.52. It is possible to note that in the case of the steady state RANS simulation the extension of the cavitation phenomenon was under-predicted. This is related to the over prediction of the draft tube losses which lead to an inaccurate pressure distribution in the turbine. Actually, in the case of the steady state RANS simulations for a given cavitation number the pressure in the runner region was higher compared to the experimental one and consequently the predicted cavitation phenomenon was less severe.

Finally, it is worth clarifying that steady-state simulations did not predict the same extent of cavitation on all blades due to the *frozen rotor* conditions, imposed at Guide Vanes-Runner and Runner-Draft tube interfaces, which somehow preserved differences in circumferential direction. With transient simulations, as expected, the same amount of vapour structures was obtained on all runner blades.

4 CONCLUSIONS

In this study a homogeneous multiphase model, used in combination with three previously calibrated mass transfer models, was evaluated for the numerical prediction of the cavitating flow around a marine propeller and Kaplan turbine runner.

The simulations were carried out considering two different levels of turbulence modelling: the industrial workhorse steady state RANS approach and the more advanced unsteady SAS approach. In both the cases the governing equations were solved using ANSYS-CFX 15 commercial CFD solver.

The numerical results were compared with the available experimental data.

For the propeller, the thrust obtained with the RANS simulations, performed along with the three different mass transfer models, compared well with the available experimental data even though the experimental cavitation patterns were not perfectly matched. Except for a particular flow condition the cavitation patterns associated with the different mass transfer models were very similar to each other. From an additional investigation performed using the SAS approach a better resolution of the cavitating tip-vortex flow was obtained.

Also for the Kaplan turbine the three different mass transfer models predicted similar shapes of the cavitation patterns in the case of the RANS simulations. Nevertheless, using the RANS approach, mainly due to the overestimation of the draft tube losses, the turbine efficiency was not properly predicted. Better prediction of the draft tube losses, as well as of the efficiency, was obtained using the SAS approach even though in this case a premature break down of the performance was obtained.

From the overall results it seems that the calibrated mass transfer models in question can be successfully applied to the numerical predictions of the cavitating flow around a marine propeller and Kaplan turbine. It seems that for the prediction of the machine's performance they can guarantee similar levels of accuracy even though differences in the predicted cavitation patterns can be observed.

Finally, from this study it emerges that for improving the accuracy of numerical predictions, SAS simulations could represent a good compromise between standard RANS simulations and the computationally more demanding and more accurate large eddy simulations (LES).

5 ACKNOWLEDGEMENTS

The research leading to these results received funding from the People Programme (Marie Curie Actions) of the European Union's Seventh Framework Programme FP7/2007-2013/ under REA grant agreement n°612279. From the Slovenian Research Agency ARRS - Contract No. 1000-15-0263.

6 NOMENCLATURE

C_e	empirical coefficient (FCM model),
C_c	empirical coefficient (FCM model),
C_{dest}	empirical coefficient (Kunz model),
C_{prod}	empirical coefficient (Kunz model),
F_e	empirical coefficient (Zwart model),
F_c	empirical coefficient (Zwart model),
D	propeller, turbine runner diameter, [m]
E	hydraulic energy, [m²/s²]
H	turbine head, [m]
J	propeller advance coefficient,
K_T	propeller thrust coefficient,
L	characteristic length scale, [m]
M	turbine torque, [Nm]
P	pressure, [Pa]
P_v	saturation vapour pressure, [Pa]
P_{outlet}	pressure on outlet boundary, [Pa]
Q	flow rate, [m³/s]
R_{nuc}	radius of a nucleation site, [m]
S_M	source term,
T	propeller thrust, [N]
$\mathbf{U}$	velocity, [m/s]
U_∞	free stream velocity, [m/s]
V_A	propeller advance velocity, [m/s]
$c_{0.7}$	chord length (at 0.7/(D/2)), [m]
f_v	vapour mass fraction,
g	gravity acceleration, [m/s²]
k	turbulence kinetic energy, [m²/s²]
$\dot{m}$	mass transfer rate, [kg/(m³s)]
$\dot{m}^+$	mass transfer rate, vapour to liquid, [kg/(m³s)]
$\dot{m}^-$	mass transfer rate, liquid to vapour, [kg/(m³s)]
n	rotational speed, [rps]
r_{nuc}	nucleation site volume fraction,
t_∞	mean flow time scale, [s]
ρ	mixture density, [kg/m³]
ρ_l, ρ_v	liquid density, vapour density, [kg/m³]
η	turbine efficiency,
φ	turbine flow coefficients,
φ_{BEP}	turbine flow coefficients at local best efficiency point,
α	vapour volume fraction,
γ	liquid volume fraction,
κ	surface tension, [N/m]
μ	mixture dynamic viscosity, [Pa s]
μ_l	liquid dynamic viscosity, [Pa s]
μ_v	vapour dynamic viscosity, [Pa s]
σ	turbine cavitation number,
σ_n	propeller cavitation number,
$\boldsymbol{\tau}$	stress tensor, [N/m²]
ω	turbulence frequency, [1/s]
ψ	turbine energy coefficient
ψ_{BEP}	turbine energy coefficient at local best efficiency point
$NPSE$	net positive suction energy, [m²/s²]

7 REFERENCES

[1] Keck, H., Sick, M. (2008). Thirty years of numerical flow simulation in hydraulic turbomachines. *Acta Mechanica*, vol. 201, no. 1-4, p. 211-229, **DOI:10.1007/s00707-008-0060-4**.

[2] Stern, F., Wang, Z., Yang, J., Sadat-Hosseini, H., Mousaviraad, M., Bhushan, S., Diez, M., Yoon, S.-H., Wu, P.-C., Yeon, S.M., Dogan, T., Kim, D.-H., Volpi, S., Conger, M., Michael, T., Xing, T., Thodal, R.S., Grenestedt, J.L. (2015). Recent progress in CFD for naval architecture and ocean engineering. *Journal of Hydrodynamics*, *Ser. B*, vol. 27, no. 1, p. 1-23, **DOI:10.1016/S1001-6058(15)60452-8**.

[3] Luo, X., Ji, B., Tsujimoto, Y. (2016). A review of cavitation in hydraulic machinery. *Journal of Hydrodynamics, Ser. B*, vol. 28, no. 3, p. 335-358, **DOI:10.1016/S1001-6058(16)60638-8**.

[4] Štefan, D., Rudolf, P., Muntean, S., Susan-Resiga, R. (2017). Proper orthogonal decomposition of self-induced instabilities in decelerated swirling flows and their mitigation through axial water injection. *Journal of Fluids Engineering*, vol. 139, no. 8, p. 081101, **DOI:10.1115/1.4036244**.

[5] Ji, B., Luo, X., Wu, Y. (2014). Unsteady cavitation characteristics and alleviation of pressure fluctuations around marine propellers with different skew angles. *Journal of Mechanical Science and Technology*, vol. 28, no. 4, p. 1339-1348, **DOI:10.1007/s12206-013-1166-8**.

[6] Morgut, M., Nobile, E. (2012). Numerical predictions of cavitating flow around model scale propellers by CFD and advanced model calibration. *International Journal of Rotating Machinery*, vol. 2012, article id 618180, **DOI:10.1155/2012/618180**.

[7] Young, F.R. (1999). *Cavitation*. Imperial College Press, London, **DOI:10.1142/p172**.

[8] Rus, T., Dular, M., Širok, B., Hočevar, M., Kern, I. (2007). An investigation of the relationship between acoustic emission, vibration, noise, and cavitation structures on a Kaplan turbine. *Journal of Fluids Engineering*, vol. 129, no. 9, p. 1112-1122, **DOI:10.1115/1.2754313**.

[9] Jian, W., Petkovšek, M., Houlin, L., Širok, B., Dular, M. (2015). Combined numerical and experimental investigation of the cavitation erosion process. *Journal of Fluids Engineering*, vol. 137, no. 5, p. 051302, **DOI:10.1115/1.4029533**.

[10] Dular, M., Petkovšek, M. (2015). On the mechanisms of cavitation erosion – Coupling high speed videos to damage patterns. *Experimental Thermal and Fluid Science*, vol. 68, p. 359-370, **DOI:10.1016/j.expthermflusci.2015.06.001**.

[11] Wittekind, D., Schuster, M. (2016). Propeller cavitation noise and background noise in the sea. *Ocean Engineering*, vol. 120, p. 116-121, **DOI:10.1016/j.oceaneng.2015.12.060**.

[12] Carlton, J.S. (2012). *Marine Propellers and Propulsion (3rd Ed.)*. Butterworth-Heinemann, Oxford.

[13] Koop, A. H. (2008). *Numerical Simulation of Unsteady Tree-Dimensional Sheet Cavitation*. PhD thesis. University of Twente, Twente.

[14] Tran T.D., Nennemann, B., Vu, T.C., Guibald F. (2015). Investigation of cavitation models for steady and unsteady cavitating flow simulation. *International Journal of Fluid Machinery and Systems*, vol. 8, no. 4, p. 240-253, **DOI:10.5293/IJFMS.2015.8.4.240**.

[15] Senocak, I., Shyy, W. (2004). Interfacial dynamics-based modeling of turbulent cavitating flows, Part-1: Model development and steady-state computations. *International Journal of Numerical Methods in Fluids*, vol. 44, no. 9, p. 975-995, **DOI:10.1002/fld.692**.

[16] Asnaghi, A., Feymark, A., Bensow, R.E. (2017). Improvement of cavitation mass transfer modeling based on local flow properties. *International Journal of Multiphase Flow*, vol. 93, p. 142-157, **DOI:10.1016/j.ijmultiphaseflow.2017.04.005**.

[17] Zwart, P., Gerber, A.G., Belamri, T. (2004). *A two-phase model for predicting cavitation dynamics*. ICMF International Conference on Multiphase Flow, Yokohama.

[18] Singhal, A.K., Athavale, M.M., Li,H., Jiang, Y. (2002). Mathematical basis and validation of the full cavitation model. *Journal of Fluids Engineering*, vol. 124, no. 3, p. 617-624, **DOI:10.1115/1.1486223**.

[19] Kunz, R.F. , Boger, D.A., Stinebring, D.R., Chyczewski, T.S., Lindau, J.W., Gibeling, H. J., Venkateswaran, S., Govindan, T.R. (2000). A preconditioned Navier-Stokes method for two-phase flows with application to cavitation prediction. *Computers and Fluids*, vol. 29, no. 8, p. 849-875, **DOI:10.1016/S0045-7930(99)00039-0**.

[20] Morgut, M., Nobile, E. and Biluš, I. (2011). Comparison of mass transfer models for the numerical prediction of sheet cavitation around a hydrofoil. *International Journal of Multiphase Flow*, volume 37, no. 6, p. 620-626, **DOI:10.1016/j.ijmultiphaseflow.2011.03.005**.

[21] SVA Schiffbau-Versuchsanstalt Potstdam (2011). PPTC smp'11 Workshop, from *http://www.sva-potsdam.de/en/pptc-smp11-workshop*, accessed on 2017-03-02.

[22] Menter, F.R. (1994). Two-equation eddy-viscosity turbulence models for engineering applications. *AIAA Journal*, vol. 32, no 8, p. 1598-1605, **DOI:10.2514/3.12149**.

[23] Egorov, Y., Menter. F. (2007). Development and Application of SST-SAS Turbulence Model in the DESIDER Project. *Proceedings of the 2nd Symposium on Hybrid RANS-LES Methods*, Corfu.

[24] Schneider, G., Raw, M. (1987). Control volume finite-element method for heat transfer and fluid flow using collocated variables - 1. Computational procedure. *Numerical Heat Transfer*, vol. 11, no. 4, p. 363-390, **DOI:10.1080/10407788708913560**.

[25] Schneider, G., Raw, M. (1987). Control volume finite-element method for heat transfer and fluid flow using collocated variables - 2. Application and validation. *Numerical Heat Transfer*, vol. 11, no. 4, p. 391-400, **DOI:10.1080/10407788708913561**.

[26] ANSYS (2013). *CFX Solver Theory Guide*, Release 15.0, Canonsburg.

[27] Huuva, T. (2008). *Large Eddy Simulation of Cavitating and Non-Cavitating Flow*. Ph.D. Thesis, Chalmers University of Gothenburg, Gothenburg.

[28] Versteeg, H.K., Malalasekera, W. (2007). *An Introduction to Computational Fluid Dynamics: The Finite Volume Method, (2nd Ed.)*. Pearson Education Limited, London.

[29] Morgut, M., Nobile, E. (2012). Influence of grid type and turbulence model on the numerical prediction of flow around marine propellers working in uniform inflow. *Ocean Engineering*, vol. 42, p. 26-34, **DOI:10.1016/j.oceaneng.2012.01.012**.

[30] Morgut, M., and Nobile, E. (2011). Numerical predictions of the cavitating and non-cavitating flow around the model scale propeller PPTC. *Proceedings of Workshop on Cavitation and Propeller Performance, Second International Symposium on Marine Propulsors*, smp'11, Hamburg, Germany.

[31] IEC 60193 (1999). *Hydraulic Turbines, Storage Pumps and Pump-Turbine – Model Acceptance Tests*. International Electrotechnical Commission, Geneva.

[32] Smirnov, P.E., Menter, F.R. (2009). Sensitization of the SST turbulence model to rotation and curvature by applying the

Spalart-Shur correction term. *Journal of Turbomachinery*, vol. 131, no. 4, p. 041010, **DOI:10.1115/1.3070573**.

[33] Kato, M., Launder, B.E. (1993). The modelling of turbulent flow around stationary and vibrating square cylinders. *Proceedings of the Ninth Symposium on Turbulent Shear Flows*, p. 10.4.1-10.4.6.

[34] Jošt, D., Škerlavaj, A., Lipej, A. (2014). Improvement of efficiency prediction for a Kaplan turbine with advanced turbulence models. *Strojniški vestnik - Journal of Mechanical Engineering*, vol. 60, no. 2, p. 124-134, **DOI:10.5545/sv-jme.2013.1222**.

[35] Jošt, D., Morgut, M., Škerlavaj, A., Nobile, E. (2015). Cavitation prediction in a Kaplan turbine using standard and optimized model parameters. *Proceedings of 6th IAHR International Meeting of the Workgroup on Cavitation and Dynamic Problems in Hydraulic Machinery and Systems*, Ljubljana.

Strojniški vestnik - Journal of Mechanical Engineering 64(2018)9, 555-565

DOI:10.5545/sv-jme.2017.4619

Original Scientific Paper

Received for review: 2017-05-27
Received revised form: 2017-09-22
Accepted for publication: 2017-10-12

Construction of Water Surface Topography Using LIDAR Data

Gašper Rak[1,*] – Marko Hočevar[2] – Franci Steinman[1]
[1] University of Ljubljana, Faculty of Civil and Geodetic Engineering, Slovenia
[2] University of Ljubljana, Faculty of Mechanical Engineering, Slovenia

Measurements of water surface topography are important for hydraulic structures, operation of hydropower plants as well as in the determination of water surface profiles in rivers, especially in the event of high waters. We therefore investigated the conditions at a confluence of two supercritical flows, where distinctly three-dimensional flow conditions of standing waves form, as well as an unsteady structure of the water flow in transversal and longitudinal directions. Due to the fast water surface dynamics and the phenomenon of foamed or two-phase flow, the conventional measurement methods typically used in hydro engineering are not suitable for capturing complex water surface topography with high temporal and spatial resolution. Hence we wanted to verify the appropriateness of the laser scanning method for water surface topography measurements. This measurement method, which is considered less suitable or even useless for measurements of water body surfaces, was, coupled with an innovative approach, successfully used for water surface measurements of dynamic, turbulent, two-phase water flow. The acquisition of a point cloud with high temporal and spatial resolution allows for the construction of topography of intensive waving, which will also enable a topology analysis based on a phenomenological analysis of the relations between integral parameters of water flows and standing wave characteristics at the confluence.
Keywords: laser scanner, water surface, topography, two-phase flow, confluence

Highlights
- *Non-intrusive measurements of highly aerated, turbulent water flow was performed.*
- *Laser scanning enables acquisition of free-water surface profiles with high spatial and temporal resolution.*
- *The vertical fluctuations of non-stationary water surface were defined with post-processing of LIDAR data.*
- *The raw point cloud of laser scanning was used to construct water surface topography.*

0 INTRODUCTION

Measurements of free surface flows are important in a wide range of water engineering application in order to understand these flows and validate predictive tools we need to measure the free surface elevation accurately. It is also important for mechanical engineering, since water surface fluctuations affect the boundary conditions of mechanical equipment (e.g. at Hydropower plant (HHP)). Two hydraulic phenomena showing the significance of measuring free-water surface profiles are well illustrated in Fig. 1. In order to determine flow conditions, it is also necessary to measure such water surface dynamics as found during high flows below the hydropower plant (HPP) (Fig. 1a), as well as in different laboratory experiments, where turbulent, two-phase flow is present. Therefore, an experimental apparatus was set up at the hydraulic laboratory of the University of Ljubljana, Faculty of Civil and Geodetic Engineering, with high dynamics and diverse distribution of the water surface in a right-angled channel, which allowed us to test the applicability of laser scanning for aerated water surface measurements (Fig. 1b).

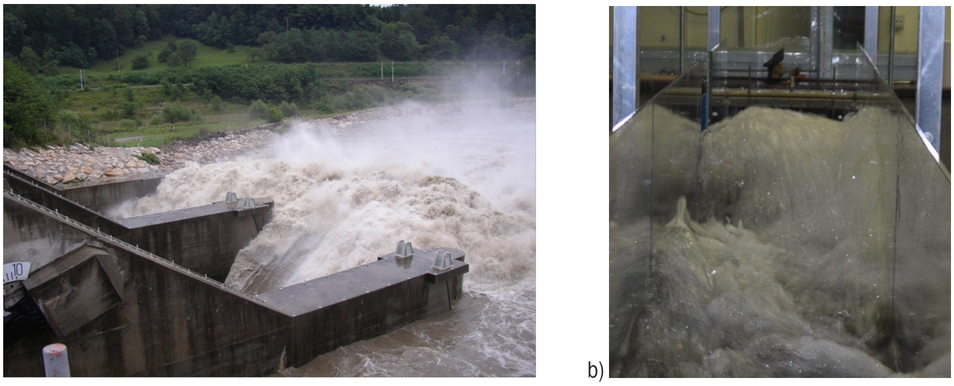

a) b)

Fig. 1. a) *The dynamic water surface below the Vrhovo HPP, and b) the experimental apparatus at the hydraulic laboratory, where distinctively standing waves are formed at the confluence of two incoming supercritical flows*

*Corr. Author's Address: University of Ljubljana, Faculty of Civil and Geodetic Engineering, Slovenia, gasper.rak@fgg.uni-lj.si

As an interesting practical case, a confluence of two flows was selected, where even with small velocities and with otherwise fairly calm water surface, vortexing and distinctively 3D flow conditions occur at the confluence. Insight into the situation at confluences has a wide applicability both for users and spatial planners, as confluences occur both on streams (natural and artificial river channels, torrents, etc.) as well as on many facilities and water infrastructure, such as fish passes, water treatment plants, surface water drainage from paved surfaces, etc. Knowledge of these phenomena is particularly important when designing the freeboard of longitudinal structures along the watercourse (e.g. bank fortifications along traffic routes) and transversal structures such as culverts and bridges that could be exposed to such waves.

1 WATER SURFACE TOPOGRAPHY AT THE CONFLUENCE

A marked change in flow conditions is caused by the confluence of two flows when, depending on the relationship between the magnitudes of the incoming flows, a more or less complex water surface topography. The conditions at confluences with incoming supercritical flow, with a high linear momentum, are even more complex, causing intensive transversal water mass dynamics. Similar to phenomena such as hydraulic jump, breaking waves etc., this is a distinctively three-dimensional water phenomenon, where a time-varying structure of the water flow forms in the transversal and longitudinal directions, which we are still unable to fully simulate using three-dimensional numerical models. 3D models are still not widely used in engineering work as they are too complex, while measured surface topographies allowing for calibration or verification of calculations are available only rarely. The acquired experimental data will be important for the development, calibration, and verification of 3D numerical models to obtain reliable results for the design and operation of hydraulic structures. In practice, particularly on torrential streams, this would help to prevent the under dimensioning of structures, thus no longer failing to take into account the accompanying processes deteriorating the functionality of hydraulic structures. Measurements are thus important, both in the field and in the laboratory, as they help us gain new insight into and knowledge of the phenomena and processes therein, while the applicability of measuring equipment can also be tested in the laboratory for more complex field conditions.

A detailed review of the literature shows that flow conditions at confluences are frequently studied, both experimentally and numerically; however, studies in subcritical flow regime prevail, i.e. where the water surface breaks into waves only slightly (e.g. [1] to [3]). Field measurements were also taken in subcritical flow conditions, which involved the triangulation of a reflector mounted on a small raft, which could only be done on a slightly undulating water surface at the confluence [4]. Few studies analysing flow conditions with supercritical flow across the confluence have been published (e.g. [5] and [6]), while the transversal changing of surface water formation and pulsations is studied the least. The main reason certainly lies in the unsuitability of conventional measurement methods, e.g. measurements of local pressures using piezometers, ultrasonic sensors, or point gauges. They measure flow parameters at a point, thus interfering with the water flow, or their performance is limited when two-phase flow occurs; thus, they do not allow for dynamic measurements with high spatial resolution. To successfully capture the dynamics of water surface topography, the measuring methods should allow for sampling using frequencies that are considerably higher than the changing rate of the water surface, it should have high spatial resolution, while the individual measuring equipment elements should not interfere with the flow and thus affect flow conditions. In our study we checked whether laser scanning could be used for these purposes. The measuring method used for a wide range of both professional and research fields to measure surfaces and/or terrain, was, until now, mostly considered as less suitable or successful in terms of measuring water body surfaces ([7] to [9]). Some studies show that laser scanning can be used to measure time-varying water surface formation ([10] to [13]), but only when particulate matter is already in water or it is added to improve reflectivity, which, however, reduces the usability in field measurements.

In analysing surface waves, along with average topography values, average values within very short time frames are important (i.e. pulsations), based on which the wave dynamics at a relevant travel length can be assessed. Our studies have shown that LIDAR can be used to measure water surfaces without the addition of particulate matter [14] in hydraulic phenomena that include turbulent two-phase and foamed flow, i.e. particularly in cases when other measuring methods provide less reliable, often unsuited results. In this study, the advantages of laser scanning were shown in the case of a very complex water surface topography formed at confluences with supercritical flow. A literature review shows that due to the limitations of conventional measuring methods this kind of topography measurements have not been taken so far.

2 EXPERIMENTAL APPARATUS AND MEASURING EQUIPMENT

The studies, which were divided into two parts, were carried out at hydraulic laboratory. First, we had to find the appropriate measuring equipment and define the settings of its parameters (having in mind that it would be used in field conditions as well) and verify the suitability of LIDAR technology for measuring water surfaces. An extensive verification process was conducted of both standing water and turbulent two-phase flow with high vertical water surface dynamics. Here, the verification procedure is not provided in detail as it relates to the measuring method, which is described elsewhere [14]. In the second part, systematic topography and surface pulsation measurements were taken at a right-angled confluence of two supercritical flows (hereinafter: T-junction, Fig. 2). The results of these extensive measurements were used to produce mesh models of water surface topography at T-junctions.

2.1 Experimental Setup of a T-Junction

The T-shaped junction, with a 90° angle between the axis of the main channel and its side inflow, has a 6-m long main channel and a 1-m long side channel. The experimental apparatus was entirely made of glass, which reduced the effect of walls on flow conditions as well allowed for a side view of the flow conditions. A horizontal bottom of all sections was provided to optimise the measurements and particularly to allow for appropriate inflows to the model, to minimise the number of joints at the confluence that might bring additional disturbances, and to reach the desired water flow velocities at the channels. The coordinate system of experimental set up has its origin of longitudinal axis at the beginning of the main channel, the origin of transverse axis at the middle point of the main channel, and of the vertical axis at the bottom of the channel (Fig. 2a).

To achieve a more distinct dynamic at the confluence, the conditions during supercritical flow were analysed when along with the flow structure a more complex water surface topography is developed in the form of standing waves, whose height significantly exceeds the average water surface levels of incoming flows or the flow downstream the confluence after calming of the waves (Fig. 2b).

Fig. 3 shows the water surface dynamics at the confluence, when the side inflow pushes away the main flow towards the opposite wall, which is followed by a downstream left/right fluctuation of the water mass until the transversal movement settles down. To gain insight into the standing wave formation it is necessary to measure wave peaks and their location as well as the magnitude of transversal fluctuation.

The dynamics at the confluence depend on the relationship between the energy and the linear momentum of both inflows. Given the selected events, the desired inflows in the inlets and at the confluence itself were provided with a controlled inflow to the model through two pressure vessels with adjustable height of the openings (Fig. 4a), and thus the height of the incoming water. The height of the apertures was adjustable to an accuracy of 0.01 mm. We can assume that due to the short distance between the outflow from the vessel and the start of mixing of the two flows at the confluence, and the small friction

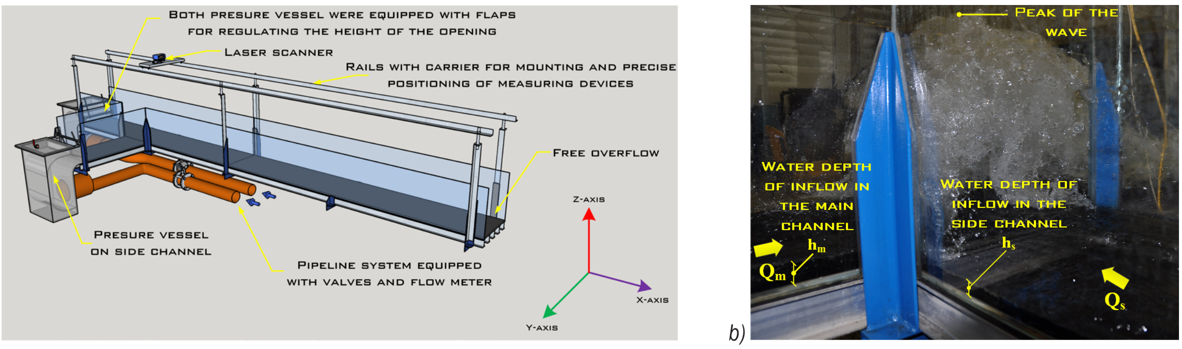

a) b)

Fig. 2. *a) A drawing of the right-angled confluence, and b) the photo of the waves at the confluence of supercritical flows exceeding the depth of the incoming flows by several times*

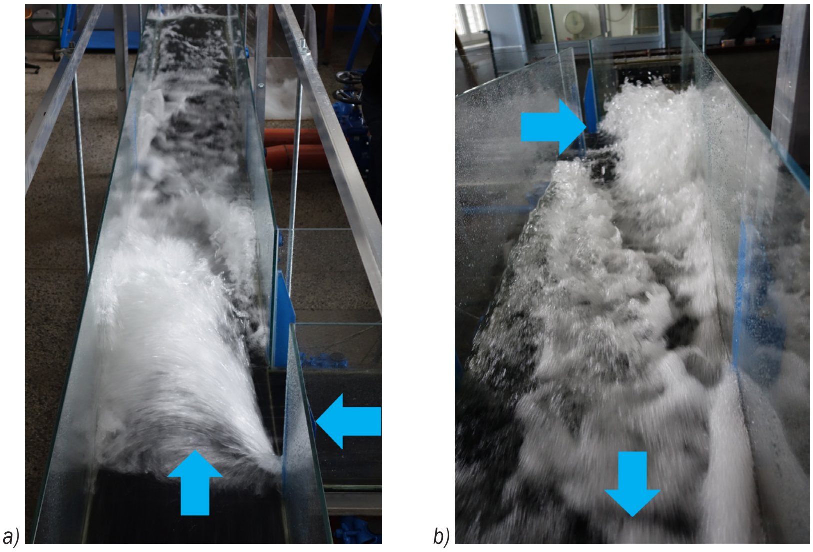

Fig. 3. *Photos of the apparatus show the dynamics of flow conditions at the confluence of two incoming flows; a)downstream view, and b) upstream view)*

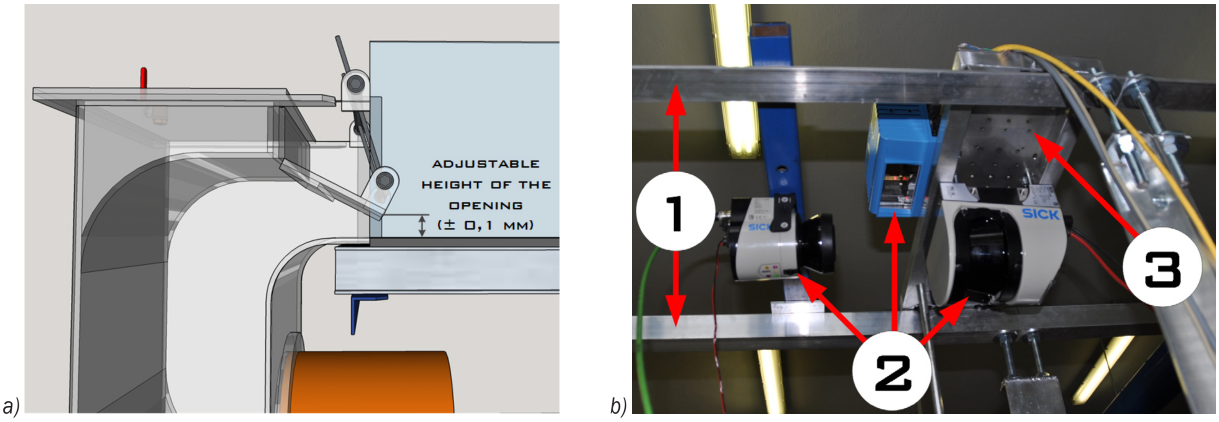

Fig. 4. *a) The pressure vessel with a flap for regulating the height of the inflows; b) the frame structure (1) with the measuring equipment (2) mounted on a special longitudinal carrier (3) whose structure allows for precise positioning in measured cross-sections*

at the glass walls the inflow height and depth were preserved in this section.

The experimental apparatus was equipped with a support provided by rails with a rail carrier for mounting measuring devices and a mechanism that allowed for repeatability of measurements in selected cross-sections with a precise location of the measuring equipment (Fig. 4b).

The frame structure for measuring equipment installation was separately attached to the model base, thus preventing the transmission of vibrations from the glass channel to the measuring equipment and the occurrence of additional pulsations and measurement uncertainty.

2.2 Measuring Equipment and Its Characteristics

LIDAR instrument LMS400 manufactured by SICK AG was used for water surface measurements. Based on the comparison of the measurements using different laser measuring systems this laser scanner proved to be the most suitable. Laser scanner operates in the visible red light wavelength λ = 650 nm (Fig. 5a). It is used for both indoor and industrial use with distances not exceeding 7 m. With this measuring range the measurement uncertainty is low also, i.e. ±3 mm with solid bodies. The instrument allows for a selection of the combination of scanning frequency 270 Hz to 500 Hz and an angular resolution from 0.1° to 1.0°. According to the manufacturer, the nominal accuracy of measurements can be achieved even at

a)

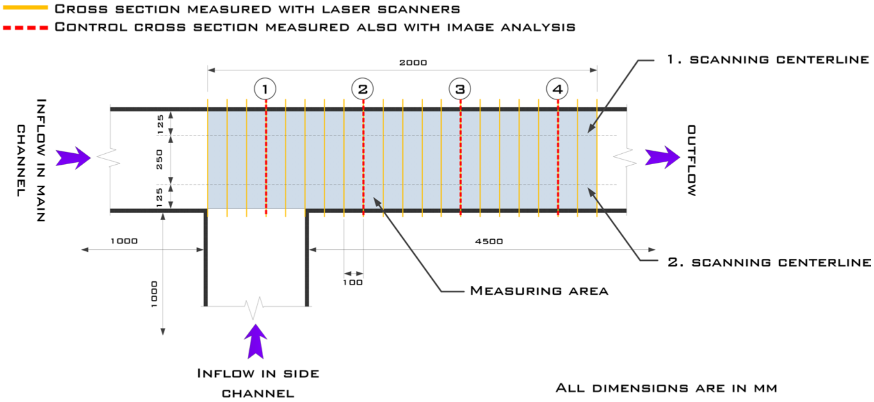

b)

Fig. 5. *a) Laser scanner SICK LMS400, and b) a scheme of the T-junction with its main dimensions, measured cross-sections, and the two longitudinal lines where simultaneous measurements in all cross-sections were taken*

290 Hz or at an angular resolution of 0.2° or at 500 Hz with an angular resolution of 0.4°. For an optimum number of the measured reflections in the individual recordings of cross-sections we used a frequency of 269.8 Hz and an angular resolution of 0.2°. To eliminate systematic errors or reduce their influence, test field measurements at a precisely known distance were taken before each set of measurements.

The longitudinal rails ensured that in all cases the bottom of the channel was at a distance of 1150 mm from the scanner. The range of depth fluctuations was between 0 mm and 450 mm so distances from 1150 mm to 700 mm were measured, while all measurements were taken inside the measuring range of the scanner; due to the response time of the device it was important that the measured surface was not located too close to the device.

Verification of the Lidar measurements using conventional instrumentation was not possible due to the highly complex and aerated nature of the free-water surface. Therefore, the verification of the laser measuring method in the dynamic water surface with two-phase flow was conducted by determining the reference values through analysing a sequence of images. Water level fluctuations were recorded using a high-speed camera, while a thin metal ruler was placed in the water to measure absolute values; the influence of the ruler under the given flow conditions could be assumed as negligible. The water surface was illuminated with a laser beam right at the ruler to later ease image processing, and particularly to improve resolution. A laser delivering 5 mW of output power and a operational wavelength 650 nm was used for illumination. Even though the directional light was used for illumination of the water surface at the ruler, bright strip was still thick around 1 cm (due to foamed water and bubbly flow). Casio EX-F1 high-speed camera was used which allows for up to 300 images per second, while a frequency of 60 images per second, with a resolution of 1920 × 1080 pixels, would suffice for water surface recordings. Video recordings of a length of 10 s were processed using our own algorithm for determining the mean value and fluctuations in Matlab. The verification measurements were conducted in 4 control sections. They are marked with red line and numbered with 1 to 4 on the Fig. 5. Verification of the method with image analysis was conducted with manual (visual) control of water levels determined with post-processing of video sequences.

To obtain the topography of standing waves at the confluence, measurements were taken in 20 cross-sections at intervals of 100 mm (Fig. 5b). For the individual scenarios of flow conditions a total of 40 cross-sections in two parallel longitudinal axes were recorded. At a higher incidence angle of the beams the number of received echoes is lower due to higher energy dissipation of the beams and specular reflections from the surface. The two scanning centerlines, as the 1st and 2nd centerlines in all measured cross-sections, are marked on Fig. 5b. This type of recording especially improved the quality of measurements along walls and in places where major changes in water surface topography occurred. In the case of a single centerline recording, such changes in topography could cause blind spots, failing to capture the entire cross-section.

At various inflow conditions, a total of 168 scenarios were recorded, where Froude numbers, which are used to express the intensity of supercritical flow, varied at both inflows between 2 and 12, while water depths varied between 10 mm and 30 mm. 3D models of topography for 5 scenarios are presented later in the paper. Raw data were recorded as a 2D point cloud in the polar coordinate system both when verifying the measuring method (which is not described here) and during systematic scanning of cross-sections along the confluence. A transverse profile of water surface for each measured cross-section was determined from the point cloud, which was composed of 6000 scans. The number of the measured values in the individual scans of the measured surfaces was a product of the angular range of measurements and the angular resolution. At an angular range 70° and an angular resolution of 0.2°, the number of outgoing signals is thus 350 per scan, i.e. a total of 2,100,000 points in the point cloud of a selected cross-section. Despite huge number of signals, emitted from laser scanner, only around 5 % of reflected beams are detected by the LIDAR scanner, and around 30 % of returned beams have remission values over threshold.

On the water surface of turbulent free-surface flows different types of two-phase air-water flow can occur (e.g. dispersed bubble flow, bubble flow, a foamed upper layer of water body and splashing of water droplets of different sizes). Because of that it is very difficult or even impossible to determine the water surface exactly. From that reason it is very important that a post-processing of LIDAR point cloud enables determination of the range of fluctuations. With filtering the measurements on the base of reflection intensity of the individual emitted signals, it is also possible to eliminate measurements, where returned beam was reflected from droplets and splashing.

2.3 Processing of the Raw Point Cloud of Measurements

In the first part of processing, the data on the measured distances were converted into the Cartesian coordinate system and point clouds from both positions of laser scanners were combined. Given the known channel geometry, the points representing the measurements outside the channel were excluded. By filtering the points based on the measured distances or calculated coordinates in the Cartesian coordinate system, the echoes received after several reflections from various surfaces were also excluded. In such a scenario, the laser scanner receiver receives the return signal, but due to the longer time of flight, the measured distance is too long, deviating from the calculated values of the coordinates within the area in question, i.e. the channel.

Along with the measured distances, reflection intensity for the individual emitted signals was also obtained, as based on the various intensities it was possible to exclude the measurements, i.e. signal returns from the drops above the water surface or from the bubbles deeper in the water body. Due to light scattering and energy dissipation along the path of the beam through water, these measurements revealed significantly lower remission values of signal returns. Such characteristics were analysed with the measurements of standing water, where, at various water depths, bubbles moving from the bottom to the surface were injected, thus determining the threshold that was later used in filtering laser measurement data **[14]**. The threshold was, subject to testing, set to a value that allowed for the exclusion of echoes from the bubbles deeper in the water and the smaller drops in the air, while still ensuring that most of the measured points were taken into account for calculating the water level's mean value **[14]**. The constant value of threshold was used for all measurements of water surface topography at the confluence.

Because that the returned beam was often not detected by the laser scanner or reflection intensity of returned beam was under threshold, data are randomly missing and consequently the data were non-uniformly sampled. Taking into account all successful measurements of each scan the water surface was determined with interpolation in uniformly increasing Y coordinates (transverse axis; increment of 5 mm). Set of data obtained was used for determination of water surface profile in a selected cross-section using median function. In the next step interpolation for 2D gridded data (predefined coordinates in X and Y direction between measured profiles; in both direction was used increment of 5 mm) was used to get data set to construct final 3D mesh models of water surface topography.

3 RESULTS

The measurement method verification, which first took place in a chamber with controlled conditions, showed that LIDAR can be only used to capture the formation of water surfaces where foamed or developed enough two-phase flow in the upper layer occurs. Due to the laser beam reflections from the water surface, successful measurements in standing, clean water were limited to an incidence angle of the beams at around 0°. In poorly developed two-phase flow with low bubble density and when bubbles occur across the entire depth of the water body, there are more reflections and a wider range of incidence angles. The assessed values are lower than the actual ones due to the reflections from the bubbles deeper in the water.

The influence of the bubbles deeper in the water was successfully reduced by filtering the point cloud and taking into account the intensity. In the foaming upper layer of standing water a measurement accuracy of ±3 mm was achieved, which corresponds to the nominal measurement uncertainty of the LIDAR device [14].

The verification of the measurement method at the T-junction apparatus, made e.g. in the scenario involving strong vertical water surface dynamics (surface fluctuation up to ±50 mm) and the two-phase flow phenomenon, showed that due to the dynamic nature of the phenomenon and the measured medium as well as the estimated measurement uncertainty of the reference method, by analysing the images taken using the high-speed camera, the measurement accuracy can be estimated at ±(5 to 10) mm. The case of the measured transversal formation of the water surface and the comparison with the reference values determined by analysing the images taken with the high-speed camera for cross-section 2 (Fig. 5b) is shown on Fig. 6 and in Table 1. The point cloud, presented on the Fig. 6, consist of 3000 scans with the laser scanner, measured from a single location (above the middle of the channel). In measurements using image analysis water surface fluctuations were also detected shown with a deviation interval from the mean value.

Fig. 6 shows that the water surface profile, determined by laser measurements and filtering based on remission values, agrees well with the measurements taken using the high-speed camera. Minor differences are shown in Table 1.

Based on the data processing shown and the small deviations in measurements in control cross-sections (Fig. 5), LMS400 was selected. All topography measurement depict the most dynamic part of the water surface along the confluence, as it gives the most important information for design, operation, etc. The mean values of the measured surfaces in consecutive cross-sections were used to construct the dynamic surface area, as a measured water surface topography of the area concerned, and presented from surfaces in the form of 3D mesh models (Fig. 7). Only

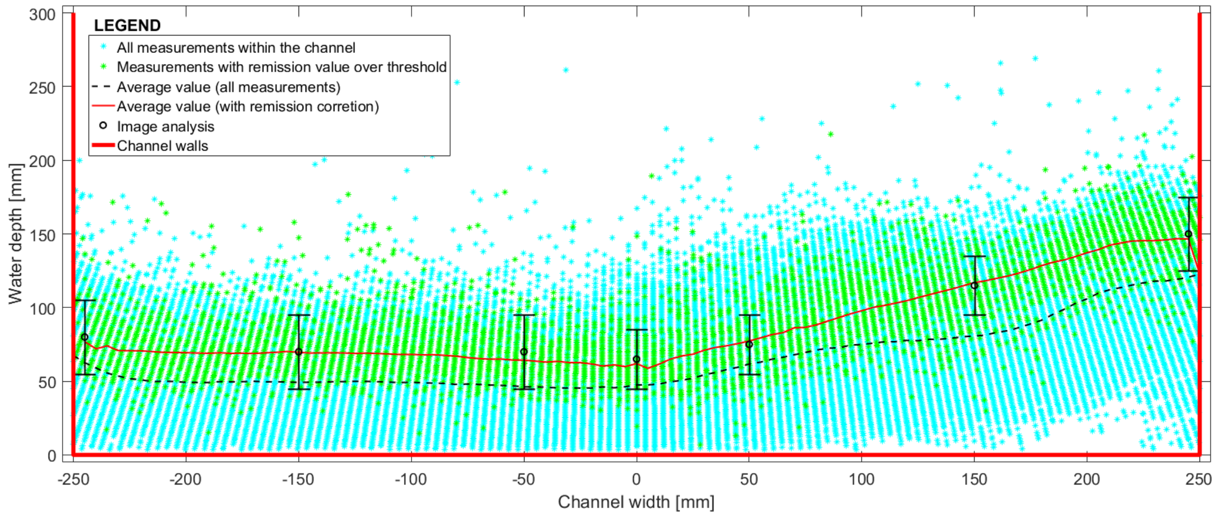

Fig. 6. *The entirety of the point cloud within the channel, deviation of the filtered data with remission values above a threshold, the water surface profile, and the reference values determined through analysis of the images recorded with a high-speed camera (control section 2 on Fig. 5; scenario $h_1 = h_2 = 20$ mm, $Fr_1 = 8.4$ and $Fr_2 = 6$)*

Table 1. *Comparison of water surface measurements in selected points at control cross-section 2 using the laser scanner and image analysis with a high-speed camera*

	Measured water depth values						
	point 1	point 2	point 3	point 4	point 5	point 6	point 7
Image analysis using a high-speed camera [mm]	80	70	70	65	75	115	150
LMS400 without filtering [mm]	63	50	46	48	62	81	121
LMS400 with filtering [mm]	77	70	65	62	77	117	147
Difference LMS400 and high-speed camera, in %	-3.7	0.0	-7.2	-4.7	+2.6	+1.7	-0.2

points with remission values over threshold were used to construct the topography models.

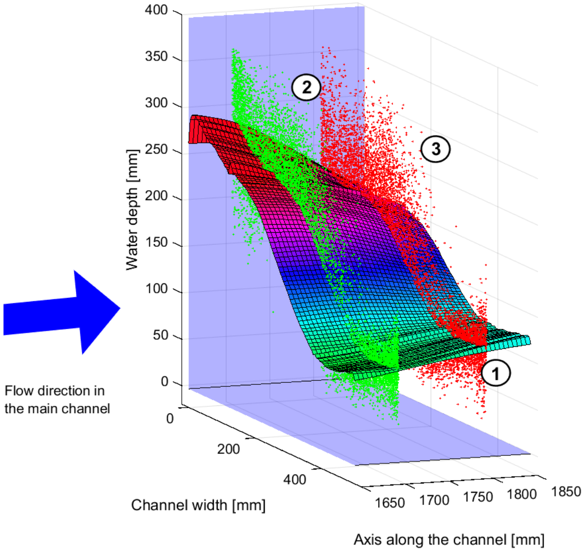

Fig. 7. *Point clouds of two consecutive cross-sections and a section of the standing wave mean free water surface, constructed with post-processing of the laser scanning measurements (scenario $h_1 = h_2 = 20$ mm, $Fr_1 = 8.4$ and $Fr_2 = 6$)*

The free water surface dynamics is shown in Fig. 7, which also shows vertical distributions of the measured reflections in two neighbouring cross-sections showing the range of fluctuations around a mesh model of the surface area structured based on calculated mean values of the water surface. The Fig. 7 showing fluctuations, as evident from the entire point cloud in the individual cross-sections, reveals that the highest water surface fluctuations occur along the channel walls (points 1 and 2) where side supercritical inflow causes a high transversal dynamic of the flow and at the very top of the standing wave ridge inside the channel (point 3).

The design of the 3D mesh model of the entire area concerned allows for illustration of a dynamic water surface topography at a confluence and thus further processing and analysis of standing wave formations (e.g. location and size of peaks) as a function of the input parameters of the inflows. The photo above (Fig. 8a) shows the 3D topography for the case of two incoming flows with the same depth in both branches (20 mm), but with different Froude numbers, i.e. $Fr = 8.5$ at the main channel and $Fr = 5.6$ at the side channel. As the laser imaging progressed from top down (i.e. plan view), the measured water surface cannot show air pockets or tunnels of air occurring in the body of the wave, below the cover ridge of the wave along the circulation zone of both inflows (Fig. 8b). As seen from the photo, with high velocities of both inflows a barrel-like water flow formation occurs, i.e. a barrel roll; the barrel's inside surfaces, of course, cannot be detected from the existing scanning axes. The number of successful measurements is also low where water is not or is hardly aerated (front-left part of the Fig. 8b). In this area there are no bubbles, but water surface is slightly waved due to the water spraying. In this area we got some successful measurements with reflection at perpendicular incident on the water surface. Density of points are smaller as well as the quality, but it was still possible to generate the 3D mesh model. Tests show that, given the momentum of incoming flows, a single barrel can be formed in the direction of the stronger flow, or a double barrel in the case of equal flows.

Fig. 9 shows 4 topography models for the scenarios with different flow characteristics. LIDAR measurements and the topography models constructed

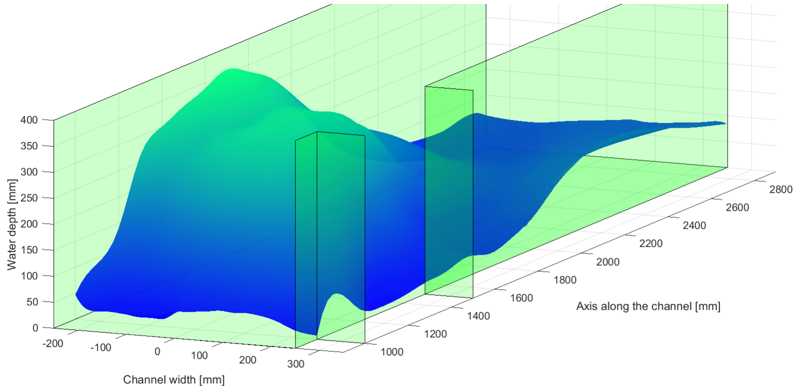

a)

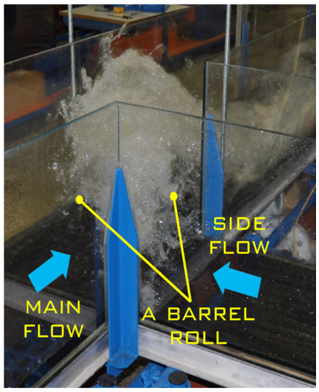

b)

Fig. 8. *a) A case of constructed water surface topography along the confluence, and b) a photo – both showing wave peaks along the wall and in the channel*

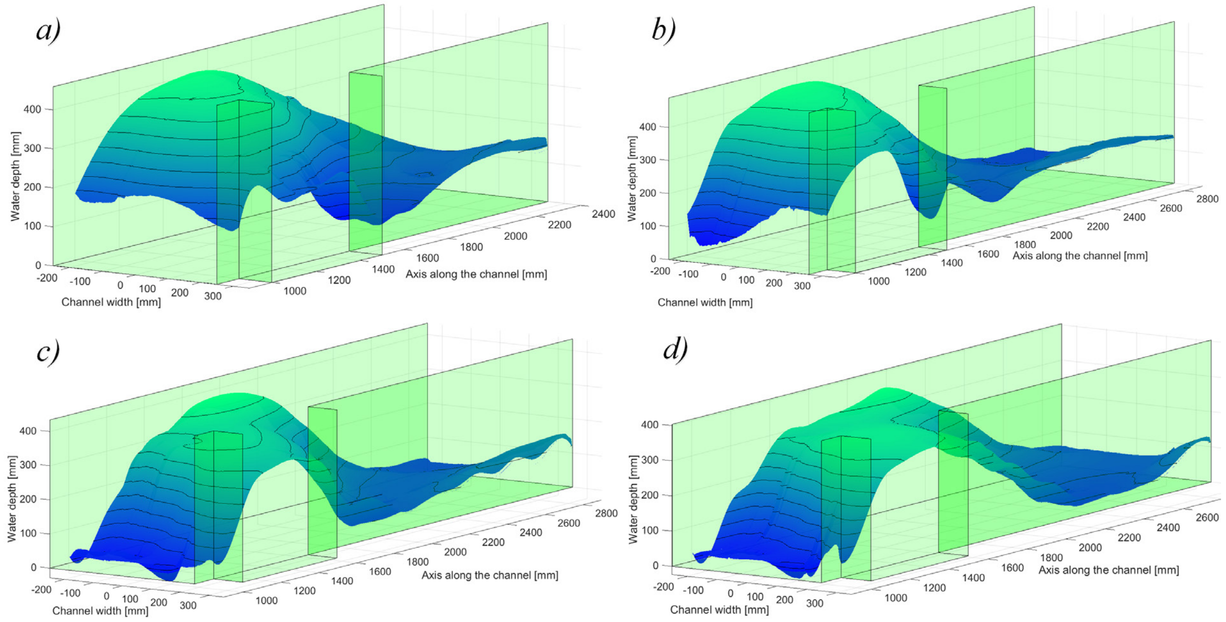

Fig. 9. *3D mesh models of water surface topography at the confluence for 4 scenarios with different flow geometry and hydraulic conditions: a) h_1 = h2 = 25 mm, Fr_1 = 7.92 and Fr_2 = 5.79; b) h_1 = 30 mm, h_2 = 20 mm, Fr_1 = 6.76 and Fr_2 = 7.04; c) h_1 = 30 mm, h_2 = 10 mm, Fr_1 = 5.99 and Fr_2 = 11.99; d) h_1 = 30 mm, h_2 = 10 mm, Fr_1 = 6.9 and Fr_2 = 11.05)*

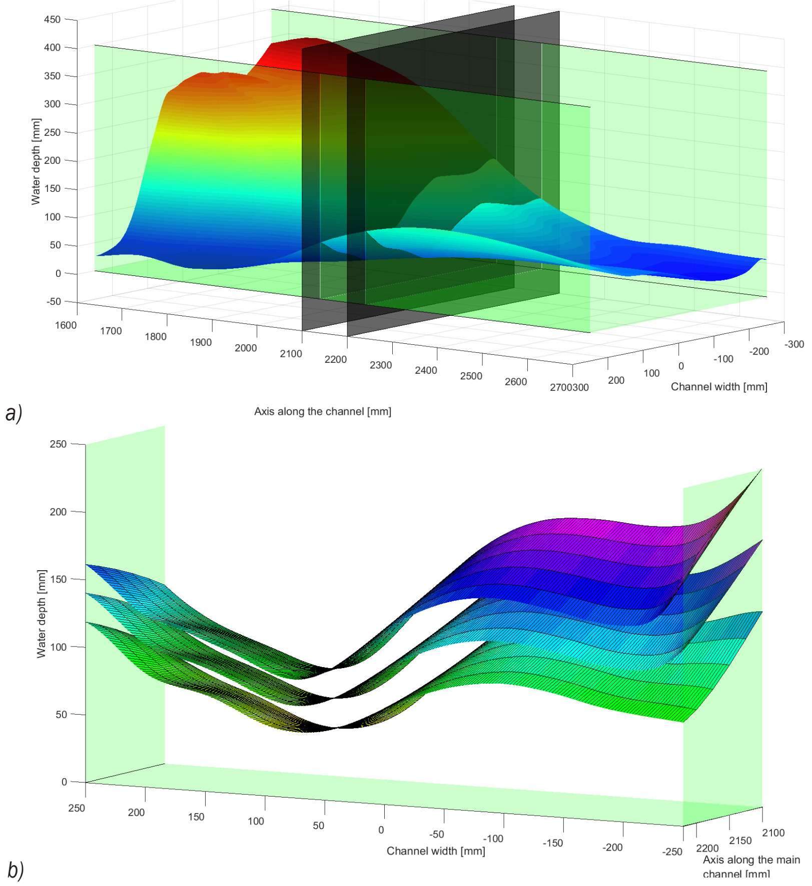

Fig. 10. *a) Location indication of a standing wave section in a length of 100 mm, and b) section of standing wave with a plot of the average free water surface and water surface envelopes by taking into account the measured fluctuations*

from them can be used to determine and visualize the structures of water flow, wave peaks and their location, points of water surface inflections, extend of standing waves etc.

Considering the (filtered) fluctuations in the individual cross-sections, it is also possible to determine the maximum and minimum water surface fluctuation envelope (e.g. without drops above the water surface). However, due to the lower number of successful measurements in the individual scans of the measured sections and particularly because the measurements were taken in the individual sections, a continuous, simultaneous illustration of temporal dynamics of water mass movement across the entire area is not possible. Nevertheless, based on the results of measuring permanent inflow from both channels we can analyse the extent to which water surface fluctuations occur also in critical locations. With knowledge of free-water surface fluctuations of these phenomena we can select appropriate solutions, when designing the hydraulic structures in practice. Fig. 10a shows a 100-mm long section (left), and Fig. 10b 3D mesh model of mean water surface as well as both measured envelopes of water surface fluctuations.

The high frequency of laser sampling allows for a highly illustrative and simultaneous representation of water level fluctuations across the entire channel cross-section. To represent the simultaneous changing of the surface in the measured section, simultaneous measurements in a mesh of points, not only in cross-sections, and additional analysis of a raw data are required.

4 CONCLUSIONS

The undeniably wide applicability of laser scanning is particularly evident in solid state measurements if, given the complexity of surface morphology, an adequate number of observation points is selected. In their tests – but with the addition of particulate matter into the water to improve reflectivity – some authors confirmed the applicability of the laser method also when measuring the travel and transformation of waves, but mostly with a slower dynamic than in our case. An added value of this measuring method has been created by the results of this study, which testify to the method's efficiency in model studies when clean water is used, both for standing water surface measurements and for acquisition of the water surface profile with a high time variability, whose dynamics cannot be captured by conventional measurements. Notably, this method gives very good results in the case of distinctively two-phase flows. In the case of water bodies with a relatively small content of air bubbles, or small density of two-phase flow in the upper layer, this measurement method is much less appropriate, water depths are underestimated, while a precise water surface formation is difficult to determine. Hydraulic phenomena with strongly aerated upper layers of water bodies with a continuous and homogenous layer of bubbles allow for a non-contact but very precise acquisition of transversal water surface formation and thus topography of water surfaces of complex cases with aerated flow and high vertical and horizontal dynamics. Data acquisition with high temporal and spatial resolution is, particularly in the cases with strongly diversified water surface in the transversal direction, important also for calibration and verification of numerical models, as nowadays even full 3D numerical models are unable to precisely simulate flow conditions at T-junctions, i.e. in areas with a simple enough channel geometry. The construction of water surface topography from the raw point cloud of measurements using laser scanning allows for determination of waving characteristics, a further analysis of flow conditions, and the determination of the main flow structures at the confluence and its characteristics as a function of integral parameters in both inflows, thus providing the background for determining the T-junction topology. With further assumptions and additional analysis of a raw reflection point cloud, it will be possible to analyse and evaluate practically simultaneous water surface fluctuations across the whole measured cross-sections, as the laser beam movement dynamics is considerably higher than the water surface changing dynamics.

5 REFERENCES

[1] Webber, N.B., Greated, C.A. (1966). An investigation of flow behavior at the junction of rectangular channels. *Proceedings of the Institution of Civil Engineers*, vol. 34, no. 3, p. 321-334, **DOI:10.1680/iicep.1966.8925**.

[2] Biron, P.M., Ramamurthy, A.S., Han, S. (2004). Three-dimensional numerical modeling of mixing at river confluence. *Journal of Hydraulic Engineering*, vol. 130, no. 3, p. 243-253, **DOI:10.1061/(ASCE)0733-9429(2004)130:3(243)**.

[3] Pinto Coelho, M.M.L. (2015). Exprimental determination of free surface levels at open-channel junction. *Journal of Hydraulic Research*, vol. 53, no. 3, p. 394-399, **DOI:10.1080/00221686.2015.1013513**.

[4] Biron, P.M., Richer, A., Kirkbride, A.D., Roy, A.G., Han, S. (2002). Spatial patterns of watter surface topography at a river confluence. *Earth Surface Process and Landforms*, vol. 27, no. 9, p. 913-928, **DOI:10.1002/esp.359**.

[5] Mignot, E., Riviere, N., Perkins, R., Paquier, A. (2008). Flow patterns in a four-branch junction with supercritical flow. *Journal of Hydraulic Engineering*, vol. 134, no. 6, p. 701-713. **DOI:10.1061/(ASCE)0733-9429(2008)134:6(701)**.

[6] Schwalt, M., Hager, W.H. (1995). Experiments to supercritical junction flow. *Experiments in Fluids*, vol. 18, no. 6, p. 429-437, **DOI:10.1007/BF00208465**.

[7] Bric, V., Berk, S., Triglav Čekada, M. (2013). Quality assurance of georeferencing airborne laser scanning data for water resource management. *Geodetski vestnik (Journal of the Association of Surveyors of Slovenia)*, vol. 57, no. 2, p. 257-285, **DOI:10.15292/geodetski-vestnik.2013.02.271-285.** (in Slovene)

[8] Mongus, D., Triglav Čekada, M., Žalik, B. (2013). The analysis is of an automatic method for digital terrain model generation from lidar data on Slovenian test cases. Geodetski vestnik *(Journal of the Association of Surveyors of Slovenia)*, vol. 57, no. 2, p. 245-259, **DOI:10.15292/geodetski-vestnik.2013.02.045-259.** (in Slovene)

[9] Rak, G., Steinman, F., Gosar, L. (2008). Analysis of hydraulic properties of watercourses using GIS tools (Analiza hidravličnih lastnosti vodotokov z uporabo GIS orodja). *GISs in Slovenia 2005-2006 (Geografski informacijski sistemi v Sloveniji 2005-2006)*, p. 123-131. (in Slovene)

[10] Allis, M.J., Peirson, W.L., Banner, M.L. (2011). Application of LIDAR as a measurement tool for waves. *Proceedings of the 21st International Offshore and Polar Engineering Conference*, p. 19-24.

[11] Blenkingsopp, C.E., Turner, I.L., Allis M.J., Peirson, W.L., Garden, L.E. (2012). Application of LiDAR technology for measurement of time-varying free-surface profiles in a laboratory wave flume. *Coastal Engineering*, vol. 68, p. 1-5, **DOI:10.1016/j.coastaleng.2012.04.006**.

[12] Streicher, M., Hofland, B., Lindenbergh, R.C. (2013). Laser ranging for monitoring water waves in the new Deltares Delta Flume. *ISPRS Annals of the Photogrammetry, Remote Sensing and Spatial Information Sciences*, vol. 2, no. 5, p. 271-276, **DOI:10.5194/isprsannals-II-5-W2-271-2013**.

[13] Hofland, B., Diamantidou, E., van Steeg, P., Meys, P. (2015). Wave runup and wave overtopping measurements using a laser scanner. *Coastal Engineering*, vol 106, p. 20-29, **DOI:10.1016/j.coastaleng.2015.09.003**.

[14] Rak, G., Hočevar, M., Steinman, F. (2017). Measuring water surface topography using laser scanning. *Flow Measurements and Instrumentation*, vol. 56, p. 35-44, **DOI:10.1016/j.flowmeasinst.2017.07.004**.

Strojniški vestnik - Journal of Mechanical Engineering 64(2018)9, 566-576

DOI:10.5545/sv-jme.2018.5262
Original Scientific Paper
Received for review: 2018-02-05
Received revised form: 2018-06-06
Accepted for publication: 2018-07-03

Experimental Hydraulic Analysis of Intake Structure for Cooling Towers Pumps

Gregor Žvab[1,*] – Gregor Lapuh[2]
[1] Kolektor-Turboinštitut d.o.o., Slovenia
[2] Krško Nuclear Power Plant, Slovenia

Experimental hydraulic analysis of troubleshooting intake structures for cooling towers (CT) pumps in nuclear power plant are presented in this paper. The formation of the free surface vortex in the pump sump with unfavorable intensity was not acceptable for the safe operation of the cooling towers pump and the cooling system in general. The objective of the present study is to investigate and improve hydraulic flow conditions in intake structure of CT pumping stations within acceptable criteria of the ANSI/HI standard experimentally. For this purpose, the physical hydraulic model with the scale factor 16 was made. Boundary conditions were calculated by dimensional analysis with the Froude number. The vorticity of flow in the suction pipe of the model pumps was measured and free surfaces and submerged vortices were observed. The model tests were made for all operating conditions of pumps. Comparison between the model and prototype showed a good agreement by the formation of an identical free surface vortex in the same area of the sump. In order to prevent the formations of the unfavorable free surface vortex, the geometry of intake structures with the additional elements and obstacles were modified. Measured and observed results for additional tests have been obtained. The optimized geometry of intake structures provided favorable flow conditions by safety factor 1.5 within acceptable criteria of the ANSI/HI standard.
Keywords: intake structures, physical hydraulic model, free surface flow, free surface vortices, vertical pump

Highlights

- *The troubleshooting of formations the free surface vortices in the pump sump with unfavorable intensity was not acceptable for the safe operation of the pump, therefore an experimental hydraulic analysis was carried out to improve the flow conditions of pump intakes in accordance of the ANSI/HI standard.*
- *Comparison between the model and prototype showed a good agreement by the formation of an identical free surface vortex in the same area of the sump.*
- *The study confirmed previous research that a strong cross flow near the pump intakes results in the formation of more intense streamlines at the free surface level.*
- *The undesirable influence of the cross flow was successfully prevented.*

0 INTRODUCTION

The inlet structures are a segment of the pumping system through which a source of fluid is supplied, and should be directed toward the pump intakes as uniformly as possible. Improperly designed intake structures can lead to unfavorable hydraulic disturbances in the flow which adversely affect the pump operation in its entire lifetime [1]. Consequently, it leads to poor pumping efficiency, damage to the vital parts of the pump, or even to failure [2]. In case of failures, additional maintenance work and remediation are required which impair the pump availability and the pump economy [3]. In general, intake structures are divided into clear liquid and intake structures for solid bearing liquid. After that, intake structures are further divided into different shapes of geometry. To prevent unfavorable hydraulic disturbance, additional elements and obstacles are installed into the sump. Unfavorable hydraulic disturbances occur in the form of surface and sub-surface vortices, non-uniform axial velocities of the flow at the pump inlet, and the leak of air and air bubbles into the pump [1].

The beginnings of the experimental research of undesirable hydraulic phenomena in intake structures date to 1950 [4]. Since then, numerous empirical relationships have been obtained between the geometric and hydraulic parameters of the pump, intake structures, and unfavorable hydraulic phenomena in the flow. Recommendations have been obtained through researches and developments in the pump industry from different authors until now. Guidelines for the design of intake structures are compiled in the ANSI/HI standard [4].

From case to case, intake structures require specific design because of different boundary conditions. In general, empirical results, correlations, and different parameter relationships are difficult to apply in the specific case. The ANSI/HI standard recommends the physical model tests for the design of a flow of pump greater than 2.5 m³/s and the pump station flow greater than 6.3 m³/s.

*Corr. Author's Address: Kolektor- Turboinštitut d.o.o., Slovenia, gregor.zvab@litostrojpower.eu

In general, it is recommended that a direction of approaching flow should coincide with the flow direction near the pump intake. Otherwise, the unfavorable cross-flow may appear near the pump [5]. In case of intense cross flow in the pump sump, the streamlines of flow become more intense at the free surface of the liquid. If the pump is not sufficiently submerged, it may lead to the formation of free vortices. During past experimental studies, numerous authors focused on the critical submergence of the pump (*Scr*). Quick [6] was the first to describe the *Scr* parameter by formations of free surface vortices. It is the relationship between pump bell diameter *D* and Froude (*Fr*) number. The effect of Reynolds (*Re*) number and Weber number (*We*) was investigated by numerous authors. They concluded that it can be neglected in case of sufficiently large *Re* and *We* numbers. Subsequently, the limit values for *Re* and *We* were recommended in the ANSI/HI standard [4].

The geometry of intake structures and of the pump also has an important influence on unfavorable hydraulic disturbances. For example, pre-swirl near the pump bell is increased if the distance between the pump axis and the back wall or the side wall is increased excessively [7]. The similar results were also obtained by Padmanabhan and Hecker [8] and by Anwar and Amimilett [9] studies. Studies by Quick [6] and Tagamori and Ueda [10] confirmed that reduction of the back wall, side wall, and the bottom floor clearances increases the risk of formation of subsurface vortices which originate from there. For this purpose, various elements and obstacles must be properly installed near the pump intake. In addition, Denny [7] suggested that geometry of the pump bell has a noticeable influence on flow separation and increases the non-uniform velocities in the approach flow. In the case of parallel installation of pumps, it can cause interaction of flows between pumps which are installed too close to the sump. For this purpose, it is necessary to design intermediate walls between pumps to prevent flow interaction. For dissipation water energy, different elements and obstacles are also installed to reduce flow velocities and other undesirable hydraulic phenomena. The velocity of flow can also be reduced with the gradual expansion of side walls in the pump sump.

In recent studies for examining the flow pattern in the approaching flow, acoustic Doppler velocimetry (ADV) was employed [11]. Hwang and Yang [12] experimentally measured approaching flow using ADV and swirl meter and provide valuable information for practical application.

Flow conditions in intake structures can also be predicted with the computational fluid dynamic (CFD). Numerous authors [13] to [16] simulated flow patterns using advanced numerical modeling. They also compared or validated their simulations with measurements taken using particle image velocimetry (PIV). Calculation of free surface flow with formations of vortices usually requires extremely fine meshing and advanced turbulent models with considerations of two-phase flow. However, this is limited by the computational power and storage [4].

The experimental study deals with the hydraulic analysis in practice. The formation of the free surface vortex in the pump sump with unfavorable intensity was not acceptable for the safe operation of the CT1 pump and cooling system in general. The objective of the present study is to experimentally investigate and improve hydraulic flow conditions in intake structure of CT pumping stations within acceptable criteria of the ANSI/HI standard. For the purpose of the study, detailed knowledge of the flow conditions at the pumping station was needed.

1 METHODS

Using the design requirements given in the ANSI/HI standard, the geometry and hydraulic parameters for the intake structure and the pump must be properly selected for satisfactory hydraulic performance. Fig. 1 shows the design criteria for rectangular intake structures for clear liquids in plan and elevation view.

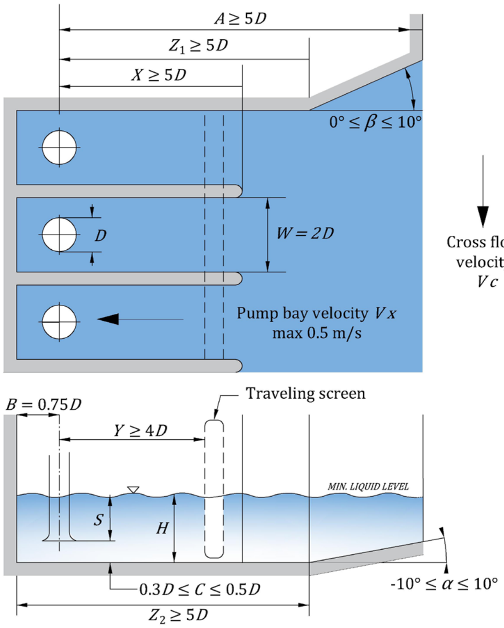

Fig. 1. *Design criteria for the rectangular intake structures*

A physical hydraulic model study shall be conducted for rectangular intake structures with one or more of the following features:

- Sump or pump geometry deviates from recommendations of the ANSI/HI standard.
- Non-uniform of non-symmetric approach flow to the pump sump exists.
- The flows of the pumps greater than 2.5 m³/s per pump or the total station flow with all the pumps running would be greater than 6.3 m³/s.
- The cross-flow velocity (Vc) in the sump exceeds 50 % of axial velocity in the pump intake.
- Traveling or static screen is mounted in the sump.

1.1 Physical Hydraulic Modeling of Free Surface Flow

The mathematical models of the flow of real liquid can be solved by simplified models alone. Therefore, the solutions for many engineering problems are achieved through the use of a combination of theoretically and experimentally obtained data [17]. In this chapter, we consider dimensional analysis, similitude and experimental modeling of free surface flow, as well as measuring techniques in acceptance to the ANSI/HI standard.

A model is a representation of a physical system that may be used to predict the behavior of the system in some desired respect. The physical system for which the predictions are to be made is called the prototype [17]. The theory of models can be readily developed by using the Buckingham theorem, which is the basis of the dimensional analysis. The model is accurate when all the dimensionless numbers that affect the physical phenomenon are the same on the prototype. In other words, we have to maintain geometric, dynamic, and kinematic similarity.

Flows in canals, rivers, basins, as well as flows around ships, are examples of flow phenomena involving a free surface flow. As shown in Eq. (1), dimensionless groups are affected by the phenomena. The first group L_i/L indicates the scale factor of the model. The next group ε/L indicates the relative roughness, and the last groups indicate Reynolds (Re), Froude (Fr) and Weber number (We). The influence of viscous effects is defined by the Re, Fr representing the ratio of inertial to gravitational forces, while We represents surface tension effect.

$$\Pi_i = \varphi\left(\frac{L_i}{L}, \frac{\varepsilon}{L}, Re, Fr, We\right), \tag{1}$$

$$Fr = \frac{V}{\sqrt{g \cdot D}}, \tag{2}$$

$$Re = \frac{V \cdot D}{\nu}, \tag{3}$$

$$We = \frac{\rho \cdot V^2 \cdot D}{\sigma}. \tag{4}$$

In practice, we must not change the kinematic viscosity and surface tension of the water drastically, so that the models involving free-surface flow are usually distorted. Fortunately, in many problems involving free-surface flows, both surface tension and viscous effects are small and, consequently, the similarity of We and Re number is not required. Therefore, in free surface flow, Fr becomes an important similarity parameter [17] and [18].

$$Fr_M = Fr_P. \tag{5}$$

By use of Eq. (6) which is derived from dimensional analysis, it may be shown that a given vortex type is a function of various dimensionless parameters. Where S/D is the ratio between submergence of the pump and pump bell diameter, L_i/L is a scale factor between model and prototype, N_T is circulation number of approach flow and the last one is Froude number.

$$\Pi_i = \varphi\left(\frac{S}{D}, \frac{L_i}{L}, N_T, Fr\right). \tag{6}$$

For example, if a scale factor is constant, the equation is simplified with Eq. (7) where terms Fr and S/D describe a family of curves. Each one represents different values of vortex strength. There are many equations in the literature with a different relationship between Scr and Fr. The ANSI/HI standard uses Eq. (8) by Hecker [4].

$$\Pi_i = \varphi\left(\frac{S}{D}, Fr\right), \tag{7}$$

$$S_{CR} = D\left(1 + 2.3 \cdot Fr\right). \tag{8}$$

1.2 Physical Model Study Scope

The objective of the model study is not to investigate flow patterns but to ensure that final sump or piping design generate favorable flow conditions at the inlet to the pump. For studying the potential formation of vortices, it is important to select a reasonably large geometric scale to minimize viscous and surface tension scale effect. The model shall also be large enough to allow visual observations of flow pattern, accurate measurements of swirl and velocity distribution. Selection of the model boundary is also extremely important for a proper simulation of flow patterns at the pump. As the approach flow non-uniformities contribute significantly to the undesirable hydraulic phenomena, a sufficient area of the approach geometry has to be modeled, including any channel transition or expansions, obstacles, gates, and any significant cross-flow past the intakes [4].

1.2.1 Observation of Pump Inlet Disturbances

The outflow from each simulated pump shall be measured with flow meters. The accuracy of the flow measurements shall be within ±2 % of the actual flow rate. Liquid surface elevation shall be measured using any type of liquid level indicator with the accuracy of at least 3 mm.

To elevate a vortex strength scale, which varies from a surface swirl to an air core vortex, is shown in Fig. 2. Vortices are usually unsteady and, hence, the vortex type shall be estimated through short time interval and determined with an average type during the observation. Subsurface vortices which are determined by the same procedure usually originate at the sump floor and walls and may be visible only when the dye is injected near the vortex core [4].

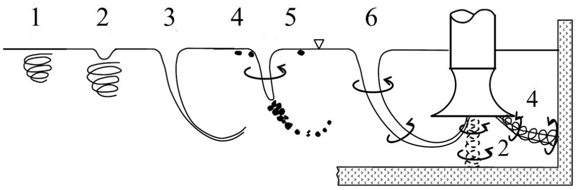

Fig. 2. *Classification of free surface and subsurface vortices*

1.2.2 Measuring Swirl in the Pump Suction Pipe

The intensity of flow rotation shall be measured using a swirl meter (see Fig. 3). It shall consist of a straight-vanned propeller with four vanes mounted on a shaft with low-friction bearings, installed in the suction pipe and dimensioned in acceptance to the ANSI/HI standard.

The revolution per unit time of the swirl meter is used to calculate a swirl angle θ by Eq. (9). Where d is a minimum diameter, u is averaged axial velocity in pump suction pipe, and n is a number of the revolution per second of the swirl meter [4].

$$\theta = \tan^{-1}\left(\frac{\pi \cdot d \cdot n}{u}\right). \qquad (9)$$

In the standard measurement techniques, the measurement of cross-sectional velocity profiles of the approach flow in pump suction pipe is also included. For the purpose of this study, the velocity profiles in pump sump were only measured (see Figs. 10 and 11). The measurement of velocity profiles in pump suction pipe in this study was not included.

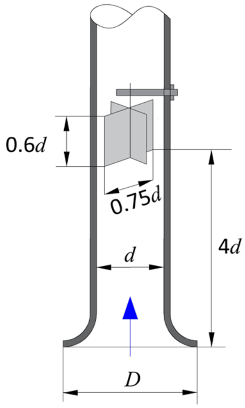

Fig. 3. *Typical swirl meter*

2 EXPERIMENTAL

2.1 Analysis of CT Pumping System

The tertiary-cooling system in the Nuclear power plant (see Fig. 4) consists of the condenser, the circulation water (CW) pumping system, the cooling tower (CT) pumping system, the cooling towers, channels, and piping.

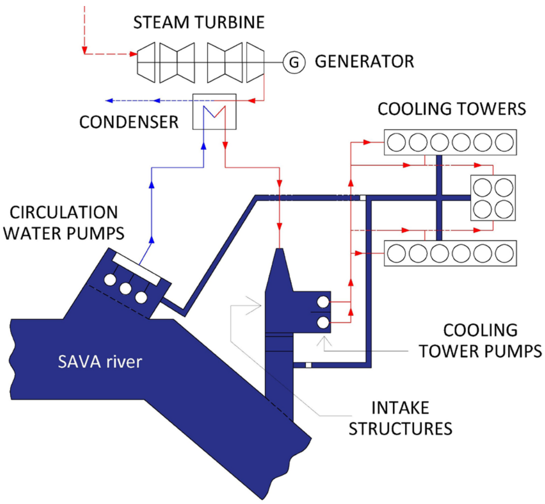

Fig. 4. *Scheme of the cooling system in the Nuclear Power Plant in Krško*

The cooling system is designed to cool the condenser and dissipate the steam heat that cannot be usefully employed to produce electricity. The

CW pumps force water from the Sava river into the condenser and back into the river. As it passes through the condenser, the river water heats up because it absorbs heat from the used steam. Since heating the water of the Sava results in the thermal pollution of the river, administrative regulations specify the permitted increase in temperature and the percentage of the river's flow that can be diverted for power plant cooling. In the case of unfavorable meteorological conditions, the cooling towers are used [19].

When only half blocks of the CT operate, only the CT1 pump operates at the CT pumping system. During the summertime, all blocks of the CT usually operate. In this case, both of the CT pumps operate in parallel. The pumps have the same design point with the flow rate of 8.5 m^3/s, the head 25 m, and the rotation speed of 427 rpm. The open impeller is semi-axial with specific speed (nq = 108). The cooling water is pumping through the pipeline with the diameter 1800 mm to the CT.

The rectangular intake structure on the CT pumping system in Fig. 5 consists of an inlet channel, an extension, an intake sump, and a dam. The pumps are divided by an intermediate wall in the sump. The heated water approaches from the condenser through the inlet channel into the intake structure extension where it decelerates the pump sump. During operation of cooling towers, CT pumps pump the required flow of water in the cooling tower. The remaining heated flow of water flows through the dam to the Sava river.

The formation of the free surface vortex in the pump sump with the type 6 (Fig. 5b) was not acceptable for the safe operation of the pump CT1 and the cooling system in general. The intake structure was investigated with the recommendations of the ANSI/HI standard. The investigation shows some deficiency which was not taken into the initial design. There, it was found that velocity of cross-flow Vc is too high, the width W of the intake channel is too wide, and the distance B and the distance X of the intermediate wall are shorter than recommended.

2.2 Design of Physical Hydraulic Model

2.2.1 Physical Hydraulic Model

Physical hydraulic model (see Fig. 6) was made in the laboratory for turbomachines at the Kolektor Turboinstitut. It contains a model, a small closed-circuit pumping system with the regulation system and the measuring system. The total flow rate regulation was set with a variable frequency of the pump. The flow rate through the model pumps was regulated by valves on the suction pipes. The intake flow rate was measured by the orifice plate D/d = 90/120 and the pressure transducer. The flow rate over the dam was measured by an electromagnetic flow meter. So the difference between each flow rate means the flow through the model pumps. At the recommended level in the suction pipe of the model pump, standard swirl meter was installed (see Fig. 7c). simultaneously. The water level near the pump was measured by the meter with the accuracy of 2 mm. The errors of flow measurement instruments are presented in Table 1, where e_1 is a systematic error and e_2 is a random error.

Table 1. *Errors of instruments*

Instrument	e_1	e_2
Pressure transducer/orifice plate	0.1	0.6
Electromagnetic flow meter	0.5	0.2

The investigation of vortices was carried out by observation over the transparent walls around the

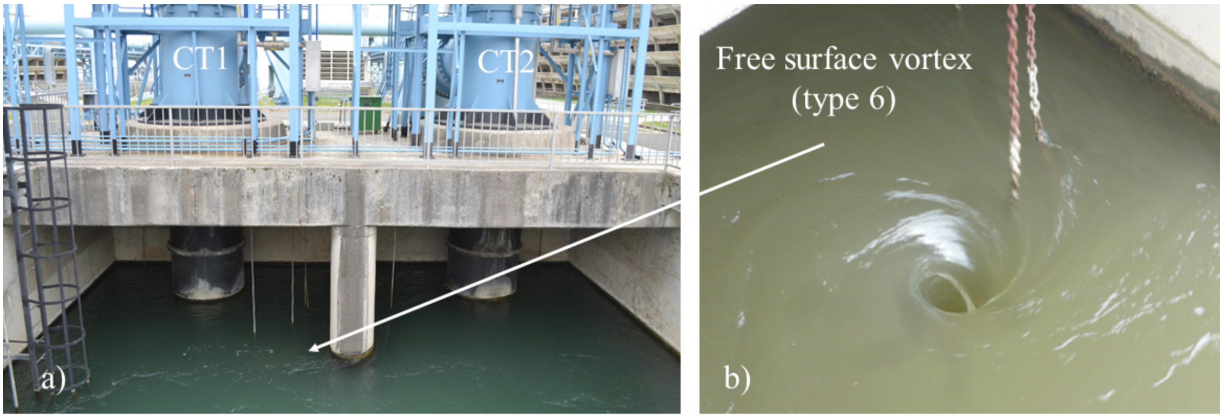

Fig. 5. *a) CT pumps with intake structures, b) free surface vortex (type 6) [20]*

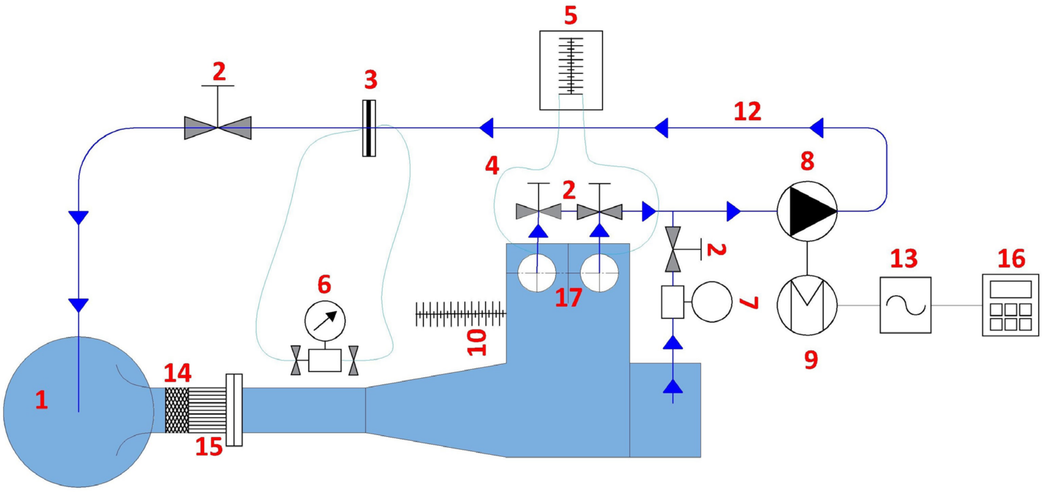

Fig. 6. *Test rig of hydraulic model; (1) surge tank, (2) regulating valves, (3) orifice plate, (4) Pitot tube, (5) static head, (6) pressure transducer, (7) electromagnetic flow meter (8) pump, (9) motor, (10) liquid level meter, (11) suction pipe, (12) pressure pipe, (13) frequency converter, (14) mesh, (15) honeycomb tubes, (16) control unit, (17) model pumps*

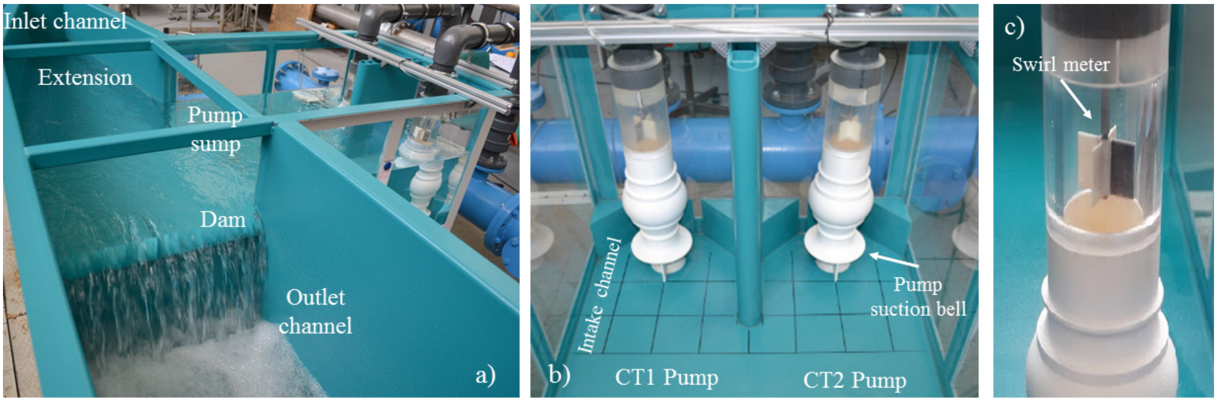

Fig. 7. *Physical hydraulic model in the laboratory; a) pump sump with the dam, b) model pumps with the intermediate wall, c) swirl meter [20]*

sump. The vortices were documented with a photo and a camera. Subsurface vortices were observed by the injected dye near the pump intake (Fig. 8c).

2.2.3 Similarity

A model was designed with the scale factor 16. Hydraulic geometry included an intake channel, an extension, a sump, a model pump suction pipes, and a dam (see Fig. 7a). It was assumed that the outflow channel of the CT pumping system did not have any hydraulic influence on flow condition near the pumps. The walls and floor of the physical model are built with sheet metal and the model pumps are made by 3D print technology (see Fig. 7b). The influence of impeller on flow patterns in the pump intake was neglected in accordance with the ANSI/HI standard. The uniform velocity profile in the inlet channel was simulated by installed meshes and small pipes into the inlet channel. The measuring of depression at the free-surface level was neglected.

2.2.3 Calibration of the Model

All the hydraulic dimensions of the model are reduced with the same scale factor. Therefore, geometric similarities were satisfied. The kinematic similarity was satisfied by the similar flows between the model and the prototype for all operating conditions, calculated with Eq. (5). Dynamic similarities were satisfied with the similarity of *Fr*. The conditions for the influence of viscous and surface tension were satisfied as well by Eqs. (10) and (11).

$$Re_M \geq 6 \cdot 10^{-4} \tag{10}$$

$$We_M \geq 240 \tag{11}$$

2.2.4 Measurement Uncertainty

The measurement uncertainty of filed measurement was neglected. The measurement uncertainty of the intake flow rate e_{Qz} is calculated by Eq. (10), where e_{z1} is a systematic error of differential pressure transducer, e_{z2} is a random error of flow through the orifice plate. The measurement uncertainty of the flow rate over the dam e_{Qd} is calculated by Eq. (11) where e_{d1} is a systematic error of flow meter; e_{d2} is a random error of flow through the orifice plate. The measurement uncertainty of the total flow rate e_Q calculated by Eq. (12) is a geometric sum of measurement uncertainty of e_{Qz} and e_{Qd}.

$$e_{Qz} = \sqrt{e_{z1}^2 + e_{z2}^2} = \sqrt{0.1^2 + 0.6^2} = 0.7\ \%, \quad (10)$$

$$e_{Qd} = \sqrt{e_{d1}^2 + e_{d2}^2} = \sqrt{0.5^2 + 0.2^2} = 0.5\ \%, \quad (11)$$

$$e_Q = \sqrt{e_{Qz}^2 + e_{Qd}^2} = 0.86\ \%, \quad 0.86\ \% < 2\%. \quad (12)$$

3 RESULTS

Model tests were carried out in accordance with the ANSI/HI standard. The observations of the undesirable hydraulic phenomena were investigated for all the operating conditions. In addition, the tests were divided on the existed and planned state. For the planned state a higher level of the dam is designed. Hence, the water level in pump sum will be higher. Despite favorable effect on the formation of surface vortices, it is necessary to investigate the flow conditions in both cases.

The results of model tests are given in two parts. In the first part, the results for the existing and the planned state are given. In the second part, we show the results of the tests with the optimization of flow conditions by the selected remedial measures.

3.1 The First Part

The existing state: during the operations condition of the CT1 pump, the formation of surface vortices (type 6) was observed (Fig. 8a). The undesirable hydraulic phenomena near the CT2 pump were not observed for all the operations conditions. Subsurface vortices near the pump intake were not observed for any conducted tests (Fig. 9a). The submergence of the pumps *Scr* calculated by Hecker Eq. (8) was satisfied for all the operation conditions (Table 2). The excessive swirl angle was only observed in the CT1 pump during the individual operating (Table 3).

Planned state: during the tests with the higher water level in the intake sump, the formations of surface vortices (type 5) were observed (Fig. 9b). During the operations condition of the pump operated in parallel, free-surface vortices with lover intensity (type 3) were observed. Subsurface vortices were not observed in any tests again. The excessive swirl angle was observed during the operations conditions of the CT1 pump again (Table 3).

Table 2. *Data of the measured submergence and critical submergence of the model pumps*

	Existing state		Planned state	
Operation	S [m]	Scr [m]	S [m]	Scr [m]
CT1	0.236	0.286	0.299	0.293
CT2	0.236	0.286	0.299	0.293
CT1+CT2	0.217	0.286	0.280	0.293

Results in Table 2 show lower S for parallel operation conditions because of higher depression on

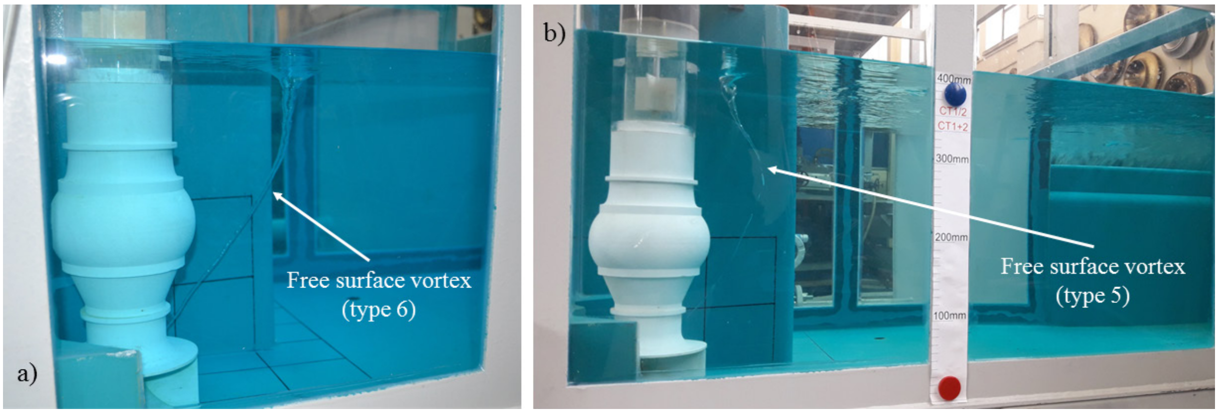

Fig. 8. *a) observing the free surface vortices of the existing state and, b) the planned state [20]*

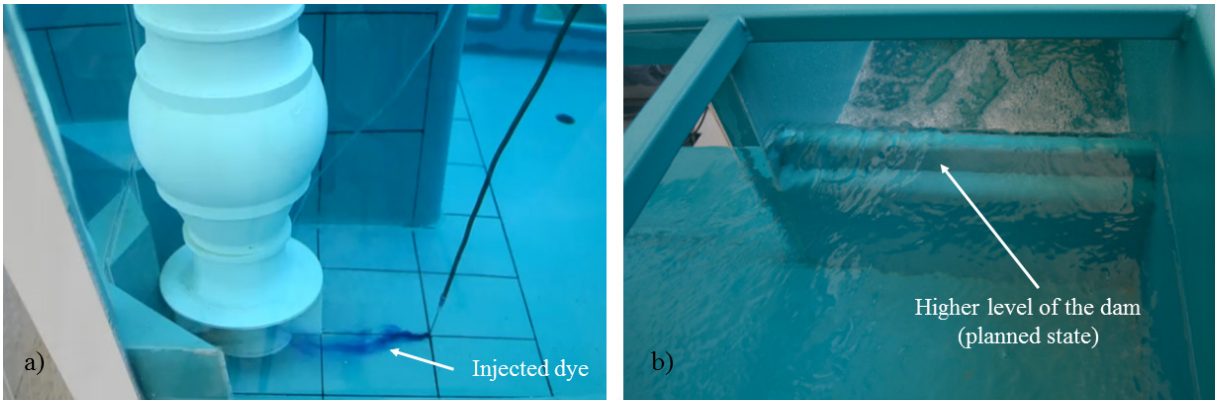

Fig. 9. *a) observation of the submerged vortices by injecting dye below the water surface, b) the installed higher level of the dam for the planned state [20]*

water surface level near the intake of the pump. For the planned state, a higher *Fr* and *V* were expected in pump suction pump, so we obtained higher *Scr* consequently.

Table 3. Calculated swirl angle θ

	Existing state		Planned state	
	CT1	CT2	CT1	CT2
Operation	θ [°]	θ [°]	θ [°]	θ [°]
CT1	10.8	-	6.3	-
CT2	-	3.31	-	2.44
CT1+CT2	6.9	3.2	6.49	1.8

Results in Table 3 show correlations with swirl angle θ and surface vortices. When the surface vortex was formed near the pump intake, the excessive swirl angle θ has been observed at the same time.

Sketches of the flow: by the comprehensive observations of the flow patterns, it was possible to find out the main reasons for formations of free-surface vortex near the CT1 pump intake. The cross-flow velocity *Vc* at the intake of the pump sump has been exceeded [4]. The main flow was oriented over the dam, because of the powerful inertia of the high water velocity *Vc*. Velocity profile *Vx* did not coincide with the axis of the CT1 pump due to stagnant and therefore unstable liquid in pump sump. CT1 pump sucked the water only from opposite site of the CT2 pump and, hence, the edge of the intermediate wall formed the flow separation at the free surface around it. Consequently, flow separation formed a coherent air core at the free surface near the CT1 pump intake (see Fig. 10).

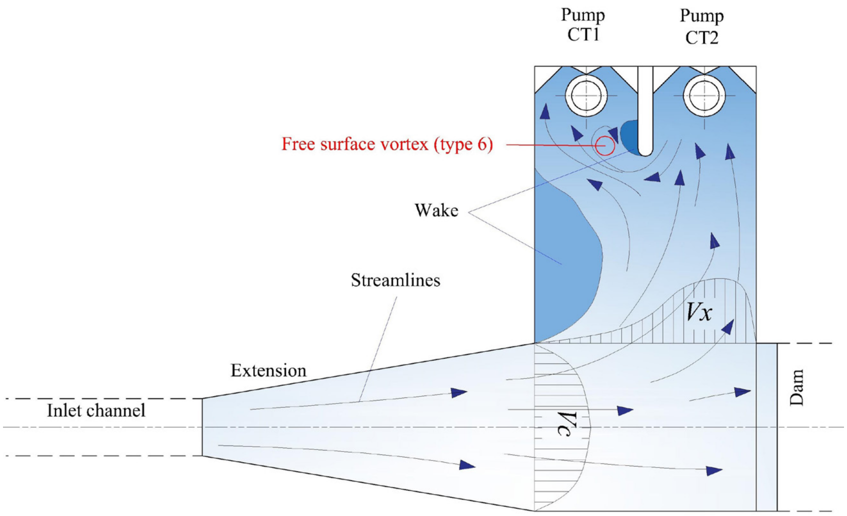

Fig. 10. *Sketch of the flow visualization for an individual operation of the CT1 pump*

3.2 The Second Part

In order to perform a uniform flow pattern in the approach flow, the appropriate measures with modification geometry of the intake structure have been selected. The measure has been selected on the basis of our experiences and recommendations of the ANSI/HI standard. In the intake sump, the additional inlet wall (Fig. 11a), and the extended intermediate wall (Fig. 11b and c) were mounted. At measure 1 (Fig. 11a), it was necessary to improve the uniformity in the approach flow. Nevertheless, free-surface vortices were still observed. At measure 2 (Fig. 11b), the extended intermediate wall was mounted into the pump sump. The favorable flow conditions in the approach flow were provided.

In order to reduce the construction cost, the same test without an inlet wall was conducted, and the similar results were obtained. The final test was repeated with a higher flow rate by the safety factor 1.5. The optimized geometry of the intake structure with measure 3 (Fig. 11c), provided favorable flow conditions within the acceptable criteria of the ANSI/HI standard.

4 DISCUSSION

Physical hydraulic model of the free surface flow for the intake structures is still an appropriate approach for flow pattern predictions near the pump intake [2] and [4]. In our case, there was a troubleshooting of formations of the free surface vortices (type 6) near the CT1 pump intake, which was not acceptable for safe operation of CT pumping station. Improperly designed intake structure has been analyzed in accordance with the ANSI/HI standard. Intensive free surface vortices may be reduced with increasing depth of submergence S [2] and [4]. During all the tests, the condition $S >$

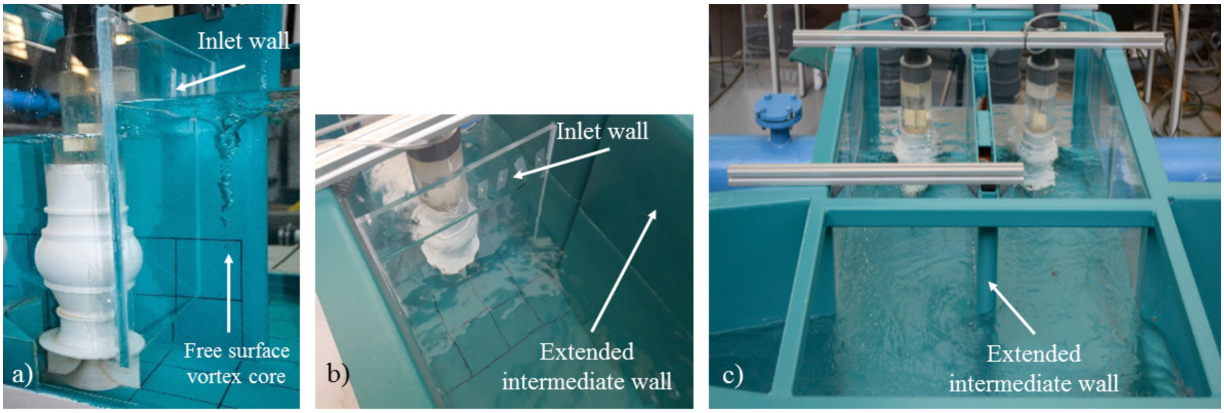

Fig. 11. *The selected remedial measures; a) measure 1, b) measure 2, c) measure 3 [20]*

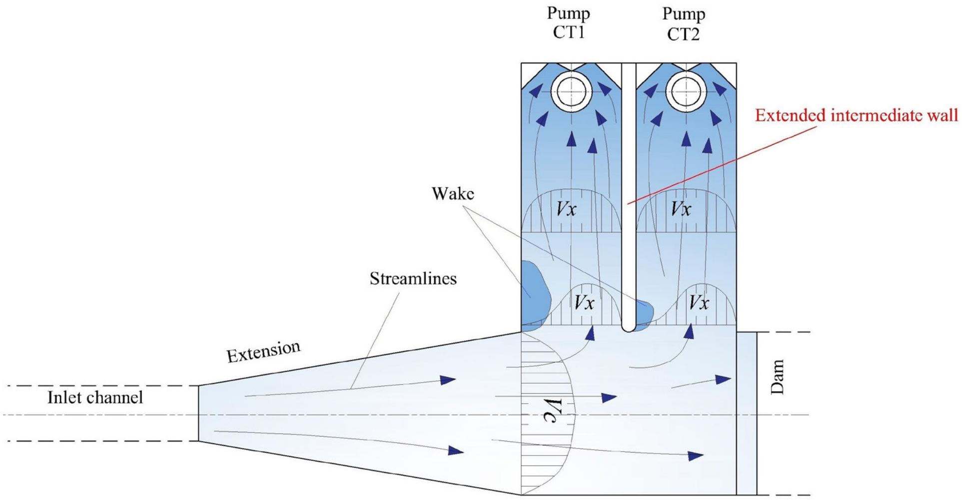

Fig. 12. *Sketch of the flow visualization for measure 3 with installed extended intermediate wall (parallel operation of pumps)*

Scr was fulfilled by Eq. (8), Nevertheless, a free surface vortex was forming. However, there are also situations where increasing depth has negligible effect or even increases free surface vortex formations due to stagnant and therefore unstable liquid [4]. As studied by Ansar [5], Ansar and Nakato [11] and Gülich [2], a strong cross flow near the pump intake results in the formations of more intense streamlines at the free surface level. In our case the reason for formation of free surface vortex (type 6) was already explained in the part of the chapter 3 (Sketches of the flow). The undesirable influence of the cross flow was successfully prevented by the installation of the extended intermediate wall between the pumps (see Fig. 12).

5 CONCLUSIONS

The study was focused on the design of the intake structure physical model tests to optimize undesirable hydraulic phenomena in free surface flow by the appropriate selection of remedial measures which will be able to apply on the prototype in the CT pumping station in the Nuclear power plant after the investigation. The important outcome of this analysis also confirms a good predictions of flow conditions between prototype and model tests carried out in accordance with the ANSI/HI guidelines. Experiences obtained during analysis can be used in other practical cases for intake structures design with similar geometry.

During the model tests, the three selected remedial measures are investigated. Although, it will be possible to study some useful empirical relationships for different hydraulic or geometry parameters. We must be satisfied by only three remedial measures because the practical studies are also limited by deadline and budget.

The pump inlet disturbances contain a series of flow phenomena and hence, the careful should be taken into account during the intake structure design process. The physical model represents an additional cost during the design process. Nevertheless, these costs are significantly lower compared to the costs which arise in the case when troubleshooting appears during the operation of the pumping system. A rehabilitation of the pumping system during the operations can be costly and demanding. In addition, it reduces the availability of the pumping system, which consequently results in a greater financial loss [1] and [3].

6 ACKNOWLEDGMENTS

The study is the result of the years of cooperation between the Nuclear Power Plant Krško and the Kolektor Turboinštitut.

7 NOMENCLATURES

D suction bell diameter, [mm]
B distance from the back wall to the pump, [m]
C the distance between the inlet bell and floor, [m]
d suction channel diameter, [mm]
ε relative friction ratio, [-]
e_{d1} systematic error of flow meter, [-]
e_{d2} random error of flow through the orifice plate, [-]
e_{z1} systematic error of pressure transducer, [-]
e_{z2} random error of pressure transducer, [-]
e_Q total measurement uncertainty of flow rate, [-]
e_{Qd} measurement uncertainty of the flow rate over the dam, [-]
e_{Qz} measurement uncertainty of the intake flow, [-]
Fr Froude number, [-]
g gravity acceleration, [m/s²]
L length, [m]
n angular velocity, [-]
nq specific speed of the pump, [-]
ρ density, [kg/m³]
ν kinematic viscosity, [m²/s]
Re Raynolds number, [-]
S submergence, [mm]
Scr critical submergence, [mm]
X pump inlet bay length, [m]
Q flow rate, [m³/s]
V flow velocity, [m/s]
Vc cross-flow velocity, [m/s]
Vx pump bay velocity, [m/s]
W pump bay entrance width, [m]
We Weber number, [-]
u axial velocity, [m/s]
θ vorticity angle, [°]
Z_1 distance from pump inlet bell centerline to diverging walls, [m]

8 REFERENCES

[1] Florjančič, D. (2008). *Trouble-shooting, Handbook for Centrifugal Pumps*. Turboinštitut, Ljubljana.
[2] Gülich, J.F. (2013). *Centrifugal Pumps*. Springer-Verlag, Berlin.
[3] Hydraulic Institute (2001). *Pump Life Cycle Costs, A Guide to LCC Analysis for Pumping System*, Hydraulic Institute, Parsippany.
[4] ANSI/HI 9.8-2012 (2012). *Rotodynamic Pumps for Pump Intake Design*. American National Standard Institute, New Jersey.

[5] Ansar, M. (1997). *Experimental and Theoretical Studies of Pump Approach Flow Distributions at Water Intakes*. Ph.D. thesis, The University of Iowa, Iowa City.
[6] Quick, M.C. (1970). Efficiency of air-entraining vortex at water intakes. *Journal of the Hydraulics Division, American Society of Civil Engineers*, vol. 96, no. 7, p. 1403-1415.
[7] Denny, D.F. (1956). An experimental study of air-entraining vortices in pump sumps. *Proceedings of the Institution of Mechanical Engineers*, vol. 170, no. 1, p. 106-125, **DOI:10.1243/PIME_PROC_1956_170_019_02**.
[8] Padmanabhan, M., Hecker, G.E. (1984). Scale effects in pump sump models. *Journal of Hydraulic Engineering*, vol. 110, no. 11, p. 1540-1556, **DOI:10.1061/(ASCE)0733-9429(1984)110:11(1540)**.
[9] Anwar, H.O., Amimilett, M.B. (1980). Vortices at vertically inverted intake. *Journal of Hydraulic Research*, vol. 18, no. 2, p. 123-134, **DOI:10.1080/00221688009499556**.
[10] Tagamori, M., Ueda, H. (1991). An Experimental Study of Submerged Vortices and Flow Pattern in the Pump Sump. *Japanese Society of Mechanical Engineering*, Paper 91-0562, **DOI:10.1299/kikaib.57.3641**.
[11] Ansar, M., Nakato T. (2001). Experimental study of 3D pump-intake flows with and without cross flow. *Journal of Hydraulic Engineering*, vol. 127, no. 10, p. 825-834, **DOI:10.1061/(ASCE)0733-9429(2001)127:10(825)**.
[12] Hwang, K.S., Yang, C.H. (2003). *Hydraulics model testing of circulating-water pump sump in Shen-Ho power plant*, Research Report 293. Taiwan Hydraulics Laboratory, Tainan.
[13] Li, S., Lai, Y., Weber, L., Silva, J.M., Patel, V.C. (2004). Validation of a three-dimensional numerical model for water-pump intakes. *Journal of Hydraulic Research*, vol. 42, no. 3, p. 282-292, **DOI:10.1080/00221686.2004.9728393**.
[14] Tokyay, T.E., Constantinescu, S.G. (2006). Validation of a large-eddy simulation model to simulate flow in pump intakes of realistic geometry. *Journal of Hydraulic Engineering*, vol. 132, no. 12, p. 1303-1315, **DOI:10.1061/(ASCE)0733-9429(2006)132:12(1303)**.
[15] Yuilin, W., Yong, L., Xiaoming, L. (2000). *PIV Experiments on Flow in a Model Pump Suction Sump, Research Report*, Thermal Engineering Department, Tsinghua University, Beijing.
[16] Škerlavaj, A., Vehar, F., Pavlin, R., Lipej, A. (2009). A hydraulic study of cooling water intake structure. *Proceedings of the 3rd IAHR International Meeting of the Workgroup on Cavitation and Dynamic Problems in Hydraulic Machinery and Systems*, p. 143-154.
[17] Munson, B.R., Okiishi, T.H., Huebsch, W.W., Rothmayer A.P. (2012). *Fundamentals of Fluid Mechanics*, Wiley, Hoboken.
[18] Franch, R.H. (1986). *Open-Chanel Hydraulic*. Mc Graw-Hill, Singapore.
[19] NEK (2017). P*lant System and Operation*, from *http://www.nek.si*, assessed on 2017-10-10.
[20] Pavlin, R., Žvab, G. (2016). *Analyse of Pump Intake Conditions with Model Test: Analyse of Intake Structures with Model Test Procedure*, Report no.: 3164-1-0, Krško.

Vsebina

Strojniški vestnik - Journal of Mechanical Engineering
letnik 64, (2018), številka 9
Ljubljana, september 2018
ISSN 0039-2480

Izhaja mesečno

Razširjeni povzetki (extended abstracts)

Strojniški vestnik - Journal of Mechanical Engineering 64(2018)9, SI 73

Prejeto v recenzijo: 2018-01-24
Prejeto popravljeno: 2018-06-04
Odobreno za objavo: 2018-06-20

Neustaljeni tlaki vplivani z ujetimi zračnimi mehurji v cevovodih napolnjenih z vodo

Anton Bergant[1,*] – Arris Tijsseling[2] – Young-il Kim[3] – Uroš Karadžić[4] – Ling Zhou[5] – Martin F. Lambert[6] – Angus R. Simpson[6]

[1] Litostroj Power d.o.o., Slovenija
[2] Tehniška univerza Eindhoven, Nizozemska
[3] Detection Services, Avstralija
[4] Univerza Črne gore, Črna gora
[5] Univerza Hohai, Kitajska
[6] Univerza v Adelaidi, Avstralija

Zračni mehurji ujeti v cevovodih napolnjenih z vodo (pretočni sistem hidroelektrarne, črpalni sistem) lahko povzročijo nekontrolirano obratovanje in poškodbe sistema (zrušitev gradnikov cevnega sistema). Prispevek obravnava dinamični odziv izoliranega zračnega mehurja. Zračni mehur, ki je izoliran v cevovodu (vzdolž cevi, na pregibih cevi, ob gradnikih sistema), povzroči značilne spremembe velikosti, oblike in časovnega poteka neustaljenih tlačnih valov. Intenziteta rezultirajočega hidravličnega prehoda je narekovana z volumnom, tlakom in tehniško razporeditvijo ujetega zračnega mehurja.

Teoretični model bazira na enčbah neustaljenega stisljivega kapljevinskega toka v ceveh. Transformacija postavljenih parcialnih diferencialnih enačb hiperboličnega tipa z uporabo metode karakteristik da navadne diferencialne enačbe, ki jih rešujemo s pomočjo diferenčne numerične metode. V deltoidno mrežo metode karakteristik je vgrajen Zielkejev konvolucijski model neustaljenega stenskega trenja. V Zielkejev model je vpeljana aproksimativna utežna funkcija, ki da računsko učinkovito konvolucijo z uvedbo eksponetnih funkcij. Vgradnja zračnih mehurjev oziroma mehurčkov (plinskih kavitacij) v numerična vozlišča da diskretni plinski kavitacijski model. Izolirani zračni mehur je glede na tehniško razporeditev obravnavan kot notranji ali robni element.

V prispevku obravnavamo dva karakteristična primera: (1) zagonski obratovalni režim (pospeševanje toka iz mirnega stanja) in (2) zapiralni obratovalni režim (zaustavitev pretoka). Zagonski preizkus smo izvedli na laboratorjski napravi Univerze Črna gora. Dolžina preizkusnega cevovoda je 55 m, notranji premer jeklene cevi pa 18 mm. Zračni mehur je izoliran (ujet) na dolvodnem koncu cevovoda. Prehodni pojav vzbudimo s hitrim odpiranjem ventila, ki ločuje vodni steber in zračni mehur. Razlika tlakov vode in zraka povzroči oscilacije vodnih in zračnih mas. Za primer v tem prispevku je tlak statičnega vodnega stebra na dolvodnem robu (ventil) 520 kPa, tlak v zračnem mehurju pa je enak tlaku okolice (atmosferski tlak). Prehodni pojav z ustavitvijo pretoka smo izvedli na preizkusni postaji Univerze v Adelaidi, Avstralija. Dolžina cevovoda je 37 m, notranji premer bakrene cevi pa 22 mm. V tem primeru je zračni mehur ujet na polovici dolžine cevovoda. Mehur je ujet v komori, ki je vgrajena na vrhu cevi. Tlaka zraka v mehurju in vode v okolici sta izenačena. Zaustavitev pretoka izvedemo s hitrim zapiranjem ventila na dolvodnem robu cevovoda. Spremembo tlaka v zračnem mehurju povzroči tlačni val, ki je vzbujen z zaprtjem dolvodnega ventila. Rezultat interakcije nizkofrekvenčnega vala z mehurjem je visokofrekvenčni tlačni pulz.

Za obravnavana primera (zagon, zaustavitev) se rezultati izračuna in meritev močno razlikujejo, ko v teoretičnem modelu uporabimo ustaljeni model stenskega trenja. Izkaže se, da ta model nezadostno duši tako nizkofrekvenčne kot visokofrekvenčne tlačne spremembe (pulze). To pomanjklivost smo odpravili z vpeljavo konvolucijskega modela neustaljenega stenskega trenja. Ta model zadostno duši tako nizko kot visokofrekvenčne tlake. Za izračun posebej hitrih prehodov priporočamo uporabo konvolucijskega modela. Naj omenimo, da smo v prispevku kot prvi obravnavali interakcije med nizko in visokofrekvenčnimi tlačnimi valovi v cevovodih z v vodi ujetimi zračnimi mehurji.
Ključne besede: prehodni pojav, vodni udar, ujet zračni mehur, diskretni plinski kavitacijski model, neustaljeno stensko trenje, preizkusna postaja

*Naslov avtorja za dopisovanje: Litostroj Power d.o.o., Litostrojska 50, 1000 Ljubljana, Slovenija, anton.bergant@litostrojpower.eu

Strojniški vestnik - Journal of Mechanical Engineering 64(2018)9, SI 74

Prejeto v recenzijo: 2017-12-13
Prejeto popravljeno: 2018-03-14
Odobreno za objavo: 2018-04-11

Diskasto mešalo z asimetrično zapognjenimi lopaticami za visoko stopnjo zračenja

Andrej Bombač
Univerza v Ljubljani, Fakulteta za strojništvo, Slovenija

Namen članka je predstaviti učinkovitost novo razvitega in patentiranega diskastega ABT mešala z asimetrično zapognjenimi lopaticami (ang. Asymmetrically folded Blade Turbine, ABT) pri mešanju in dispergiranju plina v kapljevino v posodi z mešalom. Pri nekaterih fermentacijskih procesih v fermentorjih z mešali je potrebno zagotoviti zelo visoko stopnjo zračenja, pri tem se za dispergiranje zraka v kapljevino uporablja večstopenjsko mešalo. Le to je lahko sestavljeno iz enakih mešal, kot npr. večstopenjsko Rushtonovo mešalo, lahko je kombinirano iz npr. aksialnih in radialnih mešal, kar je vse pogostejša izvedba v zadnjem času. Izbira mešala je ključnega pomena za optimalno izvedbo tehnološkega procesa fermentacije saj mora biti zagotovljeno takšno tokovno polje, da preskrbi mikroorganizme z zrakom po celotnem volumnu kapljevine. Večstopenjsko mešalo ustrezne konfiguracije tako zagotavlja ustrezno cirkulacijo snovi v fermentorju, kar z vidika karakteristik mešanja predstavlja ustrezen hidrodinamski režim. Za popis takšnih razmer pa moramo poznati osnovne karakteristike kot so npr. moč mešanja, prirastek plinaste faze, delež plinaste faze, čas pomešanja, stična površina itn.

V fermentorjih je vnos zraka običajno izveden z razpršilnim obročem na dnu fermentorja, tako je spodnje mešalo zaradi velike količine vnesenega zraka lahko preobremenjeno – poplavljeno. Pri tem postane porazdelitev plinaste faze izrazito nehomogena, spremenijo se tudi ostale osnovne karakteristike. Spodnje mešalo je ključnega pomena za učinkovito dispergiranje in v te namene je bilo razvito mešalo z asimetrično zapognjenimi lopaticami diskastega mešala. Poleg tega mešala je bilo predhodno razvito tudi mešalo z zavitimi lopaticami (ang. Twisted Blade Turbine, TBT).

V prispevku so z vidika dinamike tekočin predstavljene nekatere značilne karakteristike modificiranih diskastih mešal za dispergiranje zraka v posodah z mešali. Analiza modificiranih mešal na modelni mešalni napravi obsega meritve: (a) moči mešanja kapljevine in moči mešanja pri dispergiranju zraka v kapljevino, (b) globalnega prirastka plinaste faze, (c) nastanka poplavnega stanja mešala in (d) časa pomešanja pri mešanju kapljevine. Iz meritev izhaja, da je v območju industrijskega delovanja moč ABT mešala pri mešanju v vodi zelo majhna, izražena s številom moči znaša $Po_{\mathrm{ABT}} \sim 1,75$. Pri dispergiranju zraka v vodo je zmanjšanje moči mešala zelo majhno (manj kot 16%) in se ohranja vse do nastanka poplavnega stanja (primerjalno pri $Fr = 0.3$), pri tem pa dispergira znatno večje količine zraka (do 53 %) kot Rushtonovo mešalo. Pri mešanju kapljevine so bili doseženi najkrajši časi pomešanja z ABT mešalom.

Merjeni časi pomešanja izražajo zgolj časovno spremembo merjene veličine na izbranih lokacijah. Za boljši vpogled v tokovno polje kapljevine v posodi z mešalom in v časovni razvoj nehomogenosti, kot izključno tranzientni pojav, je bil izdelan tudi računalniški izračun dinamike tekočin (ang. Computational Fluid Dynamics, CFD). Za primerjavo učinkovitosti ABT mešala z drugimi mešali so povzeta tudi nekatera izhodišče in rezultati prejšnjih raziskav.

Ključne besede: mešanje kapljevine, dispergiranje zraka, prirastek plina, ABT mešalo, poplavno stanje, čas pomešanja

*Naslov avtorja za dopisovanje: Univerza v Ljubljani, Fakulteta za strojništvo, Aškerčeva 6, 1000 Ljubljana, Slovenija, andrej.bombac@fs.uni-lj.si

Strojniški vestnik - Journal of Mechanical Engineering 64(2018)9, SI 75

Prejeto v recenzijo: 2017-10-16
Prejeto popravljeno: 2018-01-05
Odobreno za objavo: 2018-01-17

Vodni udar in pretrganje kapljevinskega stebra povzročena s hkratnim in zakasnelim zapriranjem dveh ventilov

Uroš Karadžić[1,*] – Marko Janković[2] – Filip Strunjaš[3] – Anton Bergant[4]
[1] Univerza Črne gore, Fakulteta za strojništvo, Črna gora
[2] Elektro podjetje Črne gore, Črna gora
3 Kone, Črna gora
[4] Litostroj Power d.o.o., Slovenija

Prispevek obravnava vodni udar in pretrganje kapljevinskega stebra povzročena s hkratnim in zakasnelim zapiranjem dveh ventilov (eden od ventilov zapira z zakasnitvijo glede na zapiranje drugega) izvedenih v laboratorijski preizkusni postaji Univerze v Črni gori. Raziskave zapiranja dveh ventilov so doprinos avtorjev raziskavam zapiranja z enim ventilom, ki so jih objavili v tej reviji leta 2014. Glavni cilj teoretičnih in eksperimentalnih raziskav je bilo ugotoviti, kako sočasno in časovno zakasnelo zapiranje ventilov vpliva na fiziko tlačnega valovanja v sistemu.

Teoretični model bazira na enčbah neustaljenega kapljevinskega toka v ceveh. Transformacija postavljenih parcialnih diferencialnih enačb hiperboličnega tipa z uporabo metode karakteristik da navadne diferencijalne enačbe, ki jih rešujemo s pomočjo numeričnih metod. V deltoidno mrežo metode karakteristik je vgrajen Zielkejev kovolucijski model neustaljenega stenskega trenja z uporabo zmogljivih računalniških orodij. Vgradnja plinskih kavitacij v numerična vozlišča da diskretni plinski kavitacijski model. Eksperimentalna postaja je sestavljena iz horizontalnega jeklenega cevovoda, ki je vgrajen med gorvodni tlačni kotel in dolvodni ventil z iztokom v atmosfero. Dolžina jeklenega cevovoda je 55,37 m, notranji premer je 18 mm, debelina stene cevi je 2 mm. Prehodni pojav je povzročen s hkratnim in zakasnelim zapiranjem dveh kroglastih zasunov, ki sta vgrajena pri gorvodnem rezervoarju in dolvodno pri iztoku v atmosfero. Tlačne spremembe med prehodi zasledujemo s pomočjo štirih hitro odzivnih zaznaval, ki so vgrajeni vzdolž cevovoda. Na osnovi velikosti Ghidauijevega števila in Duanevoga parametra z upoštevanjem značilk pri različnih pretočnih pogojioh ugotovimo, da se eksperimentalna postaja nahaja v področju, kjer neustaljeno trenje prevladuje.

V laboratorijskem cevnem sistemu smo izvedli številne preizkuse za bolj poglobljeno razumevanje fizike neustaljenega kapljevinskega toka, ki ga povzroči zaprtje dveh ventilov. Frekvenca zajemanja podatkov za vsako kontinuirano izmerjeno veličino je bila f_s = 3,000 Hz. Rezultati izračuna so primerjani z rezultati meritev za dva fizikalno različna tlačna odziva: (1) vodni udar, kjer je tlak med prehodom večji od parnega tlaka kapljevine (voda) in (2) pretrganje kapljevinskega (vodnega) stebra med prehodom, ko tlak pade na parni tlak kapljevine. Pretrganje stebra je v osnovi prehodni kavitacijski tok, ki zajema popolno pretrganje kapljevinskega stebra z veliko kavitacijsko praznino (mehurjem) in kontinuiran kavitacijski tok pri parnem tlaku kapljevine (kapljevina z parnimi mehurčki (fluid)). Izkaže se, da zakasnelo zaprtje drugega ventila lahko vodi do dolgotrajne vzpostavitve parnega tlaka fluida v cevovodu. Rezultati izračuna dobljeni z razvitim plinskim diskretnim kavitacijskim modelom in rezultati meritev se dobro ujemajo za obravnavana primera. Temu sledi originalna parametrična teoretična analiza tlačnih valov povzročenih z zapiranjem dveh ventilov brez in z upoštevanjem kapljevinskega trenja ter prehodne kavitacije. Pokazalo se je, da neustaljeno stensko trenje vpliva na obliko in dušenje tlačnih valov, nima pa večjega vpliva na njihov časovni potek. Vpliv prehodne kavitacije na potek tlaka (oblika, dušenje, časovni potek) je veliko večji, ker so v pojavu zajeti pretrganje stebra, kontinuran kavitacijski tok, udarni valovi in šoki (kondenzacija pare).

V bližnji prihodnosti avtorji načrtujejo vgradnjo računalniško krmiljenih ventilov. Na ta način bo omogočeno nadzorovano hkratno in sekvenčno zapiranje dveh ventilov, ki bo temelj nadaljnjim raziskavam na področju računalniškega krmiljenja dveh in več ventilov v cevnih sistemih.

Ključne besede: cevni sistemi, dva ventila, hkratno in zapoznelo zaprtje dveh ventilov, vodni udar, prekinitev kapljevinskega stebra, preizkusna postaja, neustaljeno stensko trenje

*Naslov avtorja za dopisovanje: Univerza Črne gore, Fakulteta za strojništvo, Dzordza Vasingtona nn, 81000 Podgorica, Črna gora, uros.karadzic@ac.me

Strojniški vestnik - Journal of Mechanical Engineering 64(2018)9, SI 76

Prejeto v recenzijo: 2017-12-28
Prejeto popravljeno: 2018-05-16
Odobreno za objavo: 2018-06-06

Analiza toka v ukrivljenem kanalu z uporabo pravokotne krivočrtne numerične mreže

Mario Krzyk* – Matjaž Četina
Univerza v Ljubljani, Fakulteta za gradbeništvo in geodezijo, Slovenija

Tokovi v naravnih strmih strugah so običajno zelo razgibani, z izrazito nepravilno in spremenljivo obliko struge s številnimi ovinki. Zato je uporaba računske mreže, ki temelji na Kartezijevem koordinatnem sistemu, dokaj neracionalna in lahko povzroči netočnost rezultatov ter nestabilnost računskega postopka. Boljše možnosti prilagajanja obliki struge in njenemu poteku omogoča uporaba krivočrtnih koordinat. Da bi se uporabnost matematičnega modela razširila tudi na reševanje praktičnih problemov, ki zaradi morfologije dna in brežin struge zahtevajo zelo drobno diskretizacijo, smo obstoječi dvodimenzijski globinsko povprečeni matematični model PCFLOW2D, ki je zasnovan na Kartezijevi numerični mreži, dopolnili tako, da upoštevamo značilnosti krivočrtnega koordinatnega sistema. Takšen pristop ima še dve pomembni prednosti, in sicer omogoča upoštevanje centrifugalnih vplivov v ovinkih toka, zaradi boljše usmerjenosti numerične mreže v smeri toka pa se izognemo računskim napakam, ki so posledica prevelike numerične difuzije. Krivočrtni koordinatni sistem je lahko zasnovan v obliki pravokotne ali nepravokotne numerične mreže, in kot osnovo novega matematičnega modela smo izbrali pravokotni krivočrtni koordinatni sistem. Za reševanje sistema parcialnih diferencialnih enačb matematični model uporablja metodo končnih volumnov, ki jo je predlagal Patankar. Osnovne značilnosti metode so premaknjena numerična mreža, hibridna shema, ki predstavlja kombinacijo »upwind« in centralno diferenčne sheme ter iterativni postopek popravkov globin.

Pred uporabo modela na primerih naravne kompleksne geometrije toka smo preverili njegovo natančnost na primeru toka v polkrožnem ovinku. Za ta primer obstaja analitično izpeljana enačba, s pomočjo katere lahko izračunamo razliko med gladinama na zunanjem in notranjem robu kanala v ovinku. Predvideli smo kanal širine 20 m, z radijem ukrivljenosti 30 m in horizontalnim dnom. Da bi izničili morebitne vplive robnih pogojev na gorvodnem in dolvodnem robu kanala, je bil pred in za ovinkom predviden odsek ravnega kanala dolžine 100 m. Obravnavano področje matematičnega modela smo pokrili s 296 računskimi točkami v smeri toka in 24 točkami prečno na smer toka. V matematičnem modelu smo upoštevali zelo majhne vrednosti koeficienta hrapavosti brežin. S tem smo izničili vpliv ostenja na tok in višino hidravličnih izgub. Analizo hidravličnih razmer v ovinku kanala smo opravili pri pretokih od 100 m^3/s do 900 m^3/s s korakom 100 m^3/s, kar ustreza povprečnim hitrostim toka v ovinku od ca. 1 m/s do približno 9 m/s. Izračunali smo razpored globine toka v vseh računskih točkah matematičnega modela in tako dobili potek proste gladine vode v kanalu. Za vsak primer pretoka, oziroma hitrosti toka v kanalu smo določili kritično globino, globino vode na gorvodnem in dolvodnem robu ravnega kanala ter srednjo hitrost toka v ovinku, s pomočjo katere smo z uporabo analitične formule za izračun razlike med globinama brežin kanala v ovinku izračunali vrednost prečnega naklona gladine. Rezultate numeričnih in teoretičnih izračunov smo med seboj primerjali.

Ob zaključku opravljene analize toka v polkrožnem ovinku z zanemarljivim vplivom trenja ob ostenje lahko ugotovimo, da je potek proste gladine toka v ovinku odvisen od režima toka (mirni, prehodni ali deroči). Z uporabo srednje hitrosti toka v ovinku za izračun teoretične vrednosti naklona gladine smo dosegli zelo dobro ujemanje med teoretično izračunanim prečnim naklonom proste gladine v ovinku in rezultati matematičnega modela. Razlika med analitično rešitvijo in rezultati matematičnega modela v obravnavanih hidravličnih okoliščinah znaša do 4 %, upoštevajoč srednjo globino toka v kanalu za posamezni primer. S tem je bilo potrjeno, da je matematični model pripravljen za nadaljnje dopolnitve za analize toka v kompleksnih strmih hudourniških strugah.

Ključne besede: tok v ukrivljenem kanalu, dvodimenzijski matematični model, pravokotne krivočrtne koordinate, globinsko povprečeni tok, PCFLOW2D-ORTHOCURVE

*Naslov avtorja za dopisovanje: Univerza v Ljubljani, Fakulteta za gradbeništvo in geodezijo, Jamova cesta 2, 1000, Ljubljana, Slovenija, mkrzyk@fgg.uni-lj.si

Strojniški vestnik - Journal of Mechanical Engineering 64(2018)9, SI 77

Prejeto v recenzijo: 2017-06-02
Prejeto popravljeno: 2017-09-21
Odobreno za objavo: 2017-10-13

Numerična napoved kavitirajočega toka okoli ladijskega vijaka in okoli gonilnika Kaplanove turbine s kalibriranimi kavitacijskimi modeli

Mitja Morgut[1,*] – Dragica Jošt[2] – Aljaž Škerlavaj[2] – Enrico Nobile[1] – Giorgio Contento[1]
[1] Univerza v Trstu, Oddelek za inženirstvo in arhitekturo, Trst, Italija
[2] Kolektor Turboinštitut, Slovenia

Za konkurenčen nastop na trgu je poleg kakovosti produkta pomemben tudi čas od začetka razvoja do prodaje. Ta čas lahko bistveno skrajšamo z uporabo računalniške dinamike tekočin (CFD - computational fluid dynamics), ki omogoča, da dražje in časovno zamudne eksperimentalne analize izvajamo le v končni fazi projekta.

V primeru ladijskih vijakov in vodnih turbin numerično analizo toka uporabljamo za napoved učinkovitosti sistema in preučevanje specifičnih lokalnih pojavov v toku, kot je npr. kavitacija. Ta vpliva v večini primerov na delovanje ladijskih vijakov in vodnih turbin negativno, ker povzroča večje izgube, padec izkoristka, erozijo materiala ter ojačenje hrupa in vibracij.

V zadnjih desetletjih so bili razviti različni modeli za numerično preučevanje in analizo kavitacijskih pojavov. V tem prispevku smo uporabili homogeni model, ki obravnava dvofazni tok kot homogeno zmes vode in vodne pare, v kateri ni zdrsa med kapljevito in plinasto fazo. Gostota zmesi je določena na podlagi prenosne enačbe za prostorninski delež kapljevite faze, v kateri izvorni členi regulirajo stopnjo uparjanja in kondenzacije. Omenjene izvorne člene je mogoče modelirati z različnimi kavitacijskimi modeli. V predhodni raziskavi so bile na podlagi analize kavitirajočega toka okoli osamljenega profila NACA66MOD kalibrirane empirične konstante treh različnih kavitacijskih modelov. V tem prispevku smo želeli preveriti veljavnost teh kalibriranih modelov za napoved kavitacije na ladijskem vijaku in na gonilniku Kaplanove turbine. S tem namenom smo simulirali delovanje propelerja PPTC v homogenem toku in Kaplanove turbine, za katero je bila eksperimentalna raziskava izvedena v Kolektor Turboinštitutu v Ljubljani.

Čeprav je bil namen raziskave predvsem preveriti kalibrirane kavitacijske modele, smo delno preverili tudi vpliv turbulentnega modela. Zato smo poleg standardnega RANS (Reynolds Averaged Navier Stokes) pristopa računali tudi z dolgotrajnejšimi, a tudi bolj natančnimi SAS (Scale Adaptive Simulation) simulacijami. Vse numerične analize smo izvedli s komercialnim CFD programom ANSYS-CFX, ki sloni na metodi končnih prostornin, natančneje na metodi CV-FEM (control volume – finite element method).

Numerične rezultate smo primerjali z dosegljivimi eksperimentalnimi podatki. Za kakovostno primerjavo smo primerjali izračunane in eksperimentalne slike kavitacijskih oblakov okoli lopatic ladijskega vijaka in turbine. Za kakovostno primerjavo smo pri ladijskem vijaku primerjali pogon, pri turbini pa izgube v sesalni cevi in izkoristek turbine.

Iz prikazane raziskave izhaja, da so vsi trije kalibrirani kavitacijski modeli primerni za napoved kavitacije na ladijskem vijaku in na gonilniku Kaplanove turbine. Učinkovitost obeh sistemov (pogon ladijskega vijaka in izkoristek turbine) je bila z vsemi tremi modeli napovedana s podobno natančnostjo, čeprav so bile opazne manjše razlike v velikosti kavitacijskih oblakov. Glede turbulentnih modelov se je za ladijski vijak pokazalo, da z modelom SAS bolj pravilno napovemo vrtinčne strukture v toku in posledično tudi kavitacijo znotraj teh struktur. V primeru Kaplanove turbine, kjer je izkoristek močno odvisen od pravilne napovedi časovno odvisnega toka v sesalni cevi in turbulentnih struktur v njem, model SAS SST predstavlja dober kompromis med standardnimi RANS in računsko zahtevnejšimi LES (Large Eddy Simulation) simulacijami.

Ključne besede: kavitacija, ladijski vijak, Kaplanova turbina, modeli prenosa snovi, RANS, SAS

*Naslov avtorja za dopisovanje: Univerza v Trstu, Oddelek za inženirstvo in arhitekturo, ,via A. Valerio 10, 34127 Trst, Italija, mmorgut@units.it

Strojniški vestnik - Journal of Mechanical Engineering 64(2018)9, SI 78

Prejeto v recenzijo: 2017-05-27
Prejeto popravljeno: 2017-09-22
Odobreno za objavo: 2017-10-12

Izdelava topografije vodne gladine z uporabo LIDAR podatkov

Gašper Rak[1,*] – Marko Hočevar[2] – Franci Steinman[1]
[1] Univerza v Ljubljani, Fakulteta za gradbeništvo in geodezijo, Slovenija
[2] Univerza v Ljubljani, Fakulteta za strojništvo, Slovenija

Izmera topografije vodne gladine je pomembna tako pri vodnih zgradbah, pri obratovanju hidroelektrarn in tudi pri določanju poteka gladin v vodotokih, še posebej pri pojavu visokih voda. Zato smo raziskali razmere na sotočju dveh deročih tokov, kjer se pojavljajo izrazito tridimenzionalne tokovne razmere valovanja, pri čemer se oblikuje časovno spremenljiva struktura vodnega toka v prečni in vzdolžni smeri.

Zaradi hitre spremenljivosti vodne gladine in pojava razpenjenega oz. dvofaznega toka merilne metode, ki se običajno uporabljajo v hidrotehniki, niso več primerne za zajem topografije vodne gladine z veliko prostorsko in časovno ločljivostjo. Zato smo preverili uporabnost zajema topografije kompleksne vodne gladine z laserskim skeniranjem. Nesporno široka uporabnost laserskega skeniranja se kaže predvsem pri meritvah trdnih teles, če le glede na zahtevnost morfologije površine izberemo zadostno število opazovalnih izhodišč. Čeprav v splošnem merilna metoda velja za manj primerno ali celo neuporabno za meritve površine vodnih teles, so nekateri avtorji s svojimi poskusi, a z dodajanjem delcev v vodo za izboljšanje odbojnosti, že potrdili uporabnost laserske metode tudi pri meritvah potovanja in preoblikovanja valov, kjer pa gre večinoma za počasnejšo dinamiko pojava kot v našem primeru.

Dodatno vrednost tej merilni metodi zato dajejo tudi rezultati naše raziskave. Lasersko skeniranje je bilo z inovativnim pristopom uporabljeno za meritve vodne gladine dinamičnega, razburkanega dvofaznega vodnega toka. Rezultati kažejo, da je merilna metoda učinkovita tudi pri modelnih raziskavah v primeru uporabe čiste vode, tako za meritve gladine stoječe vode kakor tudi za zajem poteka vodne gladine z veliko časovno spremenljivostjo, katere dinamike sicer s klasičnimi meritvami ni mogoče zadovoljivo zajeti. Pri tem je treba poudariti, da metoda preizkušeno daje zelo dobre rezultate v primerih izrazitih dvofaznih tokov. V primerih vodnega telesa z razmeroma majhno vsebnostjo zračnih mehurčkov oz. majhno gostoto dvofaznega toka v vrhnji plasti je merilna metoda lahko manj primerna, globine vode podcenjene, natančen potek gladine pa težko določljiv.

Pri hidravličnih pojavih z močno ozračenimi zgornjimi sloji vodnih teles z zveznim in homogenim slojem mehurčkov pa je mogoč brezkontakten a zelo natančen zajem prečnega poteka gladine in s tem topografije vodne gladine kompleksnih primerov z ozračenim tokom in močno vertikalno ter horizontalno dinamiko. Zajem podatkov z veliko časovno in krajevno ločljivostjo je, predvsem v primerih z močno razgibano gladino v prečni smeri, pomemben podatek tudi za umerjanje in verifikacijo numeričnih modelov, saj danes tudi s polnimi 3D numeričnimi modeli še ni mogoče dovolj natančno simulirati tokovnih razmer na T-sotočju, tj. na območju z dovolj enostavno geometrijo kanalov.

Članek prikazuje tudi obdelavo surovega oblaka točk odbojev, kar omogoča analiziranje in ovrednotenje tudi praktično sočasne fluktuacije vodne gladine preko celotnih merjenih prerezov, saj je dinamika pomika laserskega žarka bistveno večja od dinamike spreminjanja gladine. Konstruiranje topografije vodne gladine intenzivnega valovanja iz surovega oblaka točk meritev z laserskim skeniranjem omogoča določanje značilnosti valovanja, nadaljnje analize tokovnih razmer in določitev glavnih struktur vodnega toka na sotočju in njihovih lastnosti v odvisnosti od integralnih parametrov v obeh dotokih, zato predstavljajo izhodišče za določanje topologije T-sotočja.

Ključne besede: laserski skener, vodna površina, topografija, dvofazni tok, sotočje

*Naslov avtorja za dopisovanje: Univerza v Ljubljani, Fakulteta za gradbeništvo in geodezijo, Slovenija, gasper.rak@fgg.uni-lj.si

Strojniški vestnik - Journal of Mechanical Engineering 64(2018)9, SI 79

Prejeto v recenzijo: 2018-02-05
Prejeto popravljeno: 2018-06-06
Odobreno za objavo: 2018-07-03

Eksperimentalna hidravlična analiza vtočnih razmer črpalk za hladilne stolpe

Gregor Žvab[1,*] – Gregor Lapuh[2]
[1] Kolektor-Turboinštitut d.o.o., Slovenija
[2] Nuklearna elektrarna Krško, Slovenija

Hlajenje kondenzatorja v elektrarnah s pretočno vodo velja za najgospodarnejšo in najboljšo termodinamično rešitev. Za visoko razpoložljivost, visok izkoristek in varnost postrojenja morajo črpališča v hladilnem sistemu delovati brezhibno. Pojav intenzivnih vrtincev na vstopu v sesalno ustje črpalke lahko dolgoročno poškoduje vitalne dele črpalke in celo privede do odpovedi. V konkretnem primeru v elektrarni so bili na hladilnem sistemu na črpališču za hladilne stolpe že dlje časa opaženi nedovoljeni površinski vrtinci na vtokih črpalk. Intenziteta vrtincev v skladu s standardom ANSI/HI ni bila sprejemljiva za varno obratovanje črpališča, hkrati pa so bile izmerjene tudi povišane vibracije na črpalkah, ki bi lahko bile posledica omenjenih razmer na vtokih črpalk. Za zanesljivost obratovanja je bilo treba za ustrezno sanacijo podrobno poznavanje hidravličnih razmer na črpališču.

V članku je predstavljena eksperimentalna hidravlična analiza, na podlagi katere smo modelirali razmere v naravi (na črpališču) v pomanjšanem merilu 1 : 16 v laboratoriju. Laboratorijske meritve na fizičnem modelu predstavljajo glavni del raziskave, ki so omogočile enostavnejše in cenejše opazovanje ter posledično lažjo izbiro ukrepov za izboljšanje hidravličnih razmer v toku. Začetki raziskav vtočnih razmer črpalk pri toku s prosto gladino segajo že v obdobje začetka druge polovice 20. stoletja. Pridobljena teoretična in eksperimentalna znanja so privedla v postopno oblikovanje splošnih navodil, ne nazadnje v izdelavo smernic standarda ANSI/HI, ki jim je sledila tudi naša raziskava.

V eksperimentalnem delu sledi analiza črpališča za hladilne stolpe. Ugotovljene so bile glavne nepravilnosti pri načrtovanju vtočne zgradbe v primerjavi s pozneje izdanimi smernicami ANSI/HI. Uporabili smo brezdimenzijsko analizo. V okviru dovoljenih predpostavk smo zadostili geometrijski, kinematični in dinamični podobnosti. Izvedba modelnega preizkusa je zajemala izdelavo modela in merilne proge, umerjanje modela, izračun merilne negotovosti ter meritve. Glede na obseg modela, smo se omejili le na območje vtočne zgradbe, ki ima prevladujoč hidravlični vpliv na razmere v okolici črpalk. V rezultatih smo predstavili opazovane intenzitete vrtincev, globine potopitve črpalk ter stopnjo vrtinčenja v sesalni cevi črpalk za vse obratovalne režime. Za obstoječe stanje smo pridobili identične tokovne razmere na vtokih črpalk z nastajanjem površinskega vrtinca tipa 6 na enakem območju s podobno intenziteto in frekvenco nastajanja. Razmere smo opazovali in merili tudi za predvideno stanje z vgrajeno zapornico na preliv vtočnega bazena. Nivoji gladin bodo višji, vendar je bilo kljub temu treba poznati razmere za obe stanji. Na podlagi opazovanj in meritev smo uspeli utemeljiti vzrok za nastanek nedovoljenega površinskega vrtinca. S spremembo zasnove geometrije vtočnega bazena je bilo treba nadalje izboljšati tokovne razmere v njem. Omejili smo se na tri ukrepe, ki so bili izbrani na podlagi izkušenj inštituta in priporočil standarda ANSI/HI. Ukrep z vgrajeno podaljšano vmesno steno med črpalki je zagotovil ustrezne tokovne razmere v vtočnem bazenu pri povečanem pretoku skozi črpalki za faktor 1,5 v skladu s smernicami.

V diskusiji smo primerjali vzroke za nastanek površinskega vrtinca na gladini z že izvedenimi raziskavami pri podobnih robnih pogojih na črpališčih. Močan vpliv za nastanek površinskih vrtincev pri zadostni potopitvi črpalk je imel močan bližnji prečni tok glede na os črpalke. Tok kapljevine mora pritekati čim bolj enakomerno in sovpadati z osjo črpalke. V znanstvenem pomenu raziskava potrjuje dobro napoved tokovnih razmer na prototipu na podlagi fizičnega modelnega testa, izvedenega v skladu s smernicami ANSI/HI. Fizični model lahko nadalje uporabimo za različne empirično pridobljene zveze med hidravličnimi in geometrijskimi parametri ter ne nazadnje za validacijo numeričnega modela. V praktičnem pomenu pa smo z raziskavo določili optimalen ukrep za sanacijo črpališča. Pridobljene izkušnje v raziskavi so hkrati prenosljive na črpališča, ki bodo načrtovana s podobno zasnovo geometrije.

Ključne besede: vtočne strukture, fizični hidravlični model, tok s prosto gladino, površinski vrtinci, vertikalne črpalke

*Naslov avtorja za dopisovanje: Kolektor- Turboinštitut d.o.o., Slovenija, gregor.zvab@litostrojpower.eu

Information for Authors

All manuscripts must be in English. Pages should be numbered sequentially. The manuscript should be composed in accordance with the Article Template given above. The maximum length of contributions is 10 pages. Longer contributions will only be accepted if authors provide juastification in a cover letter. For full instructions see the Information for Authors section on the journal's website: http://en.sv-jme.eu .

SUBMISSION:

Submission to SV-JME is made with the implicit understanding that neither the manuscript nor the essence of its content has been published previously either in whole or in part and that it is not being considered for publication elsewhere. All the listed authors should have agreed on the content and the corresponding (submitting) author is responsible for having ensured that this agreement has been reached. The acceptance of an article is based entirely on its scientific merit, as judged by peer review. Scientific articles comprising simulations only will not be accepted for publication; simulations must be accompanied by experimental results carried out to confirm or deny the accuracy of the simulation. Every manuscript submitted to the SV-JME undergoes a peer-review process.

The authors are kindly invited to submit the paper through our web site: http://ojs.sv-jme.eu. The Author is able to track the submission through the editorial process - as well as participate in the copyediting and proofreading of submissions accepted for publication - by logging in, and using the username and password provided.

SUBMISSION CONTENT:

The typical submission material consists of:

- A **manuscript** (A PDF file, with title, all authors with affiliations, abstract, keywords, highlights, inserted figures and tables and references),
- Supplementary files:
  - a **manuscript** in a WORD file format
  - a **cover letter** (please see instructions for composing the cover letter)
  - a ZIP file containing **figures** in high resolution in one of the graphical formats (please see instructions for preparing the figure files)
  - possible **appendicies** (optional), cover materials, video materials, etc.

Incomplete or improperly prepared submissions will be rejected with explanatory comments provided. In this case we will kindly ask the authors to carefully read the Information for Authors and to resubmit their manuscripts taking into consideration our comments.

COVER LETTER INSTRUCTIONS:

Please add a **cover letter** stating the following information about the submitted paper:

1. Paper **title**, list of **authors** and their **affiliations**.
2. **Type of paper**: original scientific paper (1.01), review scientific paper (1.02) or short scientific paper (1.03).
3. A **declaration** that neither the manuscript nor the essence of its content has been published in whole or in part previously and that it is not being considered for publication elsewhere.
4. State the **value of the paper** or its practical, theoretical and scientific implications. What is new in the paper with respect to the state-of-the-art in the published papers? Do not repeat the content of your abstract for this purpose.
5. We kindly ask you to suggest at least two **reviewers** for your paper and give us their names, their full affiliation and contact information, and their scientific research interest. The suggested reviewers should have at least two relevant references (with an impact factor) to the scientific field concerned; they should not be from the same country as the authors and should have no close connection with the authors.

FORMAT OF THE MANUSCRIPT:

The manuscript should be composed in accordance with the Article Template. The manuscript should be written in the following format:

- A **Title** that adequately describes the content of the manuscript.
- A list of **Authors** and their **affiliations**.
- An **Abstract** that should not exceed 250 words. The Abstract should state the principal objectives and the scope of the investigation, as well as the methodology employed. It should summarize the results and state the principal conclusions.
- 4 to 6 significant **key words** should follow the abstract to aid indexing.
- 4 to 6 **highlights;** a short collection of bullet points that convey the core findings and provide readers with a quick textual overview of the article. These four to six bullet points should describe the essence of the research (e.g. results or conclusions) and highlight what is distinctive about it.
- An **Introduction** that should provide a review of recent literature and sufficient background information to allow the results of the article to be understood and evaluated.
- A **Methods** section detailing the theoretical or experimental methods used.
- An **Experimental section** that should provide details of the experimental set-up and the methods used to obtain the results.
- A **Results** section that should clearly and concisely present the data, using figures and tables where appropriate.
- A **Discussion** section that should describe the relationships and generalizations shown by the results and discuss the significance of the results, making comparisons with previously published work. (It may be appropriate to combine the Results and Discussion sections into a single section to improve clarity.)
- A **Conclusions** section that should present one or more conclusions drawn from the results and subsequent discussion and should not duplicate the Abstract.
- **Acknowledgement** (optional) of collaboration or preparation assistance may be included. Please note the source of funding for the research.
- **Nomenclature** (optional). Papers with many symbols should have a nomenclature that defines all symbols with units, inserted above the references. If one is used, it must contain all the symbols used in the manuscript and the definitions should not be repeated in the text. In all cases, identify the symbols used if they are not widely recognized in the profession. Define acronyms in the text, not in the nomenclature.
- **References** must be cited consecutively in the text using square brackets [1] and collected together in a reference list at the end of the manuscript.
- **Appendix(-icies)** if any.

SPECIAL NOTES

Units: The SI system of units for nomenclature, symbols and abbreviations should be followed closely. Symbols for physical quantities in the text should be written in italics (e.g. v, T, n, etc.). Symbols for units that consist of letters should be in plain text (e.g. ms^{-1}, K, min, mm, etc.). Please also see: http://physics.nist.gov/cuu/pdf/sp811.pdf .

Abbreviations should be spelt out in full on first appearance followed by the abbreviation in parentheses, e.g. variable time geometry (VTG). The meaning of symbols and units belonging to symbols should be explained in each case or cited in a **nomenclature** section at the end of the manuscript before the References.

Figures (figures, graphs, illustrations digital images, photographs) must be cited in consecutive numerical order in the text and referred to in both the text and the captions as Fig. 1, Fig. 2, etc. Figures should be prepared without borders and on white grounding and should be sent separately in their original formats. If a figure is composed of several parts, please mark each part with a), b), c), etc. and provide an explanation for each part in Figure caption. The caption should be self-explanatory. Letters and numbers should be readable (Arial or Times New Roman, min 6 pt with equal sizes and fonts in all figures). Graphics (submitted as supplementary files) may be exported in resolution good enough for printing (min. 300 dpi) in any common format, e.g. TIFF, BMP or JPG, PDF and should be named Fig1.jpg, Fig2.tif, etc. However, graphs and line drawings should be prepared as vector images, e.g. CDR, AI. Multi-curve graphs should have individual curves marked with a symbol or otherwise provide distinguishing differences using, for example, different thicknesses or dashing.

Tables should carry separate titles and must be numbered in consecutive numerical order in the text and referred to in both the text and the captions as Table 1, Table 2, etc. In addition to the physical quantities, such as t (in italics), the units [s] (normal text) should be added in square brackets. Tables should not duplicate data found elsewhere in the manuscript. Tables should be prepared using a table editor and not inserted as a graphic.

REFERENCES:

A reference list must be included using the following information as a guide. Only cited text references are to be included. Each reference is to be referred to in the text by a number enclosed in a square bracket (i.e. [3] or [2] to [4] for more references; do not combine more than 3 references, explain each). No reference to the author is necessary.

References must be numbered and ordered according to where they are first mentioned in the paper, not alphabetically. All references must be complete and accurate. Please add DOI code when available. Examples follow.

Journal Papers:

Surname 1, Initials, Surname 2, Initials (year). Title. Journal, volume, number, pages, DOI code.

[1] Hackenschmidt, R., Alber-Laukant, B., Rieg, F. (2010). Simulating nonlinear materials under centrifugal forces by using intelligent cross-linked simulations. *Strojniški vestnik - Journal of Mechanical Engineering,* vol. 57, no. 7-8, p. 531-538, DOI:10.5545/sv-jme.2011.013.

Journal titles should not be abbreviated. Note that journal title is set in italics.

Books:

Surname 1, Initials, Surname 2, Initials (year). Title. Publisher, place of publication.

[2] Groover, M.P. (2007). *Fundamentals of Modern Manufacturing*. John Wiley & Sons, Hoboken.

Note that the title of the book is italicized.

Chapters in Books:

Surname 1, Initials, Surname 2, Initials (year). Chapter title. Editor(s) of book, book title. Publisher, place of publication, pages.

[3] Carbone, G., Ceccarelli, M. (2005). Legged robotic systems. Kordić, V., Lazinica, A., Merdan, M. (Eds.), Cutting Edge Robotics. Pro literatur Verlag, Mammendorf, p. 553-576.

Proceedings Papers:

Surname 1, Initials, Surname 2, Initials (year). Paper title. Proceedings title, pages.

[4] Štefanić, N., Martinčević-Mikić, S., Tošanović, N. (2009). Applied lean system in process industry. *MOTSP Conference Proceedings*, p. 422-427.

Standards:

Standard-Code (year). Title. Organisation. Place.

[5] ISO/DIS 16000-6.2:2002. *Indoor Air – Part 6: Determination of Volatile Organic Compounds in Indoor and Chamber Air by Active Sampling on TENAX TA Sorbent, Thermal Desorption and Gas Chromatography using MSD/FID.* International Organization for Standardization. Geneva.

WWW pages:

Surname, Initials or Company name. Title, from http://address, date of access.

[6] Rockwell Automation. Arena, from *http://www.arenasimulation.com,* accessed on 2009-09-07.

EXTENDED ABSTRACT:

When the paper is accepted for publishing, the authors will be requested to send an **extended abstract** (approx. one A4 page or 3500 to 4000 characters). The instruction for composing the extended abstract are published on-line: http://www.sv-jme.eu/information-for-authors/ .

COPYRIGHT:

Authors submitting a manuscript do so on the understanding that the work has not been published before, is not being considered for publication elsewhere and has been read and approved by all authors. The submission of the manuscript by the authors means that the authors automatically agree to transfer copyright to SV-JME when the manuscript is accepted for publication. All accepted manuscripts must be accompanied by a Copyright Transfer Agreement, which should be sent to the editor. The work should be original work by the authors and not be published elsewhere in any language without the written consent of the publisher. The proof will be sent to the author showing the final layout of the article. Proof correction must be minimal and executed quickly. Thus it is essential that manuscripts are accurate when submitted. Authors can track the status of their accepted articles on http://en.sv-jme.eu/.

PUBLICATION FEE:

Authors will be asked to pay a publication fee for each article prior to the article appearing in the journal. However, this fee only needs to be paid after the article has been accepted for publishing. The fee is 320 EUR (for articles with maximum of 6 pages), 400 EUR (for articles with maximum of 10 pages), plus 40 EUR for each additional page. The additional cost for a color page is 90.00 EUR. These fees do not include tax.

Strojniški vestnik -Journal of Mechanical Engineering
Aškerčeva 6, 1000 Ljubljana, Slovenia,
e-mail: info@sv-jme.eu

9 770039 248001
ISSN 0039-2480

http://www.sv-jme.eu

Contents

Papers